# STUDIES ON ABOVEGROUND STORAGE TANKS SUBJECTED TO WIND LOADING: STATIC, DYNAMIC, AND COMPUTATIONAL FLUID DYNAMICS ANALYSES

by

Yen-Chen Chiang

A Thesis

Submitted to the Faculty of Purdue University
In Partial Fulfillment of the Requirements for the degree of

Master of Science in Civil Engineering
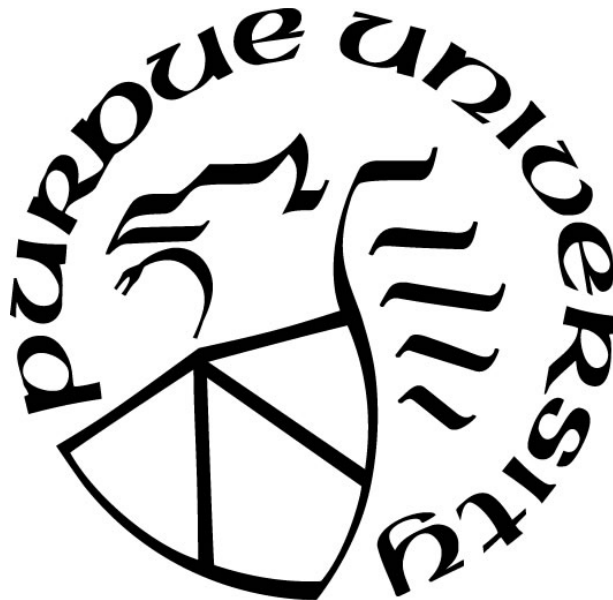
Lyles School of Civil Engineering

West Lafayette, Indiana

May 2019

THE PURDUE UNIVERSITY GRADUATE SCHOOL
STATEMENT OF COMMITTEE APPROVAL

Dr. Sukru Guzey, Chair

     Lyles School of Civil Engineering

Dr. Mark D. Bowman

     Lyles School of Civil Engineering

Dr. Ghadir Haikal

     Lyles School of Civil Engineering

Approved by:

     Dr. Dulcy M. Abraham

       Head of the Graduate Program

Dedicated to my parents.

ACKNOWLEDGMENTS

I would like to thank my advisor, Dr. Sukru Guzey, for his support and all his effort. Dr. Guzey was the one who trusted me in my capability, and provide me guidance throughout my graduate study. I also like to express my gratitude to my committee members, Dr. Mark Bowman and Dr. Ghadir Haikal, for their time reviewing my work and their precious comments on my thesis. Special thanks to Dr. Azzuni, who has always been a good mentor.

I would like to acknowledge my parents, who have been always with me, providing various kind of supports. If my mother did not encourage me to come to the states, none of these would have come true. Dr. Huang and Dr. Liao from National Taiwan University have been providing valuable suggestions on my career plans. Finally, I would like to acknowledge Mr. Rich for rigorously proofreading my works.

TABLE OF CONTENTS

LIST OF TABLES

LIST OF FIGURES

ABSTRACT

Author: Chiang, Yen-Chen. MSCE
Institution: Purdue University
Degree Received: May 2019
Title: Studies on Aboveground Storage Tanks Subjected to Wind loading: Static, Dynamic, and Computational Fluid Dynamics Analyses
Committee Chair: Sukru Guzey

Due to the slender geometries of aboveground storage tanks, maintaining the stability under wind gusts of these tanks has always been a challenge. Therefore, this thesis aims to provide a through insight on the behavior of tanks under wind gusts using finite element analysis and computational fluid dynamic (CFD) analysis. The present thesis is composed of three independent studies, and different types of analysis were conducted. In Chapter 2, the main purpose is to model the wind loading dynamically and to investigate whether a resonance can be triggered. Research on tanks subjected to static wind load have thrived for decades, while only few studies consider the wind loading dynamically. Five tanks with different height (H) to diameter (D) ratios, ranging from 0.2 to 4, were investigated in this chapter. To ensure the quality of the obtained solution, a study on the time step increment of an explicit dynamic analysis, and a on the mesh convergence were conducted before the analyses were performed. The natural vibration frequencies and the effective masses of the selected tanks were first solved. Then, the tanks were loaded with wind gusts with the magnitude of the pressure fluctuating at the frequency associating with the most effective mass and other frequencies. Moreover, tanks with eigen-affine imperfections were also considered. It was concluded that resonance was not observed in any of these analyses. However, since the static buckling capacity and the dynamic buckling capacity has a relatively large difference for tall tanks ($H/D \geq 2.0$), a proper safety factor shall be included during the design if a static analysis is adopted.

Chapter 3 focus on the effect of an internal pressure generated by wind gusts on open-top tanks. Based on boundary layer wind tunnel tests (BLWT), a significant pressure would be generated on the internal side of the tank shell when a gust of wind blow through an open-top tank. This factor so far has not been sufficiently accounted for by either ASCE-7 or API 650, despite the fact that this internal pressure may almost double the design pressure. Therefore, to investigate the effect

of the wind profile along with the internal pressure, multiple wind profiles specified in different design documents were considered. The buckling capacities of six tanks with aspect ratios (H/D) ranging from 0.1 to 4 were analyzed adopting geometrically nonlinear analysis with imperfection using an arc-length algorithm (Riks analysis). Material nonlinearity was also included in some analyses. It was observed that the buckling capacity of a tank obtained using ASCE-7/API 650 wind profile is higher than buckling capacities obtained through any other profiles. It was then concluded that the wind profile dictated by the current North American design documents may not be conservative enough and may need a revision.

Chapter 4 investigates how CFD can be applied to obtain the wind pressure distribution on tanks. Though CFD has been widely employed in different research areas, to the author's best knowledge, only one research has been dedicated to investigate the interaction between wind gusts and tanks using CFD. Thus, a literature review on the guideline of selecting input parameter for CFD and a parametric study as how to choose proper input parameters was presented in Chapter 4. A tank with an aspect ratio of 0.5 and a flat roof was employed for the parametric study. To ensure the validity of the input parameters, the obtained results were compared with published BLWT results. After confirming that the selected input parameters produces acceptable results, tanks with aspect ratio ranging from 0.4 to 2 were adopted and wind pressure distribution on such tanks were reported. It was concluded that the established criteria for deciding the input parameters were able to guarantee converged results, and the obtained pressure coefficients agree well with the BLWT results available in the literature.

1. INTRODUCTION

1.1 Thesis Background

Aboveground storage tanks are widely adopted in many industries to store water, petroleum products, etc. To make the tanks cost efficient, circular cylindrical shells with relatively thin thickness are vastly chosen. However, because of the slender geometries, the tanks are prone to buckle induced by various events such as ground motions, internal vacuums and wind gusts. The present thesis focused on the interaction between empty aboveground storage tanks and wind gusts.

To prevent open-top tanks from buckling due to wind gusts, wind girders are widely employed as a solution to provide stability to the tanks, and the formula for sizing the wind girder was first presented by an American Water Work Association (AWWA) document [1]. It was derived assuming the static wind pressure is uniformly acting on the projected surface normal to the wind direction [2]. The design pressure was identical for either an open-top or a close-top tank, assuming the internal pressure to be 14% of the external pressure. Current design documents, including API 650 [3] and ASCE-7 [4], adopt similar design philosophy. However, based on results of wind tunnel experiments [5, 6], a substantial internal inward pressure was observed for open-top tanks subject to wind loading. The magnitude of the internal pressure can be as large as 90% of the magnitude of the external pressure at the windward stagnation point. Considering this factor, the difference of wind design pressure between a close-top and an open-top tank shall be significant. Although design documents including AS/NZS 1170.2:2011 [7], and EN1993-4-1 [8] have explicitly addressed this factor, most of the North American design documents [3, 4] have not yet reflected this significant difference between the design pressure of an open- and a close-top tank.

Besides, most of the researchers chose to adopt static analysis to analyze the buckling behavior of tanks subject to wind loading. Several studies [9-11] have been dedicated to investigate the dynamic buckling behavior of tanks, and concluded that resonance was not observed when subjected to wind loading. However, only a small spectrum of tanks has been analyzed, and limited information is available. Chapter 2 is devoted to investigate the natural vibration frequency of and the dynamic effect on buckling capacity of empty open-top tanks with a wide range of aspect ratio

(height to diameter ratio). The results of this study was submitted to Engineering Structures Journal on July 2, 2018, and is currently under review.

Chapter 3 aims to compare the buckling behavior of tanks when the wind loading follows wind distribution profiles specified in various design documents. The stability of tanks design in accordance with current design code (API 650 [3]) is employed and the adequacy of the design documents is examined. The results of this study have been published at ASME Journal of Pressure Vessel Technology [12] (doi: 10.1115/1.4042992).

Chapter 4 utilizes computational fluid dynamics (CFD) analysis as a main tool to investigate the wind pressure distribution on close-top tanks. As there is barely any study been conducted to explore the interaction between wind gusts and tank using CFD, this study reviewed available guidelines, and did a through parametric study on the input parameters. After the criteria of deciding the input parameters were obtained, CFD analyses were conducted adopting tanks with various geometries.

1.2 Objective and Scope

The objective of this study is to provide practical guideline and insight for engineers to design tanks under wind loading properly. Dynamic effect and rather large internal pressure are accounted for in the analyses. The adequacy of current design documents is then discussed.

The scope of the study includes: (1) dynamic analysis of aboveground open-top steel tanks subjected to wind loading, (2) influence of internal inward pressure on stability of open-top aboveground steel tanks subjected to wind loading, and (3) application of computational fluid dynamics on close-top tanks under wind loading.

1.3 Organization

This thesis is composed on five chapters and are present as follows:

Chapter 1: introduction of the thesis, and background of the study.

Chapter 2: dynamic analysis of aboveground open-top steel tanks subjected to wind loading.

Chapter 3: influence of internal inward pressure on stability of open-top aboveground steel tanks subjected to wind loading.

Chapter 4: application of computational fluid dynamics on close-top tanks under wind loading.

Chapter 5: closing remarks.

1.4 References

[1]   AWWA, *Standard Specifications for Elevated Steel Water Tanks, Standpipes and Reservoirs*. Denver, CO: American Water Work Association, 1935, pp. 1606-1625.

[2]   R. V. McGrath, "Stability of API standard 650 tank shells," in *28th Midyear meeting of the American Petroleum Institute's division of refining*, Brooklyn, N.Y., 1963: American Petroleum Institute.

[3]   API, *Welded Tanks for Oil Storage*. Washington, DC. API Standard No.650: American Petroleum Institue, 2013.

[4]   American Society of Civil Engineers, *ASCE-7-16: Minimum Design Loads for Building and other Structures*. Reston, VA.: ASCE-7-16, 2016.

[5]   P. Macdonald, K. Kwok, and J. Holmes, "Wind loads on circular storage bins, silos and tanks: I. Point pressure measurements on isolated structures," *Journal of Wind Engineering and Industrial Aerodynamics,* vol. 31, no. 2-3, pp. 165-187, 1988.

[6]   Y. Uematsu, C. Koo, and J. Yasunaga, "Design wind force coefficients for open-topped oil storage tanks focusing on the wind-induced buckling," *Journal of Wind Engineering and Industrial Aerodynamics,* vol. 130, pp. 16-29, 2014.

[7]   Joint Standards Australia/Standard New Zealand Standard, *AS/NZS 1170.2: 2011 Structural design actions-Part 2: Wind actions*. Sydney, NSW, Australia, 2011.

[8]   European Committee for Standardization, *Eurocode 3: Design of Steel Structures, Part 4.1: Silos*. Brussels, Belgium.: Standard No. EN 1993-4-1, 2007.

[9]   J. Yasunaga and Y. Uematsu, "Dynamic Buckling of Cylindrical Storage Tanks under Fluctuating Wind Forces," (in Japanese), *Journal of Wind Engineering,* vol. 43, no. 2, 2018.

[10]   E. M. Sosa and L. A. Godoy, "Nonlinear dynamics of above-ground thin-walled tanks under fluctuating pressures," *Journal of sound and vibration,* vol. 283, no. 1-2, pp. 201-215, 2005.

[11]   F. G. Flores and L. A. Godoy, "Forced vibrations of silos leading to buckling," *Journal of Sound and Vibration,* vol. 224, no. 3, pp. 431-454, 1999.

[12]   Y.-C. Chiang and S. Guzey, "Influence of Internal Inward Pressure on Stability of Open-Top Aboveground Steel Tanks Subjected to Wind Loading," *Journal of Pressure Vessel Technology,* vol. 141, no. 3, p. 031204, 2019.

2. DYNAMIC ANALYSIS OF ABOVEGROUND OPEN-TOP STEEL TANKS SUBJECTED TO WIND LOADING

Summary

Aboveground steel tanks are prone to buckle under wind loading if they are empty. Geometrically nonlinear explicit dynamic analysis of empty open-top tanks subjected to wind loading are conducted using finite element analysis (FEA). Tanks with five different height to diameter aspect ratios, 4.0, 2.0, 1.0, 0.4, and 0.2, are adopted. Tanks are subjected to a gust of wind which fluctuates in magnitude over time to investigate whether a minor fluctuation, 10% of the average pressure, will trigger resonant behavior. Tanks with geometrical imperfections are also investigated using both dynamic analysis and static geometrically nonlinear analysis including imperfection (GNIA). It is found that, no matter if the tank does or does not have geometrical imperfections, resonance is not observed. Thus, a static analysis may be adequate for a practical tank design. The natural vibration frequencies of empty open-top tanks is studied as well, and comparisons with a theoretical solution and FEA results from the literature are presented. The effective modal mass is discussed to investigate the dynamic characteristics of the tanks examined. Insights for conducting an explicit dynamic analysis, including converged mesh size and time step limits, are also presented.

2.1 Introduction

Aboveground storage tanks are widely used to store liquid in various industries [1, 2]. These tanks are typically composed of several courses of thin steel shells, which are predominantly designed to withstand the internal hydrostatic pressure caused by the stored liquid [3, 4]. Many design approaches have been developed focusing on properly designing these shells with minimum wasted material [4-6]. As a consequence, shell thickness can be as thin as 1/2000 times of its radius [7]. Due to this geometrical slenderness, aboveground storage tanks are vulnerable to buckling induced by external pressure such as pressure caused by wind, internal pressure caused by a vacuum inside a tank, seismic excitation, etc.

Zingoni [1] reviewed recent research on liquid-containment shells of revolution mainly focusing on strength, stability, and dynamics aspects. In addition, Godoy [2] provided a survey on recent studies on buckling of vertical axis oil storage steel tanks with an emphasis on static buckling research. When the tank has liquid in it, external loads caused by seismic events need to be taken into consideration. Behavior of tanks during seismic events, including sloshing of the liquid inside a tank, has been widely studied [8-17]. However, when the tank is empty, buckling due to wind load plays a more important role. To prevent tanks from general buckling, where the upper edge of the tank can no longer maintain its circular profile, wind girders are installed on open-top tanks. The expression for sizing wind girder prescribed by API 650 [4] was first presented in an American Water Work Association (AWWA) document [18]. Later, extensive research was dedicated to sizing the wind girder properly and economically due to the overly conservative nature of the API 650 and AWWA approaches [3, 19-24].

To understand the effect of wind loads on tanks, boundary layer wind tunnel (BLWT) physical testing has been conducted by many research groups [25-29]. It was determined that for tanks with and without a fixed roof, the circumferential pressure distribution can be very different. Using the wind profile obtained from the BLWT tests, research efforts have been dedicated to theoretical and static analyses to investigate the buckling behavior of tanks with various geometries, most of which included geometric imperfections [21, 27-31]. Resinger and Greiner [21] proposed a guideline for design pertaining to buckling under wind loading. The wind profile on the circumferential shell obtained from the wind tunnel test was converted to a uniform pressure profile, which simplified the design process. Furthermore, a guideline for sizing wind girders was also provided. Greiner and Derler [30] investigated the effect of different imperfection profiles on the buckling capacity using static analysis. It was reported that the taller the cylindrical shell is, the less sensitive it is to geometric imperfection. Moreover, if a tank is subjected to a uniform pressure profile, an analysis including imperfections may not be needed. Portela and Godoy [27, 28] conducted geometrically non-linear analyses on conical and dome roofed tanks including geometric imperfections. They concluded that there is little difference in buckling behavior of the cylindrical shell with conical roof or dome roof tanks.

Uematsu et al. [29] conducted wind tunnel tests for tanks with aspect ratios (*H/D*) of 0.5 and 1.0, where *H* is the tank height, and *D* is the tank diameter. The pressure distribution and buckling capacity of the tanks were obtained from the tests and the buckling capacities were then compared to the theoretical solutions [32]. It was found that because the theoretical solutions [32] were derived from static equilibrium, the theoretical buckling capacities did not compare favorably with the buckling capacities obtained from the wind tunnel tests. While Uematsu and coworkers did not suggest that dynamic analysis be conducted, there is a need for such analyses. Recently, Uematsu et al. [31], performed wind tunnel experiments on tanks with aspect ratios of 0.25, 0.5, and 1.0 to obtain the circumferential pressure distributions and the buckling loads. They further conducted non-linear static analyses to investigate the effect of roof configuration on the buckling capacities, and proposed a practical pressure distribution for design. Though static analysis of tanks is prevalent, there is limited research on the dynamic characteristics of tanks under wind loading. Some researches studying the natural vibration frequencies of cylindrical shells has been conducted [33-36], but minimal research has been conducted using dynamic analysis to investigate buckling induced by wind.

Flores and Godoy [37] conducted dynamic analysis to investigate the buckling capacity of silos. Silos with aspect ratios of 0.357 and 1.54 were examined, including silos with and without roofs, and silos with corrugated walls. An external wind load was applied as a step function in time domain rather than an impulse function. To identify a buckled configuration using a dynamic analysis, the criterion proposed by Budiansky and Roth [38] was employed. It was then found under the above condition that the buckling capacity obtained from a dynamic analysis and from a non-linear static analysis were close, with a maximum of a 5% decrease in the buckling capacity observed between the dynamic and static analyses. It was also reported that silos without a roof were found to have a significantly lower buckling load, with only 50% of the buckling capacity of a complete silo with a roof. This significant reduction in buckling capacity was reasonable due to the absence of a top wind girder in the tank models without a roof.

Later, Sosa and Godoy [7] examined the buckling capacity by employing an impulse load function in the time domain and conducting a dynamic analysis. The purpose of their study was to see whether resonance would occur when the external wind load fluctuated at or near the tank's first, lowest natural vibration frequency. The first natural vibration period of tanks are much shorter

than 3 seconds, while the design wind speed in ASCE-7 is an averaged wind speed over a period of 3 seconds [39]. A minor fluctuation with a vibration period of less than 3 seconds may cause resonance on the tank shell. The study focused on a tank with a height to diameter aspect ratio of 0.4 and a fixed conical roof. Rafters which support the conical roof were also modeled during the analysis. In their study, the first natural vibration frequency was obtained using a general purpose finite element code, and this frequency was used as a fluctuation frequency for the linear (saw-tooth) impulse applied during the dynamic analysis. Several other fluctuation frequencies were also utilized as well. However, the buckling capacity obtained from using an impulse load and from using a step load did not differ significantly. Thus, it was concluded that no resonance was observed throughout the study. Later, Uematsu et al. [40] stated that dynamic analysis was also conducted on open-top tanks by Yasunaga [41]. Yasunaga [41] suggested the stress distribution was not greatly affected by resonance.

The present study aimed to provide information about how open-top tanks with different aspect ratios behave under different wind load patterns, and to investigate whether resonance would be observed in any of these setups. Tanks with height to diameter aspect ratios of 0.2, 0.4, 1.0, 2.0, and 4.0 were adopted. Using a finite element program, explicit dynamic analysis was conducted. In the analyses, tanks were subjected to a gust of wind whose amplitude fluctuated with respect to time. A wide range of fluctuation periods were employed, including the first natural vibration frequency of the tanks and the frequencies associated with the mode producing the highest effective modal mass in the windward direction. To ensure that the natural vibration frequencies obtained by finite element analysis (FEA) were correct, frequencies reported by Virella et al. [36] and a theoretical solution compiled by Blevins [42] were adopted as benchmark solutions. The effect of fluctuation amplitude and wind gust duration on the dynamic behavior of the adopted tanks were also investigated.

Also, to conduct a precise dynamic analysis, a small time step and a relatively fine mesh are needed. Analyses with different time steps were conducted to investigate how small a time step should be implemented to make an analysis stable. Three different criteria for a time step limit were adopted (1) the built-in time step in the general purpose finite element package ABAQUS [43], (2) the time step limit proposed by Belytschko et al. [44], (3) the time step limit proposed by

Tong and Tsui [45]. Similarly, a mesh convergence study was conducted using a particular tank configuration with different mesh sizes. Dynamic analyses with a step function in time domain were employed in the mesh convergence study, and the converged mesh size was reported.

Furthermore, tanks with geometric imperfections were also studied. Dynamic analyses were conducted using tanks with various imperfection amplitudes. To compare the difference between dynamic and static analyses, geometrically nonlinear analysis including imperfection (GNIA) was also performed.

2.2   Methodology

2.2.1   Tank Modeling

Five different size empty open-top tanks were investigated in this study, with diameter of 3.05 m (Tank A), 6.10 m (Tank B), 12.2 m (Tank C), 30.5 m (Tank D), and 62.0 m (Tank E), respectively. All of the five tanks were 12.2 m in height, and were composed of five 2.44 m high shell courses. The height to diameter aspect ratio of the five tanks were 4.0, 2.0, 1.0, 0.4, and 0.2, respectively. These tanks were modeled using a general purpose finite element program, ABAQUS version 2018 [43]. Shell course thickness information for all five tanks can be found in Table 2-1. The shell thickness of tanks A, B and C were sized according to the one foot method and minimum shell thickness specified in API 650 [4], while Tank E was designed using variable design point method given in API 650. For tanks A, B, C and E, the allowable stress of the steel was set as 159 MPa, the specific gravity of the product within the tanks was set to 1.0, and the corrosion allowance was set to zero. For Tank D, geometry including shell thickness, height, and diameter were consistent with the tank studied by Virella et al. [36], which made the results comparable. Note that the tanks included in the work done by Virella et al. [36] were tanks with fixed roofs at the top of the tanks while the tanks in this study are open-top tanks without a fixed roof, but with top wind girders to maintain the circular profile at the top edge of the shell.

The top wind girders were designed in compliance with API 650, using a design wind speed of 190 km/h. However, no intermediate wind girders were modeled even if API 650 prescribed an intermediate wind girder. Only Tank E actually required an intermediate wind girder. The details

of the top wind girders adopted are compiled in Table 2-2. For Tank C, the top wind girder was an angle with short leg vertical.

The material used in this study was a mild carbon steel, which has a modulus of elasticity $E = 200$ GPa, a Poisson's ratio $v = 0.3$ and a mass density $\rho = 7900$ kg/m^3. No material non-linearity was considered. To improve the efficiency of the analysis, an S4R element, which is a 4-node, reduced integration, quadrilateral shell element with large strain formulation [43], was used. For the boundary conditions, the bottom of the shell was fixed and the top edge of shell was free. Fixed boundary condition at the bottom of shell was used by Sosa and Godoy [7] and Azzuni and Guzey [3], among many others. Sun et al. [20] pointed out that fixed boundary condition at the bottom of the shell may produce slightly larger buckling capacity than pinned boundary condition due to strengthening effect at the lower part of the shell. No damping was applied to any of the models in this study.

With respect to mesh sizes, for the purposes of this study, even a relatively coarse mesh should be enough for capturing the resonance behavior. For the sake of consistency between different models, an index of global mesh size, $\beta\sqrt{Rt}$, was defined. Here, β is a mesh scaling factor, t is the thinnest thickness of the shell, and R is the radius of the shell. The mesh scaling factor β was chosen to be 0.5 for Tanks A and B. On the other hand, β was chosen to be 1.76 for Tanks C, D and E, except for the mesh convergence study in section 2.2.7. This rather large mesh size resulted in high analysis efficiency. On the other hand, a rather small mesh was chosen for Tanks A and B, and the reasoning will be presented in section 2.3.3. The approximate mesh size for Tanks A, B, C, D and E were 4 cm, 6 cm, 30 cm, 60 cm, and 85 cm, respectively. A model of Tank D is presented in Figure 2-1.

2.2.2 Dynamic Analysis

An explicit dynamic analysis was carried out in this study. In explicit dynamic analysis, the displacement and velocity are directly calculated based on the former time increment, while the mass matrix as well as the stiffness matrix are assumed to be known. This results in a relatively high analysis efficiency compared with implicit analysis [46]. In the explicit dynamic analysis, the central-difference integration rule, which is conditionally stable, was adopted. In order to ensure

the stability of the numerical method, a sufficiently small time increment is needed. In ABAQUS, the maximum time step limit was selected using the linear von Neumann criteria [44], and can be given as Eqn. (1)

$$\Delta t \leq \alpha \frac{L_{min}}{c_d} \tag{1}$$

Here, α is a scaling factor, L_{min} is the smallest element length dimension (mesh size), and c_d is dilatational wave speed, which can be calculated using the Eqn. (2).

$$c_d = \sqrt{\frac{\lambda + \mu}{\rho}} \tag{2}$$

In Eqn. (2), where ρ is mass density, and λ is Lamé's first parameter which can be calculated using Eqn. (3).

$$\lambda = \frac{E\nu}{(1 + \nu)(1 - 2\nu)} \tag{3}$$

where μ is shear modulus, and is calculated using Eqn. (4).

$$\mu = \frac{E}{2(1 + \nu)} \ . \tag{4}$$

If a time step is not specified during the analysis, ABAQUS [43] generates a time step using an α value ranging from 0.707 to 1, while Belytschko et al. [44] suggested using a value between 0.2 and 0.9 for α. On the other hand, Tong and Tsui [45] proposed another time step limit, which can be expressed as given in Eqn. (5).

$$\Delta t \leq \left[\frac{\frac{\rho(1 - \nu^2)}{E}}{2 + \left(\frac{1}{12}\right)(1 - \nu)\pi^2[1 + (3/2)(L_{min}/h)^2]} \right]^{1/2} L_{min} \tag{5}$$

where h is the thickness of a uniform cylindrical shell. In this study, analyses were conducted adopting both the ABAQUS built-in time step and the time step proposed by Tong and Tsui [45] and suggestions based on Belytschko et al. [44] were also discussed.

The wind gust duration used during the analysis should also be considered. Previously, Sosa and Godoy [7] used a wind gust duration of 3 seconds. Nevertheless, Sosa [47] later suggested that extending the wind gust duration may be something worth investigating. Therefore, a wind gust duration of 9 seconds was adopted in this study.

2.2.3   **Dynamic Buckling Criterion**

The criterion for dynamic buckling employed by this study was defined by Budiansky and Roth [38]. This criterion considered the displacement response of the node which had the maximum displacement under different levels of pressure (λ). The minimum pressure level which yielded a steep increase in displacement response compared to a slightly lower pressure level was defined as the "dynamic buckling load", and denoted as λ_{cr}. In other words, dynamic buckling capacity is the lowest level of pressure that results in a large displacement response, which in this study is defined as the maximum displacement of the buckled model which is at least an order of magnitude larger than a model in which buckling did not occur.

2.2.4   Natural Vibration Frequencies

In general, if a structure is loaded dynamically and the loading frequency is at or near the structure's one of the natural vibration frequencies, the structure should encounter a resonance [48, 49]. In this case, resonance should yield a significantly lower buckling capacity compared with a loading frequency that does not closely corresponded with the resonant vibration frequency. The response of a structural system subjected to a periodic external load usually displays a maximum response when the external load fluctuates at the first natural vibration frequency of the system. Therefore, the natural vibration frequencies of the tanks are discussed next.

Previously, Virella et al. [36] conducted FEA of tanks with various roof configurations and open-top tanks without wind girders, while in this study, open-top tanks with wind girder were studied. Due to the similarities in the tank geometries, the study done by Virella et al. [36] was used as a benchmark solution in this study.

Also, a theoretical solution for the natural vibration frequencies of a cylindrical shell with uniform thickness which was derived by researchers and compiled by Blevins [42] was also adopted as a benchmark solution in this study. The natural vibration frequencies can be expressed by Eqn. (6)

$$f_{ij} = \frac{\lambda_{ij}}{2\pi R}\left[\frac{E}{\rho(1-v^2)}\right]^{1/2}$$

(6)

where λ_{ij} is related to the boundary conditions and is defined using as follows:

$$\lambda_{ij}{}^2 = \frac{(a_{11}a_{22}a_{33} + 2a_{12}a_{13}a_{23} - a_{11}a^2{}_{23} - a_{22}a^2{}_{13} - a_{33}a^2{}_{12})i^4}{(a_{11}a_{22} - a^2{}_{12})(\beta_j{}^2\alpha_2 + i^4 + i^2)}$$

(7)

$$a_{11} = \beta_j{}^2 + \frac{1}{2}(1+k)(1-v)i^2\alpha_2 \tag{8}$$

$$a_{12} = -vi\beta_j\alpha_1 - \frac{1}{2}(1-v)i\beta_j\alpha_2 \tag{9}$$

$$a_{13} = -v\beta_j\alpha_1 - k\beta_j[-\beta_j{}^2 + \frac{1}{2}(1-v)i^2\alpha_2] \tag{10}$$

$$a_{22} = i^2 + \frac{1}{2}(1+3k)(1-v)\beta_j{}^2\alpha_2 \tag{11}$$

$$a_{23} = i + ki\beta_j{}^2[v\alpha_1 + \frac{3}{2}(1-v)\alpha_2] \tag{12}$$

$$a_{33} = 1 + k[\beta_j{}^4 + (i^2-1)^2 + 2vi^2\beta_j{}^2\alpha_2] \tag{13}$$

$$\beta_j = \frac{\lambda_j R}{L} \tag{14}$$

$$k = \frac{h^2}{12R^2} \tag{15}$$

where i is the number of circumferential waves, j is the number of axial half-waves, h is the thickness of the uniformly thick cylindrical shell, L is the length of the cylinder, and parameters such as $\underline{\lambda}_j$, α_1, and α_2 are related to the boundary conditions. For the boundary conditions adopted in this study, the bottom edge of the tank shell was assumed to be fixed, and the top edge with a top wind girder keeping the circular shape of the shell can be considered as a pinned boundary condition in the horizontal direction (radial and circumferential direction) and free in the axial direction [3]. As a consequence, a pinned-fixed boundary condition was adopted for calculating the first natural vibration frequency theoretical solution. For this boundary condition case, $\underline{\lambda}_j$ is 3.927 when $i=1$ (which is common for lower modes), and both α_1 and α_2 are 0.7467. Furthermore, to make the frequency of a stepped thickness cylindrical shell considered in this study compatible with Eqn. (6), which is only applicable for a uniformly thick cylindrical shell, the average of the thickness of the stepped thickness cylindrical shell is used in Eqn. (6). Han and Liu [50] reported that the first natural vibration frequency for a cylindrical shell that has a specific uniform thickness h or a cylindrical shell whose shell thickness has an average of h but varies linearly would be similar.

2.2.5   Wind Action

As stated previously, a wind gust duration of 9 seconds was used for most of the cases during the dynamic analyses. Different fluctuation periods, T_f, and fluctuation functions were selected to investigate whether the tanks would experience resonance during these loading situations. An

example time history of a gust of wind considered in this study is shown in Figure 2-2, where the
x-axis is time in seconds and the *y*-axis is the amplitude of the applied wind pressure. Note that the
adopted wind action model might be far from the actual fluctuation pattern, but this kind of
periodic load should be a worst case scenario to the tanks. Fluctuation period T_f was varied from
0.05 seconds to 3 seconds, including the first natural vibration frequency, to consider whether any
period less than 3 seconds would trigger the resonant behavior in the shell. Both linear (saw-tooth)
and sinusoidal fluctuations were considered, and the fluctuation amplitude P_f for both functions
were set to 0.1 times of the average gust pressure P_{ave} to represent a minor fluctuation ($P_f = 0.1P_{ave}$).
When the displacement response of a tank met the criterion of buckling established in previous
section under a certain level of external pressure P_{ave}, that pressure was selected as the buckling
load, λ_{cr}, of the tank.

The relationship between of wind speed and pressure can be found in ASCE 7-10 [51] and ASCE
7-16 [39]. The wind profile specified in ASCE 7 [39, 51] and API 650 was constant on the
projected areas of a cylindrical shell along circumferential direction and changing only along
vertical direction. The constant pressure along circumferential direction assumption was not
adopted in this study because it is not a realistic wind profile distribution of pressure on a
cylindrical tank. The wind profile used in this study was provided by the European code EN 1993-
4-1 [52] and can be expressed as Eqn (16).

$$
\begin{aligned}
C_p(\theta) = {} & -0.54 + 0.16(D/H) + [0.28 + 0.04(D/H)]cos(\theta) \\
& + [1.04 - 0.20(D/H)]cos(2\theta) + [0.36 - 0.05(D/H)]\,cos(3\theta) \\
& - [0.14 - 0.05(D/H)]\,cos(4\theta)
\end{aligned}
\tag{16}
$$

where C_p is the normalized circumferential pressure distribution, and θ is the circumferential
angular position in degrees. Note that for open-top tanks, an additional internal pressure of 0.6
should be added to the normalized circumferential pressure. In other words, if a gust of wind blows
at a certain velocity would generate 1.0 Pa of pressure (λ) when there is no obstacle, it generates
1.6 Pa of pressure on the windward side ($\theta = 0$) of an open-top tank. The wind pressure distribution
along the circumferential direction is shown in Figure 2-3. The wind speed was assumed to be
independent of the height of the tanks since the heights of the adopted tanks were relatively short
with a height of 12.2 m and thus the vertical pressure distribution was assumed to be constant. This
assumption was not far from provisions in ASCE 7, EN 1993-4-1, and API 650.

2.2.6   Validation of Wind Action

The wind action model adopted in the present study assumed that the circumferential wind distribution shape would not vary with respect to time and represented the mean circumferential distribution. Without taking a time varying distribution, time-space correlation, into account, the buckling capacity obtained would be questionable.

Therefore, to validate the adopted wind action model, the work done by Yasunaga and Uematsu [53] was considered as a benchmark. Yasunaga and Uematsu [53] conducted a BLWT study using two scaled tanks to obtain the circumferential wind distribution at every instant during a gust of wind, and the distribution was used as the input for a ABAQUS finite element dynamic analysis. In other words, time-space correlation was taken into account. In this section, the results obtained using a constant circumferential wind distribution with respect to time were compared with the results presented by Yasunaga and Uematsu [53] to investigate how the buckling capacities differed with these two wind profile.

The dimensions of the tanks studied by Yasunaga and Uematsu [53] are presented in Table 2-3. A tank with uniform thickness was adopted rather than a stepped thickness tank. The material selected was steel with $E = 205$ GPa, and $v = 0.3$. The element type selected was S4R quadrilateral shell element of ABAQUS. The number of element on the circumference and the height of the tanks were 360 and 100, respectively, for both models. The boundary condition of the bottom of the tank shell was set to be fixed and there were two types of boundary condition at the top edge of the tanks. One of which fixes the top edges of the tanks, and the other is free boundary condition. These two boundary conditions were labeled as fixed and free in Table 2-3.

The first natural vibration frequency, the circumferential wave number on the tank shell of the first mode, the buckling capacity obtained from a static analysis, and the buckling capacity obtained from an implicit dynamic analysis were compared in this section. The first natural vibration frequency and the circumferential wave number on the tank shell were also computed to ensure the models in the present study were identical to those modeled by Yasunaga and Uematsu [53]. Yasunaga and Uematsu [53] conducted a static analysis using Riks analysis with geometrically perfect tanks subjected to wind loading with a mean circumferential distribution to obtain the

buckling capacity. The author, however, decided to conduct LBA to obtain the static buckling capacity, since without any imperfection, Riks algorithm may not be able to properly capture the bucling behavior. Besides, without any imperfections, the capacities obtained using Riks analysis and LBA should be similar for the aspect ratios of thanks under consideration.

Yasunaga and Uematsu [53] conducted an implicit dynamic analysis since they recorded the circumferential wind distribution during the BLWT testing every 0.001 seconds. For an explicit dynamic analysis, this was a large time step that may cause divergence of the analysis, but for an implicit dynamic analysis with the model constructed, this time step size was acceptable. As a consequence, the circumferential distribution at every instant could be employed without any extra interpolation or post-processing. An implicit dynamic analysis was adopted by the author in this section as well, but the circumferential wind distribution and the velocity pressure did not vary with respect to time. In other words, the wind load was applied as a step load in this section.

The results of the FEA, including the first natural vibration frequency, wave number on the shell of the first natural vibration mode, the static buckling capacity, and the dynamic buckling capacity are presented in Table 2-4. Note that the buckling capacity presented in this section was the pressure on the shell rather than the velocity pressure. In other words, the reported pressure level was $C_p(0°)\lambda_{cr}$. It sould be observed that all the results in Table 2-4 are fairly close between this study and Yasunaga and Uematsu study. The difference between the first natural vibration frequencies was no more than 0.2% and the circumferential wave numbers matched. This indicates that the model in present study is very similar to the Yasunaga and Uematsu [53] modeled. The difference in static buckling capacities is around 10%. This difference may be a result of the difference in the adopted wind pressure distribution. The dynamic buckling capacities are almost identical. Case 4 in Table 2-4 has the most difference, 4%, between dynamic buckling capacities. Since there is not a dramatic difference in buckling capacities obtained by two methodology, it can safely be concluded that the buckling capacities obtained from present analysis, which did not consider the time-space correlation, did not distinguish themselves from the buckling capacities obtained from analysis in which the time-space correlation was taken into account.

2.2.7 Mesh Convergence Study

The mesh convergence study was conducted to provide a guideline for future researches, which may need a more precise result. Rawat et al. [54] conducted a mesh convergence study using cylindrical shells with aspect ratios ranging from 1 to 10. However, a good portion of open-top storage tanks may have an even smaller aspect ratios [55], and, therefore, more information on mesh convergence is needed. In this study, a step load in the time domain was applied on Tank D, to investigate how small the mesh scaling factor β should be to make the buckling capacities converge.

2.2.8 Effect of Imperfection

It is well known that imperfections have a great impact on the buckling capacity of a tank when subjected to wind loading. According to Godoy and Flores [56], for tanks with aspect ratios ranging from 0.16 to 1.0, tanks with smaller aspect ratios are more sensitive to imperfections. Thus, in this study, dynamic analysis with imperfections was conducted using Tank E to investigate the influence which geometric imperfection have.

Eigenmode-affine imperfection shape based on the first buckling mode shape obtained from LBA scaled with an imperfection amplitude was used. In this procedure, the perfect initial geometry of the mesh nodal coordinates were moved with the amount of scaled first buckling mode shape and after that the desired dynamic analysis were performed using this imperfect geometry. The first buckling mode shape, which has the most impact on the buckling capacity of a tank subjected to wind loading comparing with higher mode shapes, used as imperfections [20]. The thinnest shell thickness t was used as a reference for the magnitude of the imperfection amplitude, and analyses with different levels of imperfection amplitudes were performed. Imperfection amplitudes of $0.1t$, $0.25t$, $0.5t$, $0.75t$, and $1t$ were employed, as those magnitudes of imperfection have been widely adopted by other researchers [3, 7]. In addition, static GNIA was performed under the same imperfection levels to provide a comparison of the buckling capacities obtained between the dynamic analysis and the static GNIA.

2.3   Analysis and Discussion

The present study reports the results of dynamic analyses of five open-top, flat-bottom tanks under wind loading using FEA. To investigate whether a tank would encounter resonance when the external load fluctuates at or near its first natural vibration frequency, the first natural vibration frequency was first obtained and was compared with published results based on FEA and theoretical solutions. The effective modal mass in the windward direction was determined as well. Once the first natural vibration frequency was obtained, explicit dynamic analyses with and without imperfections were conducted. Next, the influence of wind gust duration as well as the fluctuation amplitude of the wind on the buckling behavior were discussed. Moreover, studies on time step and mesh refinement were conducted as well. Different available maximum time step limit criterions were adopted to investigate the time step size that result in a stable analysis. A mesh convergence study provided the information about how fine a mesh should be used to conduct a precise analysis.

2.3.1   Natural Vibration Frequencies of Tanks

The natural vibration frequencies of the five tanks were obtained using FEA and compared to the benchmark solutions mentioned previously. The first three vibration frequencies and corresponding wave numbers of all five tanks obtained using the FEA and the theoretical solution [42] are compiled in Table 2-5. Note that for Tanks A and B in Table 2-5, the top edge of the shell was pinned in the horizontal direction, since for these tall tanks, the wind girder was no longer stiff enough to keep the circular profile of the upper edge. In other words, without the pin boundary condition, the wind girder simulates a boundary condition between a pinned and free end, and correlates more to a free end condition. The first eigen mode shape for Tanks A and B without a pinned top edge are shown in Figure 2-4, and the resulting first natural vibration frequencies were 7.728 Hz and 7.549 Hz, respectively.

In Table 2-5, the results obtained from the theoretical solution and the FEA are relatively close to each other, and they had even better agreement when a finer mesh is adopted. For Tanks A, B, and C, whose shell thicknesses were closer to a uniform thickness, the result of the FEA are also very close to the theoretical solutions, which all have a difference less than 2% between the result of the FEA and theoretical solutions. Similarly, there is a difference of approximately 1% to 4%

between the results of the FEA and theoretical solutions for Tanks D and E. It is noteworthy that, although the theoretical solution provided by Blevins [42] was not based on a stepped thickness cylindrical shell, but rather a uniform thickness, and the tops of Tanks C, D and E were not a perfect pinned-end condition, this theoretical solution still gave a good estimation of the first three natural vibration frequencies of all the tanks. Note that, for the frequencies reported, only the frequencies whose mode shapes resulted in shell vibration were reported and modes with repeated eigenvalues were only reported once.

The first three natural vibration frequencies of Tank D obtained by the FEA and the comparable results reported by Virella et al. [36] are compiled in Table 2-6. Table 2-6 shows that even when the roof configurations are different, the first three natural vibration frequencies of the tank shells with the same diameters are relatively close. The frequencies of the open-top and the tanks with the rafter-supported roof have even better agreement, with the difference of first natural vibration frequencies among these tanks types being approximately 1%. Although the tanks without the rafters have a slightly lower frequencies, the difference between open-top tank and the tank with self-supported roof was only about 5%.

By extracting the natural vibration frequencies and eigen mode shapes, the effective modal mass could be discussed. Effective modal mass is a property that can be calculated based on generalized mass, modal participation factor, and mode shape. Effective modal mass was reference to evaluate the extent a mode would be excited by wind gusts in the windward direction, as a high effective mass indicates a high response under external excitation [57]. Note that for all of the following discussions, the pin boundary condition at the top edge of Tanks A and B was removed, in favor of a free condition. Figure 2-5 presents the effective mass normalized with respect to the total mass of tank of each modes with respect to each model's natural vibration frequency. For all five subfigures in Figure 2-5, the effective mass adds up to be at least 80% of the total mass. It was surprising that for all five tanks, the mode which had the most effective mass were not the first modes, and the first modes had little contribution in the reaction in the windward direction. The modes which had the most effective mass for Tanks A, B, C, D, and E were the 11th, 79th, 244th, 534th, and 753rd modes, respectively. The mode shape of the first mode and the mode with the most effective mass contribution in the wind direction are plotted in Figure 2-6 to Figure 2-10. In Figure

2-6 to Figure 2-10, the subfigures (a) and (b) are the top view and elevation view of the first mode, respectively. Similarly, subfigures (c) and (d) are the top view and elevation view of the dominant mode. It should be observed that the higher the aspect ratio, the mode with the most effective mass in the windward direction (the dominant mode) appears in early modes. In addition, the dominant modes are the cantilever modes for all five tanks. It is noteworthy that for the dominant mode of Tank E, there is some irregular on the shell rather than a pure cantilever mode. The presented result indicates that resonance may actually happen when the external load fluctuates at the dominant frequency rather than the first natural vibration frequency.

Using the results obtained above, the first natural vibration frequencies as well as the frequencies which has the most effective modal mass were used as parameters in the dynamic analyses. Next, the results of dynamic analyses shall be presented.

2.3.2   Results of Dynamic Analysis of Broader Tanks (Tank C, D and E)

To illustrate the buckling behavior of a tank subjected to wind loading, the results of the dynamic analysis of Tank E, which was subjected to a step load, and a constant pressure distribution in time domain, are shown in Figure 2-11. The global mesh size was set to 85 cm (scaling factor $\beta = 1.76$). In Figure 2-11(a), the tank is subject to a gust of wind with a wind pressure level λ of 980 Pa. There is only subtle deformation on the tank shell with a maximum displacement of 0.27 cm. However, when the pressure level was increased slightly to 1000 Pa, as shown in Figure 2-11(b), the magnitude of deformation increases dramatically to a maximum displacement of 17 cm. As a result of the more than ten times increase in displacement with only a 2% increase in external pressure, this meets the buckling criterion proposed by Budiansky and Roth [38]. Note that a series of analyses with different wind pressure levels were conducted, and the deformed shape under the two most critical pressure levels are presented in Figure 2-11.

Using the dynamic buckling criterion defined earlier, buckling under various circumstances were studied. Analyses with step loading in time domain and linear impulse loads with various periods (see Figure 2-2 and Figure 2-3 for loading profiles in time and space domains, respectively) were conducted, and the result of the analyses are shown in Figure 2-12. The global mesh size was set to 40 cm, 60 cm, and 85 cm (mesh scaling factor $\beta = 1.76$) for Tank C, Tank D, and Tank E,

respectively. The buckling capacities were obtained with a 50 Pa increment and the time step used in these analyses was the ABAQUS built-in time step. An LBA was also conducted for all three tanks and the linear buckling capacities are 1705, 1624, and 1010 Pa for Tank C, Tank D, and Tank E, respectively. It is observable that at some fluctuation periods, the buckling capacity could decrease up to 15% compared with the step loading scenario in time domain, but it was not considered to be resonance nor a significant decrease in buckling capacity for all three tanks. This structural response is similar to what Sosa and Godoy [7] reported. It is also observable the lowest buckling capacity did not coincide with the first natural vibration frequency or the frequency with the highest effective modal mass, and that buckling capacities are usually lower when the fluctuation period is longer.

To investigate influence of different fluctuation functions in time domain, sinusoidal functions were adopted as well and this analysis was conducted using Tank E. The global mesh size was set to be 85 cm (mesh scaling factor $\beta = 1.76$), and the time step was the ABAQUS built-in time step. The results of the linear (saw-tooth) impulse loads and sinusoidal impulse loads with the same series of fluctuation periods and an amplitude of $0.1P_{ave}$ are presented in Figure 2-13. The buckling capacities obtained from both types of fluctuation functions for the majority of the frequencies adopted are almost identical. It should be observed that the tanks may not encounter resonance when the load was applied as a linear or sinusoidal impulse function.

This phenomenon is interesting because a typical structure should display resonant behavior when an external excitation force vibrates at first natural vibration frequency of the structure or in this case, at the frequency of the mode with the most effective mass. Take a single degree of freedom system as an example. When it is subjected to a periodic external excitation at a frequency that happens to be close to the first natural vibration frequency of the system, the response would be very large. Moreover, for systems without damping, the response would be infinite [49]. However, resonance was not observed even when periodic loads with a wide range of frequencies were applied in this study.

2.3.3   Results of Dynamic Analysis of Taller Tanks (Tanks A and B)

The observed dynamic buckling behavior of taller tanks (e.g. Tank A and B) was different from the behavior of broader tanks discussed in the previous section. As discussed in Section 2.3.1, a cantilever mode dominated the behavior in tall tanks and greatly affected the buckling capacity of Tanks A and B. To better understand this phenomenon, the mesh scaling factor β was set to 0.5, a relatively finer mesh comparing with that of used in broader tanks. The LBA buckling capacities of Tanks A and B were 20130 Pa and 5992 Pa, respectively. The wind pressure was applied to fluctuate linearly (saw-tooth shape), and the fluctuation amplitude was set to 10% of the average wind pressure. The dynamic buckling capacity of Tank A could not be clearly defined due to dominant cantilever mode deformation of the tall tank. On the other hand the dynamic buckling capacities of Tank B are identified and compiled in Figure 2-14.

The deformed shapes of Tank A subjected to wind loading fluctuating at its first natural vibration frequency are presented in Figure 2-15 and Figure 2-16 at two load levels λ. Subfigures (a) and (b) in Figure 2-15 and Figure 2-16 are the top view and the elevation view of the deformed shape. The maximum displacement throughout the history of the whole model is 29.6 cm and 50.5 cm for load levels $\lambda = 7000$ Pa and $\lambda = 8000$ Pa, respectively. This is not a significant difference in terms of displacement magnitude, and thus could not be stated as dynamic buckling following the Budiansky and Roth [38] buckling criterion adopted previously. The deformed shapes, however, are clearly distinct from one another. In Figure 2-16 for $\lambda = 8000$ Pa, a buckled shell can be observed through the concave deformed shell. In contrast, Figure 2-15 for $\lambda = 7000$ Pa, the deformed shell is not as concave, and it can be noticed that the top edge of Tank A under this loading scenario is not circular. One possible reason for this phenomenon would be the fact that wind girder was sized according to a much lower wind speed, the wind girder was not able the maintain the circular profile of the top edge at $\lambda = 7000$ Pa. This phenomenon also occurred between $\lambda = 7000$ Pa and $\lambda = 8000$ Pa for several other runs with different fluctuation frequencies. Therefore, if we increase the size of the wind girder we may identify the $\lambda = 8000$ Pa load level as dynamic buckling load. It is interesting that this pressure level was only about 40% of the LBA buckling load level. However, these results did not indicate a resonance because this dynamic buckling load level was obtained for various wind fluctuation frequencies.

Similarly, comparing the dynamic buckling capacity in Figure 2-14 for Tank B with the LBA results, a more than 25% drop in buckling capacity between dynamic analysis and LBA is observed. This significant decrease in buckling capacity is probably a result of the large geometric nonlinearity caused by the cantilever mode shape deflection of the tank, which the LBA could not capture. Thus, the static GNIA using Riks algorithm was conducted for Tanks A and B to better identify the static buckling capacity. An eigen-affine imperfection shape was adopted and the imperfection amplitude was set to $0.01t$. This very small imperfection was introduced because Riks analysis may not able to capture the buckling behavior properly without any imperfection. The buckling capacity obtained from the static GNIA for Tanks A and B are 8819 Pa and 5108 Pa, respectively. Therefore, the results of the static GNIA and dynamic analysis agreed well with each other because both of the analysis took the geometric nonlinearity into account. The difference in buckling capacity between the two analyses was around 15%. This is also the relationship observed between the LBA and the dynamic analysis for broad tanks. Thus, the LBA analysis for taller tanks (Tanks A and B) grossly overestimate the static buckling capacity for not considering geometric nonlinearity due to cantilever mode deflection. GNIA buckling results with a very small imperfection amplitude such as $0.01t$ would be more comparable with the dynamic buckling results.

2.3.4 Effect of Wind Gust

To address the influence of the fluctuation amplitude and the duration of the wind, the parameters were adjusted and analyzed in this section. First, the fluctuation amplitude, P_f, of a wind gust was studied. For this study, a wind gust of 9 seconds was applied to Tank C. The fluctuation amplitude was set to 0.1, 0.2, or 0.3 times of the average pressure. The wind was assumed to be linearly fluctuating at 35.90 Hz, 5.633 Hz, and 3.33 Hz frequencies. The frequency 35.90 Hz was the frequency which had the most effective mass in the windward direction, 5.633 Hz was the first natural vibration frequency, and 3.33 Hz was an arbitrarily picked frequency. The buckling capacity was obtained with incremental wind pressures of 50 Pa. The results are presented in Table 2-7. The buckling capacity decreased only for one case of 3.33 Hz fluctuation frequency when the fluctuation amplitude was modified. Again, it can be observed that a fluctuation in wind load did not trigger the most sensitive mode: the cantilever mode. As a consequence, even when the wind fluctuated at rather large amplitudes, there is not a significant loss in buckling capacity.

The effect of the duration of the wind gust was also investigated. Tank C was again examined and the fluctuation amplitude was set equal to 0.1 times the average pressure. The same set of impulse loading fluctuation frequencies specified in the former paragraph were adopted. In addition, a step load (no fluctuation of wind load) was also included. Analyses with wind gust duration of 9 seconds and 30 seconds were compared. The result of the analysis are given in Table 2-8. No significant difference in buckling capacity is observed when the duration of the wind gust is extended. This implies that if a tank would buckle, it would probably buckle within the first 9 seconds. This indicates that the wind gust duration of 9 seconds was reasonable. Thus, with the discussion on the influence of wind gusts concluded, the effect of the time step is discussed in the next section.

2.3.5 Effect of Time Step

To investigate the effect of the time step, a step load was applied to the tanks in this section. Analyses using Tank E were conducted using the ABAQUS built-in time step and the time step proposed by Tong and Tsui [45]. In the model of Tank E, the element with the smallest dimension had a width of 6.5 cm. While the mesh scaling factor β was set to 1.76, the smallest dimension of mesh was controlled by the elements on the top wind girder. The time step generated by ABAQUS was 9.75×10^{-6} seconds, which implies that the scaling factor α used was 0.740. However, the time step proposed by Tong and Tsui [45] is much smaller as 1.6×10^{-6} seconds (equivalent to $\alpha = 0.121$).

Using these parameters, with both time steps, the buckling capacity λ_{cr} is observed to be 1000 Pa. The displacement response present at the buckling pressure level ($\lambda_{cr} = 1000$ Pa) is given in Figure 2-17. In this figure, the two different nodes which have the largest displacement response are selected, one node for each time step. It is evident that these two nodes are not identical. However, not only are their response time histories similar, but also their buckling capacities matched. This indicates that when different time steps are used, the response of a structure may slightly vary, but the overall behavior and buckling capacity are similar. This may imply that the ABAQUS built-in time step is sufficiently small to make the analysis stable, and there little need for an α value as small as 0.1.

In order to find the maximum time step size which makes the analysis stable, FEA were conducted using time steps larger than the step generated by the ABAQUS built-in time step. Here, maximum acceptable time step size was defined as the maximum at which can successfully complete the analysis with no error messages or terminating the analysis. The maximum acceptable time steps are presented in Table 2-9. Again, the smallest mesh dimension was controlled by the elements on the top wind girder for all five models. The results show that in order to ensure a stable analysis, an α of no greater than 1.0 is preferable. However, for Tanks A and C, an even smaller time step size is needed, indicating that an α less than 0.9 is a better criterion for a time step size when performing explicit dynamic analyses, which is the value suggested by Belytschko et al. [44]. The next section shall focus on a mesh convergence study.

2.3.6   Mesh Convergence Study

To conduct a mesh convergence study, different mesh sizes were determined using the previously mentioned index $\beta\sqrt{Rt}$. Tank D was utilized for this part of the study and the β values selected were 0.29, 0.43, 0.58, and 1.76 (the global mesh sizes were 10 cm, 15 cm, 20 cm, and 60 cm, respectively). The buckling capacities of the models with differing mesh sizes under a constant dynamic load and the static linear buckling capacities are presented in Table 2-10. The dynamic buckling capacities were obtained using a 5 Pa increment. Though $\beta = 0.29$ did give a slightly lower buckling load when compared to $\beta = 0.43$, it could be decided that the linear buckling capacities and the dynamic buckling capacities when $\beta = 0.43$ and 0.58 are close enough to be considered converged solutions. This indicates that a scale factor β of 0.5 should be enough for achieving a fairly precise dynamic or static buckling load. The main reason for using a relatively large mesh size when conducting a dynamic analysis is time consuming relative to a static LBA or even a GNIA, which considers imperfection of geometry in the model. Next, imperfection sensitivity of the dynamic analysis and static GNIA shall be investigated.

2.3.7   Analysis including Geometric Imperfections

Geometric imperfections were introduced in the explicit dynamic analysis and the static GNIA to compare the static and dynamic buckling capacities with geometric imperfections. Tank E was used for this purpose. The first buckling mode shape obtained from the LBA is shown in Figure

2-18 along with the selected imperfection profile. Subfigures (a) and (b) in Figure 2-18 are the top view and elevation view of the mode shape, respectively. The results of the GNIA are presented in Figure 2-19. Compared with the buckling capacities obtained from the LBA, the buckling capacities are overall relatively smaller. Figure 2-19 shows that for tanks with larger imperfection amplitudes (1.0t) there is no particular critical point, a peak of load in GNIA. On the other hand, analyses with smaller imperfection amplitudes had distinct critical points in Figure 2-19. A decrease in peak applied load (buckling capacity) is associated with an increase in the imperfection amplitude.

The same phenomenon is observed in the results of the dynamic analysis. Tank E was subjected to a linear impulse pressure which fluctuated linearly at the first natural vibration frequency of Tank E. The time step adopted in this section was the ABAQUS built-in time step. For the tanks with relatively smaller imperfections (0.1t, 0.25t, and 0.5t) the buckling behavior was distinct and met the Budiansky and Roth [38] buckling criterion stated previously. The buckling capacities λ_{cr} are 850 Pa, 750 Pa, and 600 Pa for 0.1t, 0.25t, and 0.5t imperfection amplitudes, respectively. Note that the buckling capacities were obtained using a 50 Pa increment. The buckling capacities obtained from GNIA are 877 Pa, 775 Pa, and 709 Pa for tanks with imperfections of 0.1t, 0.25t, and 0.5t respectively. For the tanks with imperfections of 0.1t, and 0.25t, the buckling capacities of the static GNIA and the dynamic analysis have a good agreement, though the results for the tanks with imperfection of 0.5t did not match as well. This indicates that a static analysis is sufficient for analyses with small imperfections. On the other hand, the buckling behavior of tanks with large imperfections (0.75t and 1.0t) remain unclear, because there is no distinct critical point at which the system buckles, as mentioned previously. In other words, the magnitudes of the displacement obtained from different levels of pressure do not have a difference within an order of magnitude, and thus the behavior does not meet the dynamic buckling criterion defined in this study.

The displacement response of the tanks with 0.5t, 0.75t and 1.0t of imperfection amplitudes under different pressure levels are presented in Figure 2-20. Similarly, the displacement response of the tanks with different levels of imperfection, but subjected to a particular pressure are plotted in Figure 2-21. Note that for Figure 2-20 and Figure 2-21, only the first 3 seconds of the time histories

are reported because the behaviors after this interval are similar. Though, there seems to be a jump in displacement response of the tanks with imperfection amplitudes of $0.75t$ and $1.0t$ subjected to different pressure levels, the difference is not significant enough to meet the criterion. Since the results obtained from the GNIA and the dynamic analysis are similar, it can be concluded that a GNIA would be adequate for a practical design.

2.4   Conclusion

The natural vibration frequencies of tanks were obtained using a FEA. These frequencies were then used to find a resonant behavior in dynamic analyses. Dynamic analyses of open-top steel tanks with varying geometries under various wind loading patterns were then performed. Furthermore, information needed to perform a precise explicit dynamic analyses, including converged mesh size and time step size were determined.

The natural vibration frequencies was first obtained using the FEA and compared to a theoretical solution [42] and FEA results from other sources [36]. The FEA results closely matched the theoretical results. After comparing the FEA result with the result of the previous study [36], it was determined that for tanks with similar geometries, including diameter, aspect ratio and shell thickness, the first three natural vibration frequencies of the tank shell would also be similar regardless of the roof configurations. The difference between natural vibration frequencies of tank shells with different roof configuration was less than 5%. The effective modal mass for all five tanks were also examined. It was concluded that, the dominant mode for all the tanks were cantilever mode in the windward direction. It was also found that larger the aspect ratio was, the earlier the cantilever mode occurred.

Explicit dynamic analyses were conducted for geometrically perfect tanks with five different height to diameter aspect ratios, 4.0, 2.0, 1.0, 0.4, and 0.2, under different loading patterns. Loads fluctuating at a wide range of frequencies were considered, including the first natural vibration frequency and the frequency associated with the dominant mode of each of the tanks. It was concluded that the behavior of broader tanks (Tanks C, D, and E) and taller tanks (Tanks A and B) were different due to the effect of the cantilever mode.

For broad tanks, a linear (saw-tooth) and sinusoidal impulse in time domain were applied. Although there was a 15% reduction in the buckling capacity compared to that obtained with step loading in time domain and the LBA, no resonance response was observed when the load was fluctuated at various periods.

For taller tanks (Tank A and B), the buckling capacities obtained from the LBA were significantly different from the buckling capacities obtained from the dynamic analyses and the GNIA. This was caused by the geometric nonlinearity which greatly affected the behavior of tall tanks. The LBA did not take geometric nonlinearity into account, but the other two analyses did. Moreover, the buckling of the shell of Tank A did not meet the criterion defined by Budiansky and Roth [38] since the cantilever motion of Tank A was too dominant. Comparing the GNIA buckling capacities with the dynamic buckling capacities on the shell, a decrease of 15% was found. This indicated that the difference in buckling capacities of a tank's shell obtained by conducting a static or dynamic analysis would be around 15% for tanks with aspect ratios between 0.2 and 4.0. This is consistent with what Sosa and Godoy [7] reported. It may be concluded that those open-top steel tanks would not encounter excessive displacement response from resonance, because the wind distribution on the tank was not able to trigger the mode with the highest effective modal mass.

The effect of fluctuation amplitude and wind gust duration was also discussed. Fluctuation amplitudes of 20% and 30% of the average wind pressure level, and a wind gust duration of 30 seconds were examined. These wind gusts, however, were not able to trigger the resonance, and the buckling capacity barely differed when comparing with a wind gust of 9 seconds with a fluctuation amplitude of 10% of the average wind pressure. This implied that wind duration and fluctuation amplitude had little influence on the dynamic behavior of the studied tanks because it did not match the dominant mode of the adopted tanks.

To provide the information that is needed for a precise dynamic analysis, a time step that ensures a stable analysis was proposed and mesh convergence study was also performed. The result of the time step study indicated that the criteria adopted by ABAQUS [43] was sufficient to make an explicit dynamic analysis stable. The results produced by adopting the ABAQUS criteria and a smaller time step did not differ from each other significantly. Regarding suitable mesh size, for an

analysis using a maximum time step, it would be better for the time step size to adhere to the criterion (α less than 0.9) proposed by Belytschko et al. [44]. On the other hand, the results of the mesh convergence study using a LBA indicated that a mesh scaling factor β of 0.5 should be adequate for achieving a precise result for the buckling capacity of an open-top steel tank.

Finally, a static GNIA and a dynamic analysis with imperfections were performed using the eigen-affine imperfection profile obtained from the LBA. It was determined that the buckling behaviors produced by the static GNIA and the dynamic analyses agreed well when the imperfection amplitude is small ($0.1t$ and $0.25t$). For small imperfections ($0.1t$ and $0.25t$), the buckling capacity obtained from the static GNIA and the dynamic analysis were close to each other. However, for tanks with large imperfections ($1.0t$), the buckling behavior could not be well defined for either the static GNIA or the dynamic analysis. For the static GNIA, there was no critical point, while the displacement response of the dynamic analysis for the tanks subjected to different levels of external pressure did not meet the defined buckling criterion. For both the static GNIA and the dynamic analysis, a decrease in buckling capacity was clear regardless of the level of imperfection.

To summarize, the results in this study indicated that empty open-top steel tanks do not face resonance responses under the situation considered. On the other hand, information that is needed for a precise dynamic analysis is presented.

2.5 Tables

Table 2-1. Shell course thickness for modeled tanks.

Tank diameter (m)	Shell thickness of course (mm)				
	1 (bottom)	2	3	4	5 (top)
3.05	6.35	4.76	4.76	4.76	4.76
6.10	6.35	4.76	4.76	4.76	4.76
12.2	6.35	4.76	4.76	4.76	4.76
30.5	12.7	9.50	7.90	7.90	7.90
62.0	22.1	16.7	12.4	8.00	7.90

Table 2-2. Size of top wind girder for modeled tanks.

Tank diameter(m)	Detail type	Size (mm)	Distance from top edge of shell (cm)	Section Modulus (cm³)
3.05	a	L65x65x8	N/A	8.46
6.10	b	L65×65×6	2.50	27.03
12.2	c	L150×75×10	7.61	308.2
30.5	e	b = 400	12.6	687.0
61.0	e	b = 1040	12.6	2700

Table 2-3. Geometry of tanks used in Ref. [24].

	Tank Diameter (m)	Height (m)	H/D	Shell thickness (mm)	Boundary condition
Case1	20	18.4	0.92	8	Fixed
Case2					Free
Case3	40	16.9	0.42	16	Fixed
Case4					Free

Table 2-4. Comparison of FEA results and Ref. [24] results

	First natural vibration frequency (Hz)		Wave number on the shell		Static buckling capacity (Pa)		Dynamic buckling capacity (Pa)	
	FEA	Ref. [24]	FEA	Ref. [24]	FEA	Ref. [24]	FEA	Ref. [24]
Case1	4.42	4.43	12	12	3334	3623	3456	3442
Case2	1.79	1.79	8	8	1504	1547	1600	1625
Case3	4.65	4.64	17	17	6765	7420	7680	7642
Case4	1.95	1.95	12	12	2972	3268	3200	3333

Table 2-5. Natural vibration frequencies obtained by FEA and comparison with theoretical solution [42]

	Tank A	Tank B	Tank C	Tank D	Tank E
Diameter	3.05 m	6.10 m	12.2 m	30.5 m	62.0 m
	Natural vibration frequency (Hz)				
Mode	FEA (wave number)				
1st	10.821 (4)	8.109 (7)	5.753 (11)	4.924 (19)	4.225 (28)
2nd	13.373 (5)	8.213 (6)	5.919 (10)	4.926 (18)	4.229 (27)
3rd	13.526 (3)	9.176 (8)	5.932 (12)	5.013 (20)	4.248 (29)
Mode	Theoretical solution (wave number) [42]				
1st	11.055 (4)	8.270 (7)	5.730 (11)	4.838 (18)	4.075 (27)
2nd	13.711 (3)	8.302 (6)	5.896 (10)	4.856 (19)	4.088 (28)
3rd	13.794 (5)	9.425 (8)	5.911 (12)	4.921 (17)	4.096 (26)

Table 2-6. Natural vibration frequencies obtained by FEA of Tank D and the comparison with FEA results obtained by Virella et al. [36] using tanks with various roof configuration.

	This study	Virella et al. [36]			
	Open-top	Tank with roof rafters		Tanks with self-supported roofs	
Mode		Cone	Shallow Cone	Dome	Cone
1st	5.029	5.051	5.000	4.785	4.762
2nd	5.036	5.076	5.051	4.808	4.831
3rd	5.203	5.102	5.181	4.831	N/A

Table 2-7. Buckling capacities (Pa) of Tank C subjected to wind gust with different fluctuation amplitudes.

	Frequency of external load		
P_f/P_{ave}	3.33 Hz	5.63 Hz	35.9 Hz
10%	1500	1650	1550
20%	1500	1650	1550
30%	1450	1650	1550

Table 2-8. Buckling capacities (Pa) of Tank C subjected to 9 seconds and 30 seconds durations of wind gusts.

Wind gust duration (sec)	Frequency of external load			
	3.33 Hz	5.63 Hz	35.9 Hz	No fluctuation
9 sec	1500	1650	1550	1650
30 sec	1500	1650	1550	1650

Table 2-9. Time step parameter α values of the ABAQUS [43] generated time step sizes and maximum acceptable time step sizes.

Tank diameter (m)	Smallest dimension of the mesh (mm)	Time step of $\alpha=1$	ABAQUS generated time step		Maximum acceptable time step	
			Size	α value	Size	α value
3.05	32.5	6.59E-6	5.33E-6	0.81	6.00E-6	0.91
6.10	25.0	5.07E-6	4.25E-6	0.84	5.10E-6	1.01
12.2	37.5	7.60E-6	6.64E-06	0.87	7.00E-6	0.92
30.5	65.0	1.32E-5	9.85E-06	0.75	1.40E-5	1.06
62.0	65.0	1.32E-5	9.85E-06	0.74	1.40E-5	1.06

Table 2-10. Global mesh sizes used in the mesh convergence study and the corresponding buckling capacities.

Mesh scaling factor β	Global mesh size (cm)	Dynamic buckling capacity (Pa)	Linear buckling capacity (Pa)
0.29	10	1455	1460
0.43	15	1460	1465
0.58	20	1460	1473
1.76	60	1650	1624

2.6 Figures
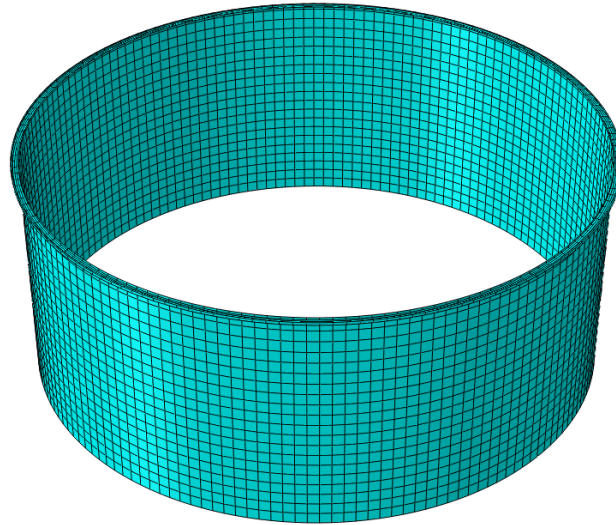
Figure 2-1. Finite element model of Tank D with 4491 S4R elements (mesh scaling factor $\beta = 1.76$).
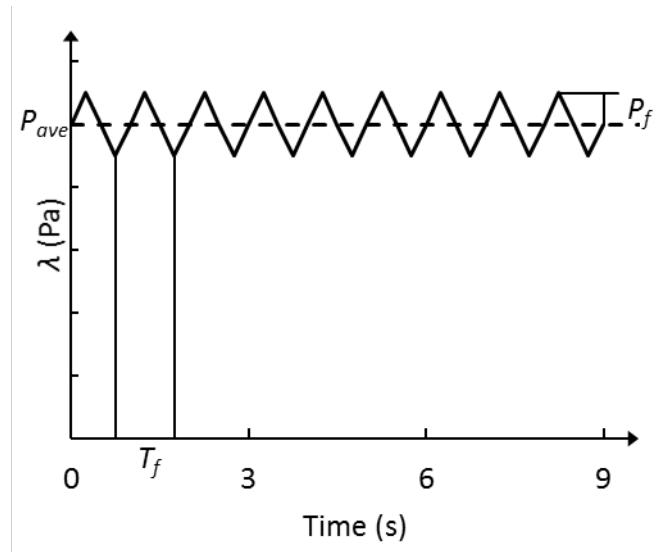
Figure 2-2. Example time history of linear impulse pressure. $T_f = 1$ second this diagram. $P_f = 0.1 P_{ave}$.
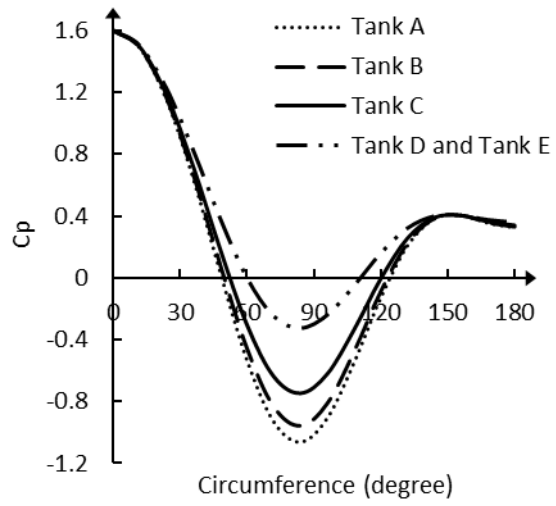
Figure 2-3. The wind pressure distribution specified for open-top tanks specified in Eurocode [52].

(a)

(b)
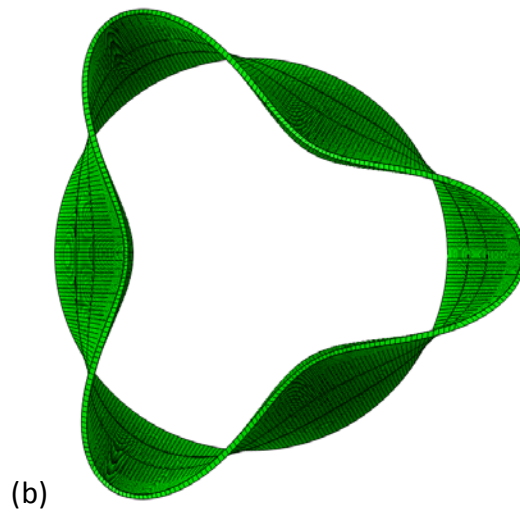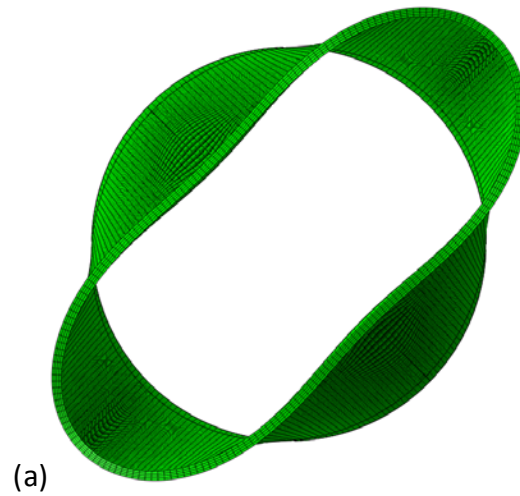
Figure 2-4. Top view of first eigen mode shape of (a) Tank A and (b) Tank B.
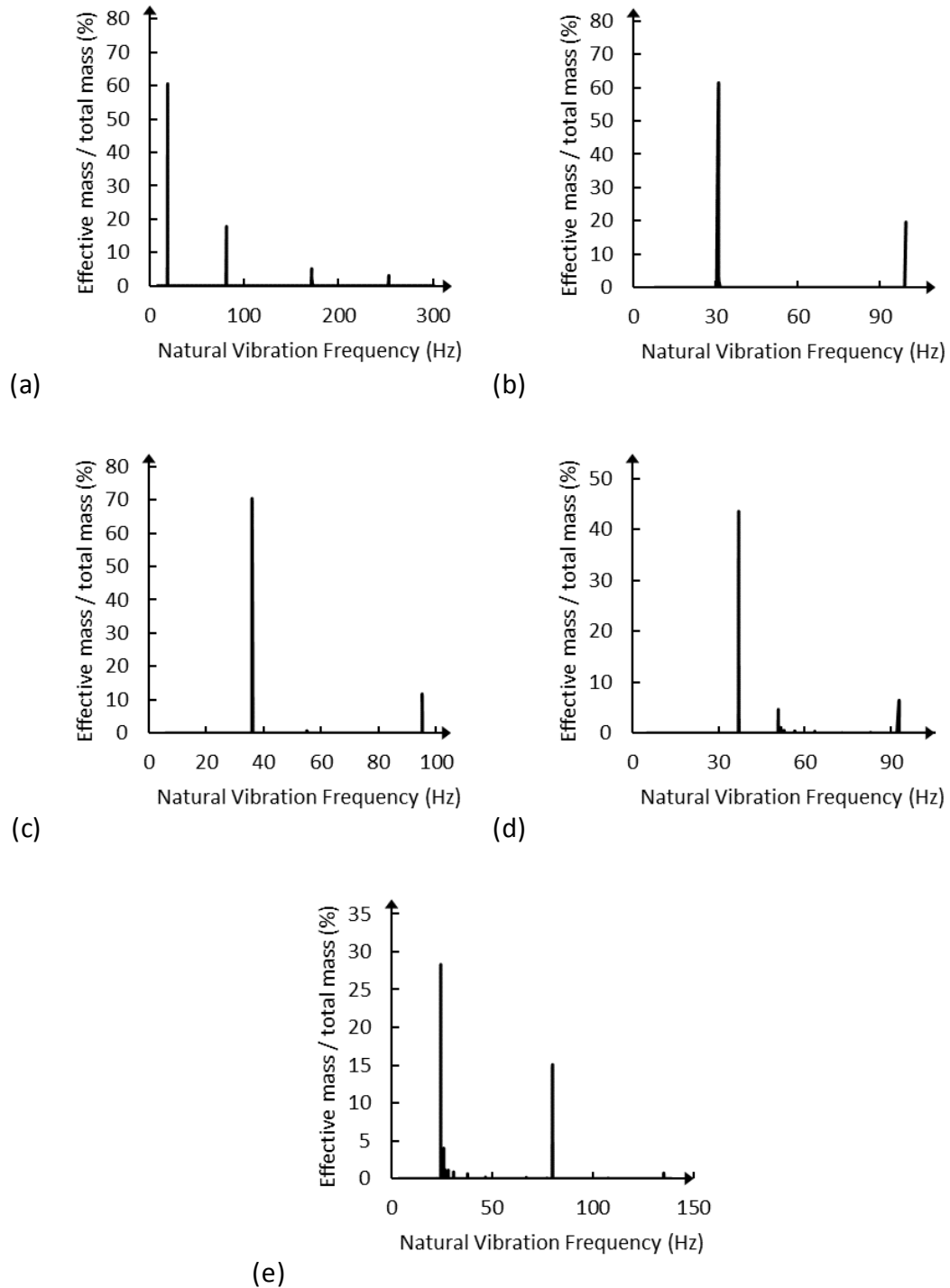
Figure 2-5. Ratio of the effective mass to the total mass for each mode with respect to the eigen-frequency. (a) Tank A, (b) Tank B, (c) Tank C, (d) Tank D, (e) Tank E.
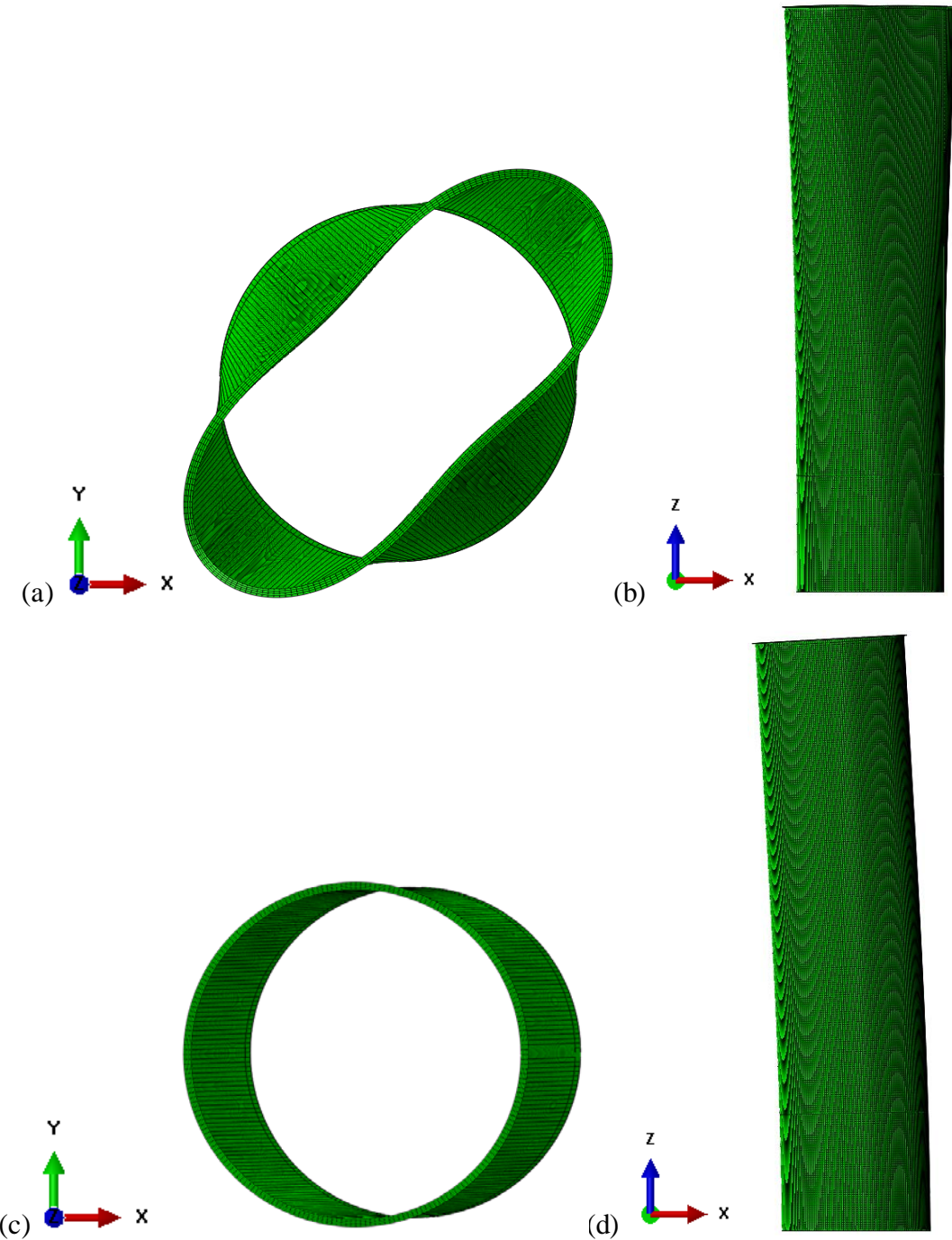
Figure 2-6. Top and elevation view of the eigen mode shape for the first mode and the mode with most effective mass of Tank A in the windward direction (+x to -x). (a) and (b) are the top view and elevation view of the first mode, (c) and (d) are the top view and elevation view of the dominant mode
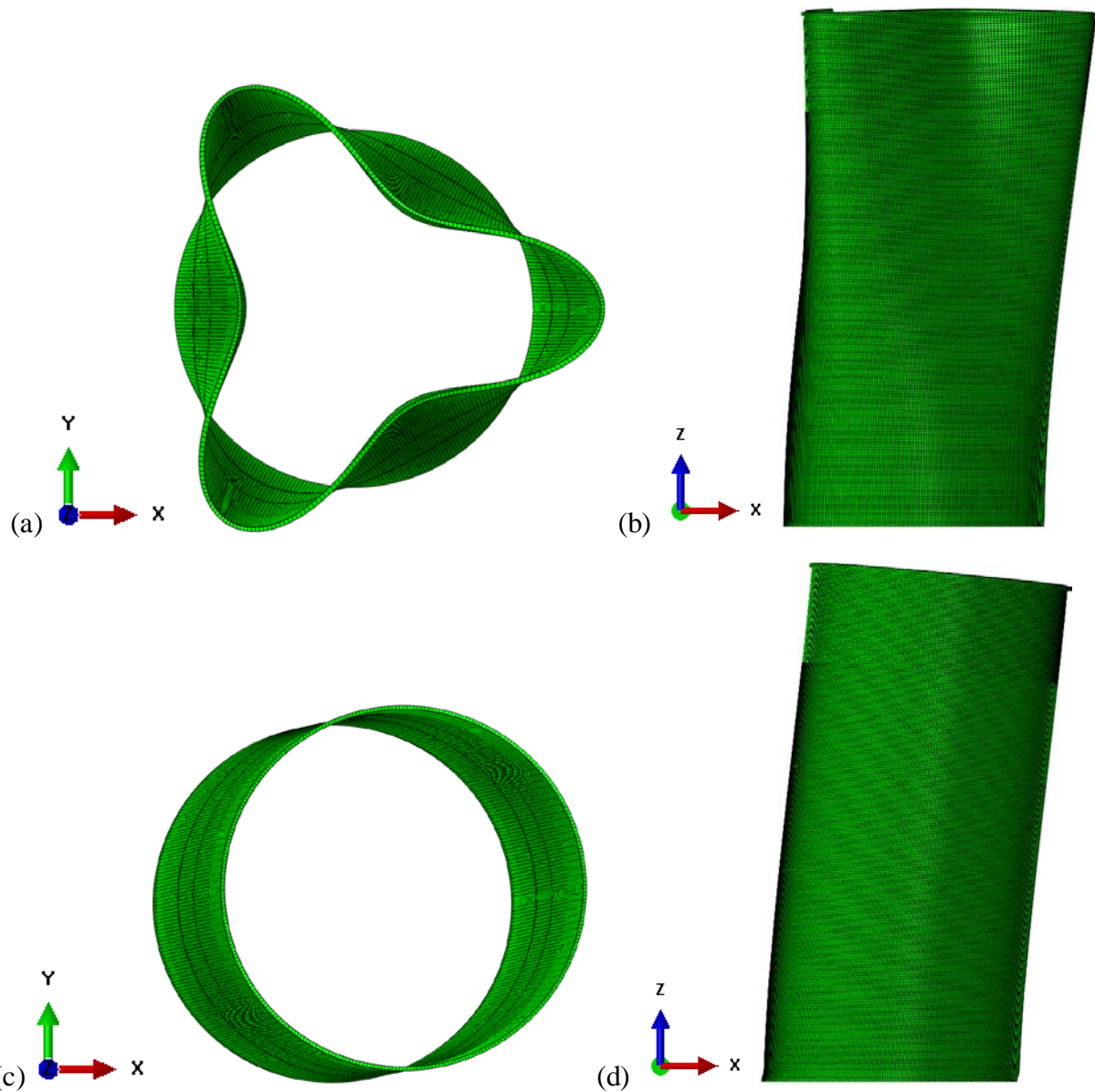
Figure 2-7. Top and elevation view of the eigen mode shape for the first mode and the mode with most effective mass of Tank B in the windward direction (+x to -x). (a) and (b) are the top view and elevation view of the first mode, (c) and (d) are the top view and elevation view of the dominant mode
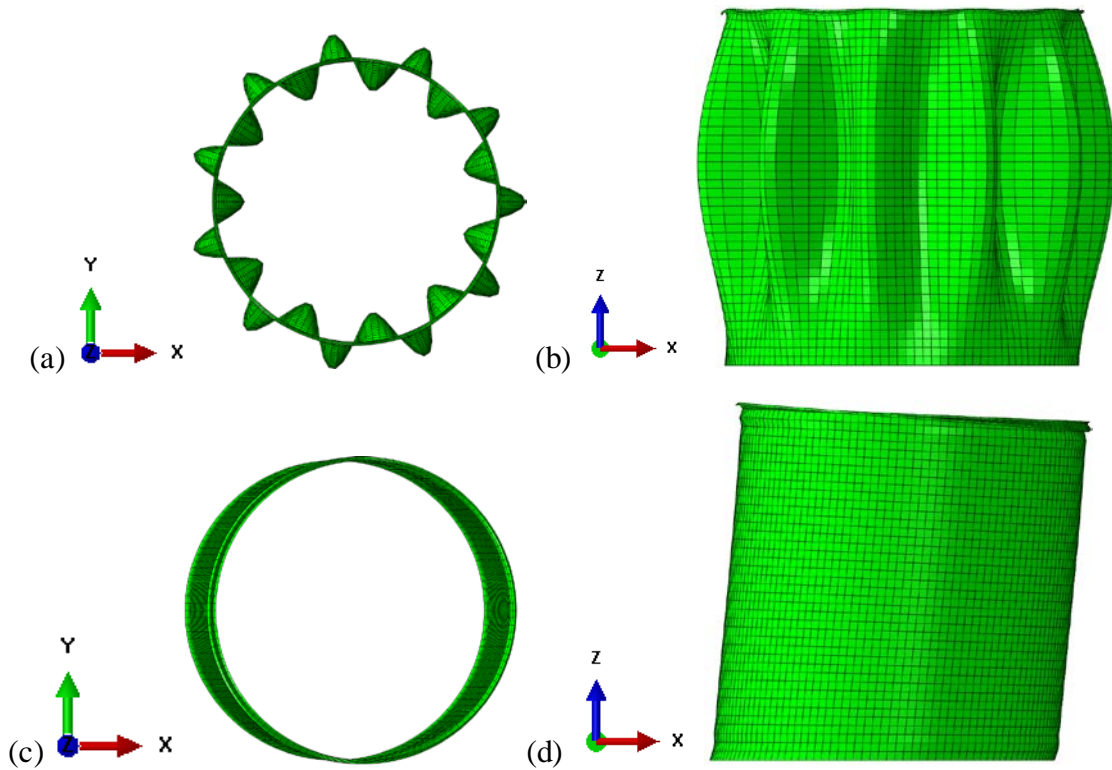
Figure 2-8. Top and elevation view of the eigen mode shape for the first mode and the mode with most effective mass of Tank C in the windward direction (+x to -x). (a) and (b) are the top view and elevation view of the first mode, (c) and (d) are the top view and elevation view of the dominant mode
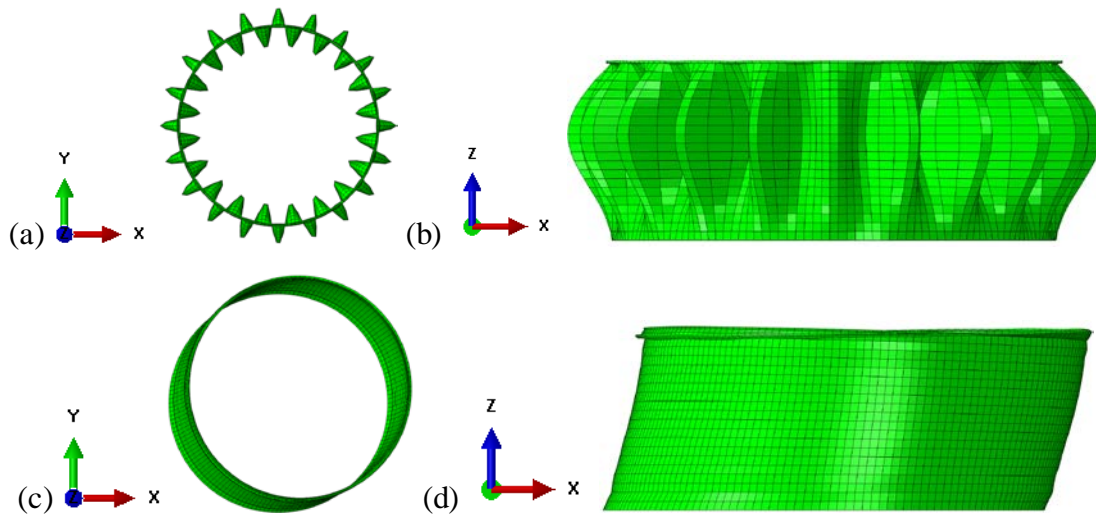
Figure 2-9. Top and elevation view of the eigen mode shape for the first mode and the mode with most effective mass of Tank D in the windward direction (+x to -x). (a) and (b) are the top view and elevation view of the first mode, (c) and (d) are the top view and elevation view of the dominant mode
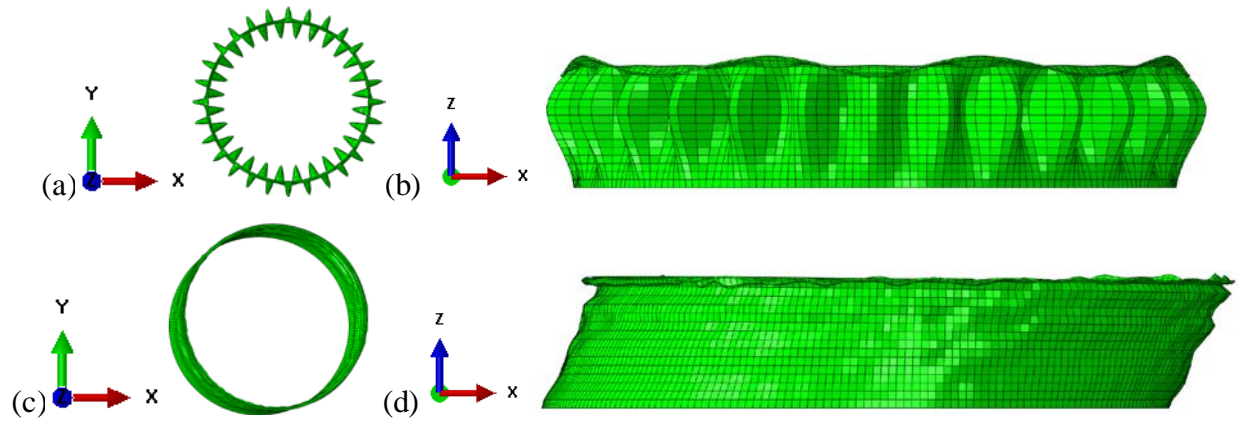
Figure 2-10. Top and elevation view of the eigen mode shape for the first mode and the mode with most effective mass of Tank E in the windward direction (+x to -x). (a) and (b) are the top view and elevation view of the first mode, (c) and (d) are the top view and elevation view of the dominant mode

(a)

(b)
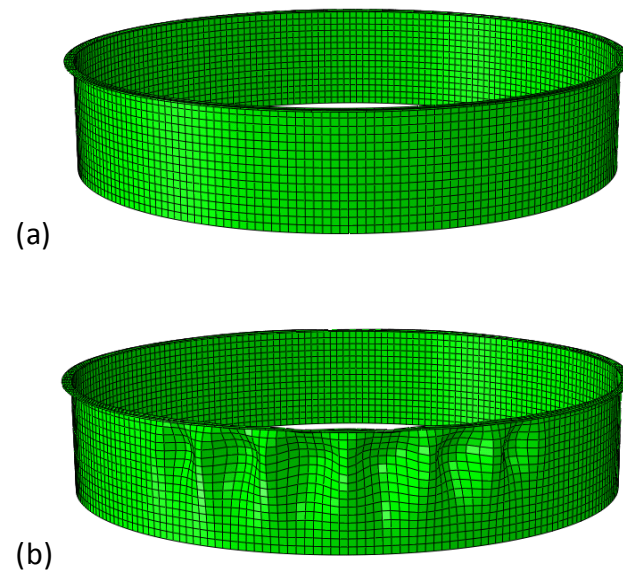
Figure 2-11. Deformed shape of Tank E under different step loadings. (The displacement is scaled by 20 times in both figures.) (a) $\lambda = 980$ Pa, (b) $\lambda = 1000$ Pa
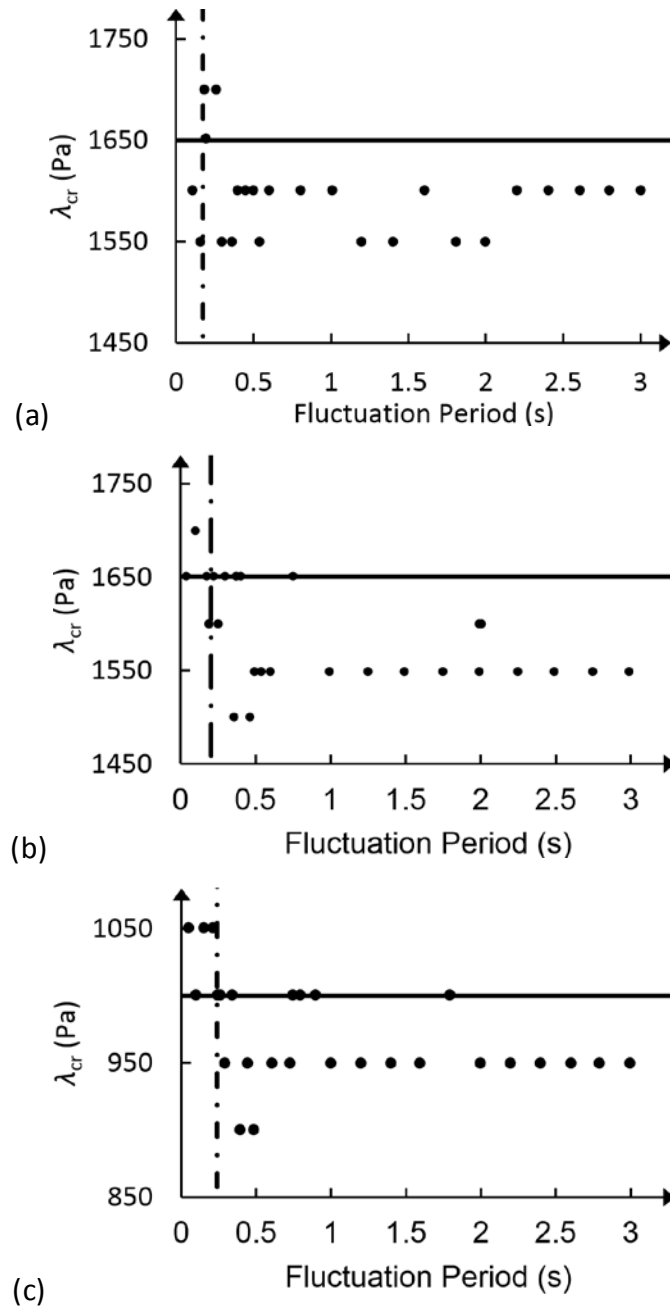
Figure 2-12. The dynamic buckling capacities of (a) Tank C, (b) Tank D, and (c) Tank E with a linear impulse applied at various fluctuation periods. The solid line represents the loading without fluctuation in the time domain, and the vertical dotted line represents the first natural vibration period.
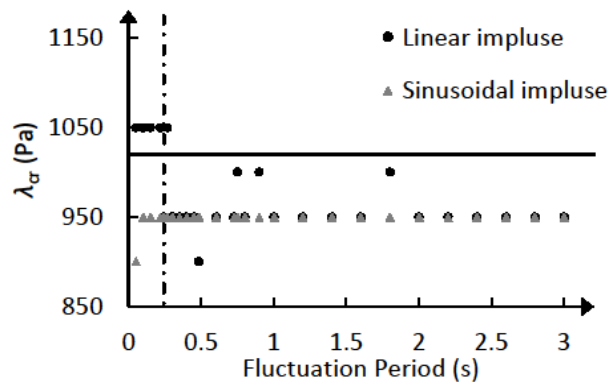
Figure 2-13. The dynamic buckling capacities Tank E with a linear and a sinusoidal impulse applied at various fluctuation periods. The solid line represents the loading without fluctuation in time domain, and the vertical dotted line represents the first natural vibration period.
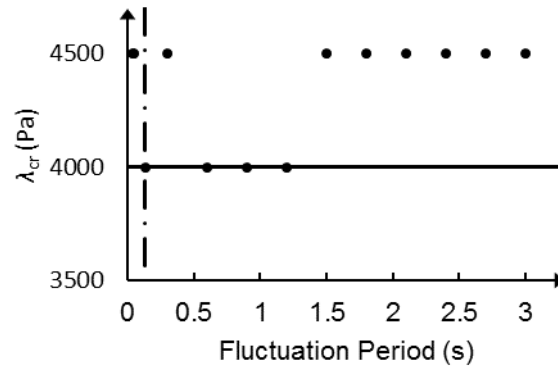
Figure 2-14. The dynamic buckling capacities of Tank B with a linear impulse applied at various fluctuation periods. The solid line represents the loading without fluctuation in the time domain, and the vertical dotted line represents the first natural vibration period.
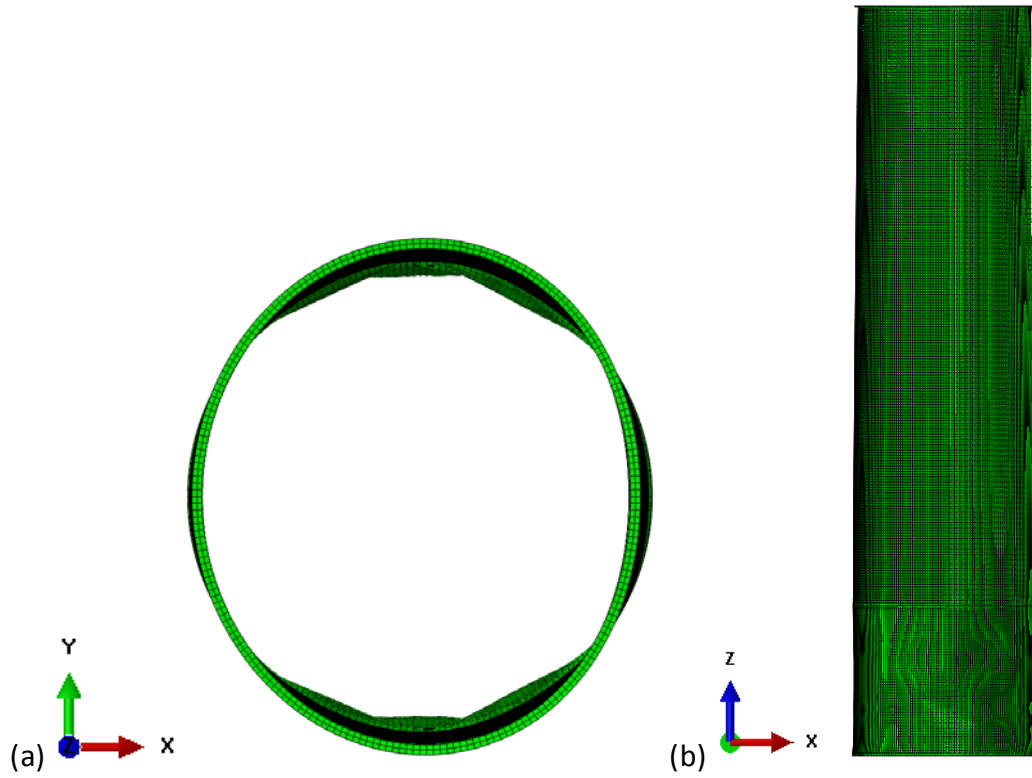
Figure 2-15. Deformed shape of Tank A under wind loading fluctuating at its first natural vibration frequency, λ = 7000 Pa. (a) Top view, (b) Elevation view. (Wind blowing from +x to -x)
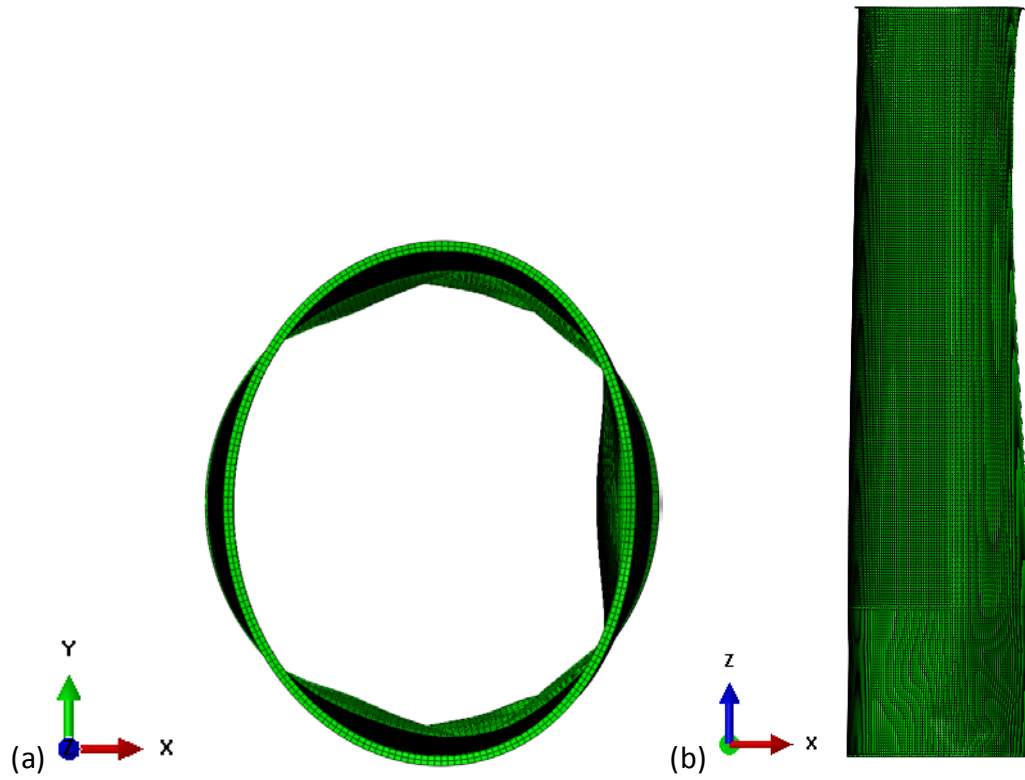
Figure 2-16. Deformed shape of Tank A under wind loading fluctuating at its first natural vibration frequency, $\lambda = 8000$ Pa. (a) Top view, (b) Elevation view. (Wind blowing from +x to -x)
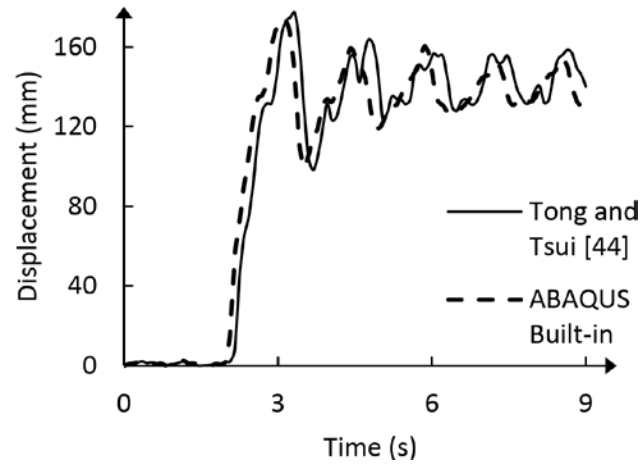
Figure 2-17. Displacement response of Tank E under constant external pressure in the time domain obtained using a different time step size. $\lambda = 1000$ Pa.
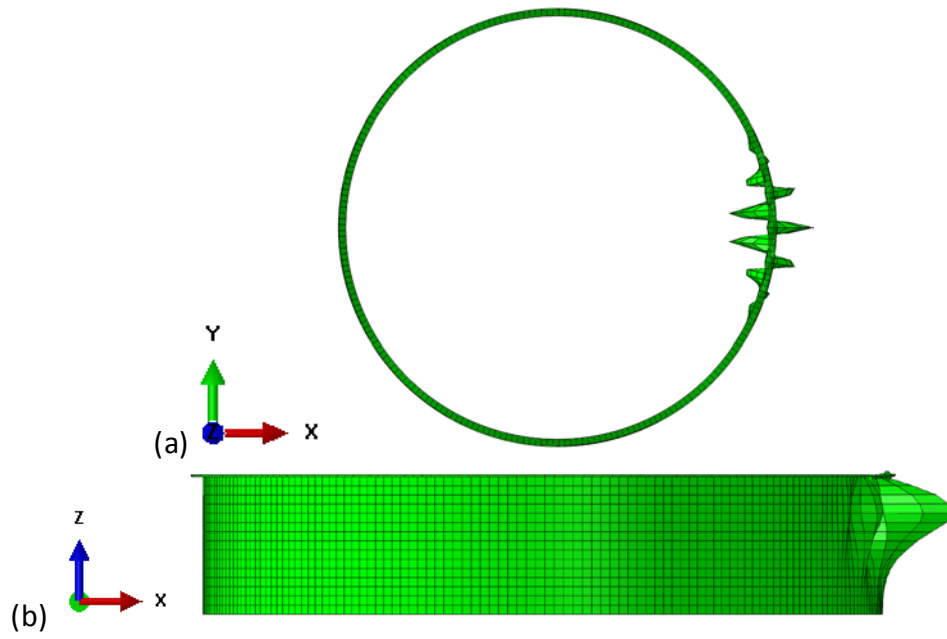
Figure 2-18. Top view and elevation view of first LBA mode shape of Tank E. (wind blowing from +x to -x)
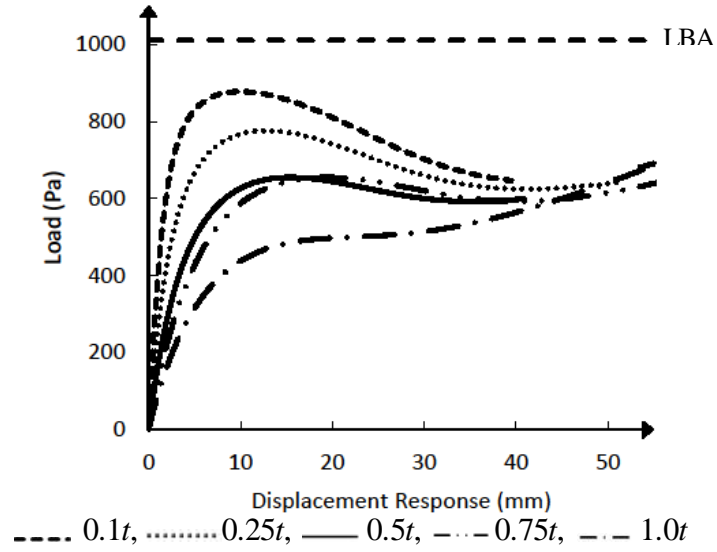
Figure 2-19. GNIA results for Tank E subjected to different levels of imperfection amplitudes.
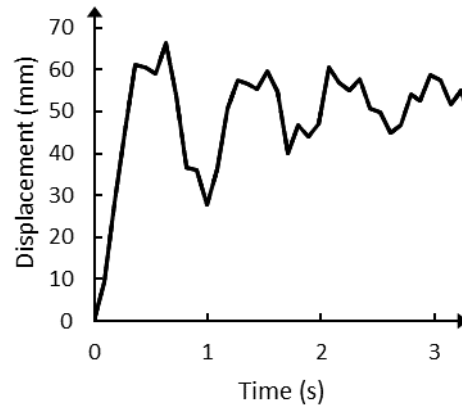
(a)
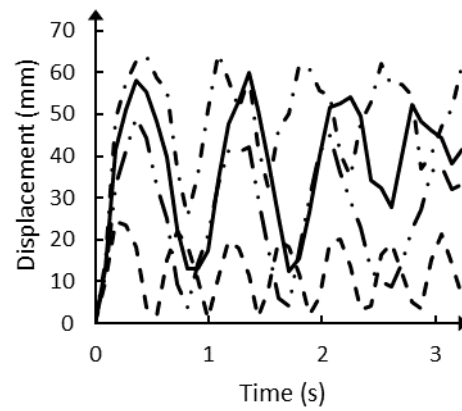
(b)
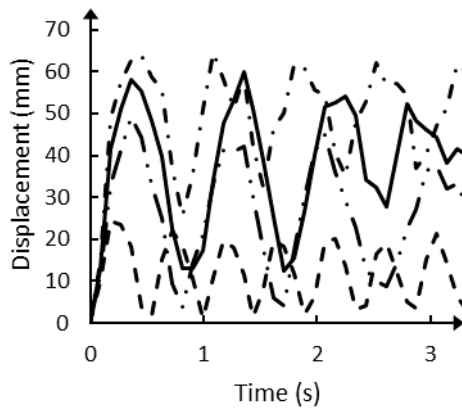
(c)

- - - 500 Pa, — ·· — 550 Pa, —— 600 Pa, — · — 650 Pa

Figure 2-20. Dynamic analysis of tanks with certain imperfection amplitudes subjected to different pressure levels. (a) 0.5*t* (b) 0.75*t* (c) 1.0*t*
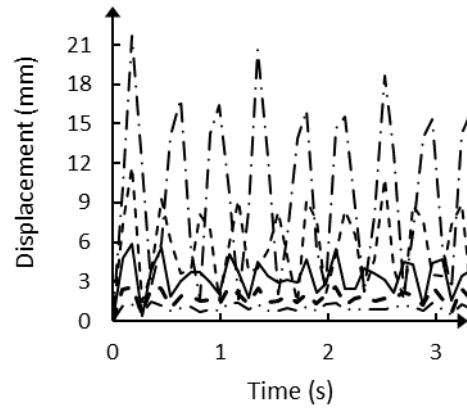
(a)
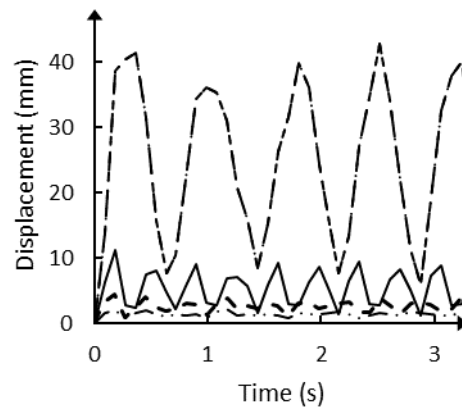
(b)
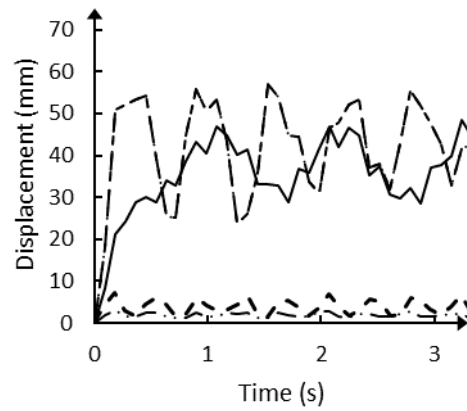
(c)

—··—0.1t, ▬▬▬0.25t, ——— 0.5t, ---- 0.75t, —·— 1.0t

Figure 2-21. Dynamic analysis with imperfections under different pressure levels. (a) 400 Pa (b) 500 Pa (c) 600 Pa.

2.7   References

[1]   A. Zingoni, "Liquid-containment shells of revolution: a review of recent studies on strength, stability and dynamics," *Thin-Walled Structures,* vol. 87, pp. 102-114, 2015.

[2]   L. A. Godoy, "Buckling of vertical oil storage steel tanks: Review of static buckling studies," *Thin-Walled Structures,* vol. 103, Thin-Walled Structures, pp. 1-21, 2016.

[3]   E. Azzuni and S. Guzey, "Stability of open top cylindrical steel storage tanks: Design of top wind girder," *Journal of Pressure Vessel Technology,* vol. 139, no. 3, p. 031207, 2017.

[4]   API, *Welded Tanks for Oil Storage*. Washington, DC   API Standard No.650, 2013.

[5]   L. Zick and R. McGrath, "Design of Large Diameter Cylindrical Shells," *Proceedings—API Division of Refining, Americadn Petroleum Institute, New York,* vol. 48, pp. 1114-1140, 1968.

[6]   E. Azzuni and S. Guzey, "Comparison of the shell design methods for cylindrical liquid storage tanks," *Engineering Structures,* vol. 101, pp. 621-630, 2015.

[7]   E. M. Sosa and L. A. Godoy, "Nonlinear dynamics of above-ground thin-walled tanks under fluctuating pressures," *Journal of sound and vibration,* vol. 283, no. 1-2, pp. 201-215, 2005.

[8]   Z. Ozdemir, M. Souli, and Y. Fahjan, "Application of nonlinear fluid–structure interaction methods to seismic analysis of anchored and unanchored tanks," *Engineering Structures,* vol. 32, no. 2, pp. 409-423, 2010.

[9]   M. Djermane, D. Zaoui, B. Labbaci, and F. Hammadi, "Dynamic buckling of steel tanks under seismic excitation: Numerical evaluation of code provisions," *Engineering Structures,* vol. 70, pp. 181-196, 2014.

[10]   M. E. Kalogerakou, C. A. Maniatakis, C. C. Spyrakos, and P. N. Psarropoulos, "Seismic response of liquid-containing tanks with emphasis on the hydrodynamic response and near-fault phenomena," *Engineering Structures,* vol. 153, pp. 383-403, 2017.

[11]   M. A. Haroun and G. W. Housner, "Seismic design of liquid storage tanks," *Journal of the Technical Councils of ASCE,* vol. 107, no. 1, pp. 191-207, 1981.

[12]   K. K. Mandal and D. Maity, "Nonlinear finite element analysis of elastic water storage tanks," *Engineering Structures,* vol. 99, pp. 666-676, 2015.

[13]   A. Veletsos, "Seismic response and design of liquid storage tanks," *Guidelines for the seismic design of oil and gas pipeline systems,* pp. 255-370, 1984.

[14]   G. W. Housner, "Dynamic pressures on accelerated fluid containers," *Bulletin of the seismological society of America,* vol. 47, no. 1, pp. 15-35, 1957.

[15]   P. K. Malhotra, "Seismic response of soil-supported unanchored liquid-storage tanks," *Journal of Structural Engineering,* vol. 123, no. 4, pp. 440-450, 1997.

[16]   L. S. Jacobsen, "Impulsive hydrodynamics of fluid inside a cylindrical tank and of fluid surrounding a cylindrical pier," *Bulletin of the Seismological Society of America,* vol. 39, no. 3, pp. 189-204, 1949.

[17]   N. Buratti and M. Tavano, "Dynamic buckling and seismic fragility of anchored steel tanks by the added mass method," *Earthquake Engineering & Structural Dynamics,* vol. 43, no. 1, pp. 1-21, 2014.

[18]   AWWA, *Standard Specifications for Elevated Steel Water Tanks, Standpipes and Reservoirs.* Denver, CO: American Water Work Association, 1935, pp. 1606-1625.

[19]   J. H. Adams, "A study of wind girder requirements for large API 650 floating roof tanks.," in *API, Refining 40th Midyear Meeting,.* Chicago, IL: American Petroleum Institute, 1975, ch. 16-75, pp. 16-75.

[20]   T. Sun, E. Azzuni, and S. Guzey, "Stability of Open-Topped Storage Tanks With Top Stiffener and One Intermediate Stiffener Subject to Wind Loading," *Journal of Pressure Vessel Technology,* vol. 140, no. 1, p. 011204, 2018.

[21]   F. Resinger and R. Greiner, "Buckling of wind loaded cylindrical shells—application to unstiffened and ring-stiffened tanks," in *Buckling of shells*: Springer, 1982, pp. 305-331.

[22]   F. Bu and C. Qian, "On the rational design of the top wind girder of large storage tanks," *Thin-Walled Structures,* vol. 99, pp. 91-96, 2016.

[23]   F. Bu and C. Qian, "A rational design approach of intermediate wind girders on large storage tanks," *Thin-Walled Structures,* vol. 92, pp. 76-81, 2015.

[24]   Y. Uematsu, T. Yamaguchi, and J. Yasunaga, "Effects of wind girders on the buckling of open-topped storage tanks under quasi-static wind loading," *Thin-Walled Structures,* vol. 124, pp. 1-12, 2018.

[25]   I. Sabransky and W. Melbourne, "Design pressure distribution on circular silos with conical roofs," *Journal of Wind Engineering and Industrial Aerodynamics,* vol. 26, no. 1, pp. 65-84, 1987.

[26]   P. Macdonald, K. Kwok, and J. Holmes, "Wind loads on circular storage bins, silos and tanks: I. Point pressure measurements on isolated structures," *Journal of Wind Engineering and Industrial Aerodynamics,* vol. 31, no. 2-3, pp. 165-187, 1988.

[27]   G. Portela and L. A. Godoy, "Wind pressures and buckling of cylindrical steel tanks with a dome roof," *Journal of Constructional Steel Research,* vol. 61, no. 6, pp. 808-824, 2005.

[28]   G. Portela and L. A. Godoy, "Wind pressures and buckling of cylindrical steel tanks with a conical roof," *Journal of Constructional Steel Research,* vol. 61, no. 6, pp. 786-807, 2005.

[29]   Y. Uematsu, C. Koo, and K. Kondo, "Wind loads on open-topped oil storage tanks," in *BBAA VI 6th International Colloquium on Bluff Bodies Aerodynamics and Applications, Milano, Italy. July*, 2008: Citeseer, pp. 20-24.

[30]   R. Greiner and P. Derler, "Effect of imperfections on wind-loaded cylindrical shells," *Thin-Walled Structures,* vol. 23, no. 1-4, pp. 271-281, 1995.

[31]   Y. Uematsu, C. Koo, and J. Yasunaga, "Design wind force coefficients for open-topped oil storage tanks focusing on the wind-induced buckling," *Journal of Wind Engineering and Industrial Aerodynamics,* vol. 130, pp. 16-29, 2014.

[32]   Y. Uematsu and K. Uchiyama, "Deflection and buckling behavior of thin, circular cylindrical shells under wind loads," *Journal of Wind Engineering and Industrial Aerodynamics,* vol. 18, no. 3, pp. 245-261, 1985.

[33]   N. Alujević, N. Campillo-Davo, P. Kindt, W. Desmet, B. Pluymers, and S. Vercammen, "Analytical solution for free vibrations of rotating cylindrical shells having free boundary conditions," *Engineering structures,* vol. 132, pp. 152-171, 2017.

[34]   W. Zhang, Z. Fang, X.-D. Yang, and F. Liang, "A series solution for free vibration of moderately thick cylindrical shell with general boundary conditions," *Engineering Structures,* vol. 165, pp. 422-440, 2018.

[35]   I. Nachtigall, N. Gebbeken, and J. L. Urrutia-Galicia, "On the analysis of vertical circular cylindrical tanks under earthquake excitation at its base," *Engineering structures,* vol. 25, no. 2, pp. 201-213, 2003.

[36]   J. Virella, L. A. Godoy, and L. Suárez, "Influence of the roof on the natural periods of empty steel tanks," *Engineering Structures,* vol. 25, no. 7, pp. 877-887, 2003.

[37]   F. G. Flores and L. A. Godoy, "Forced vibrations of silos leading to buckling," *Journal of Sound and Vibration,* vol. 224, no. 3, pp. 431-454, 1999.

[38]   B. Budiansky and R. S. Roth, "Axisymmetric dynamic buckling of clamped shallow spherical shells," in *NASA Collected Papers on Stability of Shell Structure*, 1962, pp. 597-606.

[39]   American Society of Civil Engineers, *ASCE-7-16: Minimum Design Loads for Building and other Structures*. Reston, VA.: ASCE-7-16, 2016.

[40]   Y. Uematsu, J. Yasunaga, and C. Koo, "Design wind loads for open-topped storage tanks in various arrangements," *Journal of Wind Engineering and Industrial Aerodynamics,* vol. 138, pp. 77-86, 2015.

[41]   J. Yasunaga, "Design Wind Loads on Open-Topped Oil Storage Tanks in Various Arrangements," Master's, Tohoku University, Japan, 2013.

[42]   R. Blevins, *Formulas for natural frequency and mode shape*. New York, NY: Van Nostrand Reinhold Inc., 1979.

[43]   ABAQUS, *ABAQUS Analysis User's Manual version 2018*. Providence, RI: Dassault Systèmes SIMULIA, 2018.

[44]   T. Belytschko, R. Chiapetta, and H. Bartel, "Efficient large scale non-linear transient analysis by finite elements," *International Journal for Numerical Methods in Engineering,* vol. 10, no. 3, pp. 579-596, 1976.

[45]   P. Tong and T. Tsui, "Stability of transient solution of moderately thick plate by finite-difference method," *AIAA journal,* vol. 9, no. 10, pp. 2062-2063, 1971.

[46]   K.-J. Bathe, *Finite element procedures*, 2nd ed. Upper Saddle River, NJ: Pearson Prentice Hall, 2006.

[47]   E. M. Sosa, "Computational buckling analysis of cylindrical thin-walled aboveground tanks," Ph.D. Dissertation, University of Puerto Rico, Mayaguez, Puerto Rico, 2006.

[48]   S. P. Timoshenko and J. M. Gere, "Theory of elastic stability," 2nd ed: McGraw-Hill, New York, 1961.

[49]   A. K. Chopra, *Dyanimcs of Structures: Theory and Application to Earthquake Engineering*, 3rd ed. Upper Saddle River, NJ: Pearson Prentice Hall, 2007.

[50]   R. Han and J. Liu, "Free vibration analysis of a fluid-loaded variable thickness cylindrical tank," *Journal of Sound and Vibration,* vol. 176, no. 2, pp. 235-253, 1994.

[51]   American Society of Civil Engineers, *ASCE -7-10: Minimum Design Loads for Building and other Structures*. Reston, VA.: ASCE -7-10, 2010.

[52]   European Committee for Standardisation, *Eurocode 3: Design of Steel Structures, Part 4.1: Silos*. Brussels, Belgium: Standard No. EN 1993-4-1, 2007.

[53]   J. Yasunaga and Y. Uematsu, "Dynamic Buckling of Cylindrical Storage Tanks under Fluctuating Wind Forces," (in Japanese), *Journal of Wind Engineering,* vol. 43, no. 2, 2018.

[54]   A. Rawat, M. Vasant, and A. K. Nagpal, "Finite Element Analysis of Thin Circular Cylindrical Shells," *Proceedings of the Indian National Science Academy,* vol. 82, no. 2, 2016.

[55]   C. J. Virella, "Buckling of steel tanks subject to earthquake loadings," Ph.D. Dissertation, University of Puerto Rico, Mayaguez, Puerto Rico, 2003.

[56]   L. A. Godoy and F. G. Flores, "Imperfection sensitivity to elastic buckling of wind loaded open cylindrical tanks," *Structural Engineering and Mechanics,* vol. 13, no. 5, pp. 533-542, 2002.

[57]   J. J. Wijker, *Spacecraft structures*, 1 ed. Berlin, Germany: Springer-Verlag, 2008.

3. INFLUENCE OF INTERNAL INWARD PRESSURE ON STABILITY OF OPEN-TOP ABOVEGROUND STEEL TANKS SUBJECTED TO WIND LOADING

Summary

The results of wind tunnel tests indicate that there is an internal inward pressure induced by wind excitation when open-top tanks are examined, but not when close-top tanks are examined. This internal pressure is considered in many design documents outside of the U.S., however, ASCE-7 and API 650 do not explicitly address this factor. The present study examined the effect of this internal pressure by conducting finite element analyses. Open-top tanks with height to diameter ratios of 0.11, 0.2, 0.5, 1.0, 2.0, and 4.0 were modeled using a finite element program. A linear bifurcation analysis and a postbuckling analysis were then conducted to verify the tank's stability when subjected to wind loading in accordance with the wind profiles specified in the selected design documents. To ensure the quality of the analyses, a study on mesh convergence and the load increment of Riks analysis was conducted. It was determined that the presence of the additional internal pressure term has a drastic impact on the buckling capacity of all the tanks examined. As a consequence, it can be concluded that the additional internal pressure generated by the wind on an open-top tank should not be neglected.

3.1 Introduction

Aboveground steel tanks are widely used in various industries to store different types of liquids [1, 2]. To make these tanks cost-efficient, the tanks are usually composed of several courses of steel sheets which vary in thickness from the bottom to the top of the tank. The reason for varying the shell thickness is a result of the hydrostatic pressure created by the stored liquid. The hydrostatic pressure increases as the depth of the liquid increases. Research efforts have been dedicated to properly designing the shell thickness to prevent overstress in the shells, and avoid overly conservative thicknesses [3-5]. Many researchers have been proposing feasible tank configurations for the convince of purchasers [6, 7]. This results in slender geometries with ratios of shell thickness to tank radius as small as 1/2000 [8].

With these relatively thin geometries, tanks are capable of withstanding the pressure resulting from the contained liquid, but are prone to instability when excited by such events as internal vacuum, earthquakes, and wind gusts. An internal vacuum is usually the consequence of an operational mistake [1]. The buckling for such a condition can be modeled as a circumferentially uniform pressure and has been the focus of much researches [9-15]. When a tank is full of liquid, the buckling caused by seismic excitation plays an important role. Similarly, this issue has been widely investigated [16-27]. Other factors including uneven settlement [28] and fire damage [29] may also cause tanks to buckle.

When a tank is empty, however, the damage caused by wind excitation dominates. To thoroughly understand how wind affect empty tanks, boundary layer wind tunnel physical tests (BLWT) have been conducted to determine the relationship between tank geometry and wind pressure distribution. The work presented by Sabransky and Melbourne [30] and MacDonald et al. [31] are known to be the early wind tunnel tests that were conducted using high Reynolds numbers. Sabransky and Melbourne [30] performed tests on isolated silos and an in-line group of silos with conical roofs. Those tanks had aspect ratios (H/D) ranging from 0.66 to 1.16, where H is the height of the tank, and D is the diameter of the tank. This work was stated to be the first valid work in this field [31]. On the other hand, MacDonald et al. [31] conducted wind tunnel experiments on silos with aspect ratios of 0.5, 1, and 2. The selected silos had either a conical, flat-top, or no roof. MacDonald et al. [31] concluded that there was a significant difference between the pressure distribution of closed-top and open-top silos. MacDonald et al. [31] reported the presence of a large inward internal pressure when examining the open-top silos. According to Hua and Letchford [32], the wind profiles applied to the tank shell and roof of open-top tanks specified in Australian/New Zealand Standard [33] is based on the these two studies [30, 31]. Moreover, the roof load on tanks and silos specified in latest edition of ASCE-7 [34] also originates from these two studies [30, 31].

Later, wind tunnel experiments conducted by Portela and Godoy [35, 36] investigated the effect which roof configuration (including dome and conical roof geometries) has on wind pressure distribution. They concluded that the wind pressure distribution on the shell of tank did not differ

depending upon the roof geometry, but a conical roof would increase the pressure on the roof. Yasunaga and Uematsu [37] also conducted wind tunnel tests on open-top tanks with aspect ratios of 0.5 and 1.0. Additionally, dynamic finite element analyses were conducted using the wind distribution profiles recorded at every instant during a wind tunnel test. They concluded that the buckling capacity obtained by conducting a dynamic analysis is more conservative than the buckling capacity obtained by a static analysis.

As an alternative, computational fluid dynamics (CFD) can be used to obtain the wind pressure distribution on tanks. A CFD analysis has the advantage of not requiring a BLWT facility, which may not be available to many researchers. Iamandi et al. [38] conducted CFD and BLWT on tanks with conical roofs. The result of the CFD and BLWT analyses had agreed well with each other, and Iamandi et al. [38] recommended that CFD be used to obtain wind pressure distributions in order to minimizes the cost.

With the wind pressure distribution obtained, the stability of a tank can be further investigated. To prevent tanks from global buckling, top wind girders are installed on open-top tanks. The expression for sizing wind girders was first presented in an America Water Work Association (AWWA) document [39]. This expression, however, was determined to be overly conservative, and therefore, researchers have been developing better design guidelines [40-47].

In the past few decades, with the development of the finite element method (FEM), research analyzing tanks has thrived. Using a finite element (FE) static analysis, including a linear bifurcation analysis (LBA) and a geometrical nonlinear analysis with imperfection (GNIA), to examine tank behavior is a common practice. Dynamic analysis has been deemed unnecessary, because resonance effects on tanks subjected to the wind loading do not dominate [8, 48, 49], and dynamic analyses can be time consuming. Greiner and Derler [50] conducted analyses involving geometric nonlinearity and material plasticity with geometric imperfections. It was observed that short tanks are more sensitive to the chosen imperfection types. They concluded that the buckling shape of a long cylindrical shell does not correspond with the first eigenmode. Godoy and Flores [51] conducted FEA to evaluate existing tanks, considering geometric nonlinearity and imperfections. They observed that many shells failing during hurricanes were not equipped with

top wind girders and thus investigated such tanks. The relationship between the imperfection sensitivity of a cylindrical shell with the height to diameter ratio and thickness to diameter ratio was proposed.

A recent study conducted by Zhao and Lin [52] studied tanks with aspect ratios ranging from 0.27 to 0.88 using a LBA and a GNIA. They reported that there were few studies considering an additional internal pressure induced by wind excitation on an open-top tank. In Zhao and Lin's paper [52], imperfections simulated depressions caused by welds and eigen-affine imperfection shapes. It was determined that the weld depression imperfections did not have an great impact on the buckling capacity of a tank as they did on the buckling capacity of a silo [53]. Zhao and Lin [52] also studied the effect of storing liquid in the tank, and concluded that the liquid helped stabilize the tank. Shokrzadeh and Sohrabi [54] studied the strengthening effect of stairways on tanks using a LBA. It was determined that stairways strengthen the tank under wind loads. However, this strengthening effect was not observed when tanks were subjected to internal vacuums, but the buckling mode shape of the tank did change.

This study compares the behavior of open-top tanks subjected to wind profiles specified in various design documents. An additional internal pressure (acting inward) is generated when an open-top tank is subjected to a gust of wind, and this internal pressure is considered in European [55] and Australian/New Zealand [33] design documents. Uematsu et al. [56] also proposed a wind profile which includes this internal pressure. The North American design documents, including API 650 [4] and ASCE-7 [34], however, do not distinguish between the pressure distribution on tank shells with an open- or a close-top geometries. In fact, the ratios of internal to external pressure can be greater than 1.0 in the wind profile specified in Australian/New Zealand Standard [33] for particular tanks. In other words, the internal inward pressure may almost double the design wind pressure on the tank shell in some cases.

By conducting a FEA, the behavior of tanks under selected wind profiles can be thoroughly investigated. Tanks with aspect ratios of 0.11, 0.2, 0.5, 1.0, 2.0, and 4.0 were adopted to represent a wide spectrum of common tank sizes. Analyses using a general purpose finite element package (ABAQUS [57]) weres conducted. An LBA and a postbuckling analysis were conducted to

simulate the behavior of a tank with different geometries. A comparison of the buckling capacities of tanks subjected to different wind profiles, the effects of internal pressure, and the effects of imperfections are then discussed based on the results obtained. To gain a better understanding of the quality of the results obtained, a mesh convergence study and a study on the load-arc length increment of the postbuckling analyses were conducted.

The tank designs and the wind profiles employed in this study are discussed in Section 3.2. Some background knowledge of the analyses conducted, the study on mesh and load increment, and the computational model are presented in Section 3.3. The result of the FEA are presented and discussed in Section 3.4. Finally, the conclusions of this study are given in Section 3.5.

3.2   Analysis Parameters

3.2.1   Tank Design

Six different open-top tanks, which cover a wide range of height to diameter aspect ratios, were modeled using ABAQUS version 2018 [57]. The geometries of the tanks examined in this study are compiled in Table 3-1. All six tanks were composed of five 2.44 m tall courses with stepped thickness. The shell thickness of Tanks A, B, C, and D were designed in accordance with the 1-foot method specified in API 650 [4] and the shells of Tanks E and F were designed using the variable-design-point method presented in API 650. The shell course thicknesses can be found in Table 3-2, where *t* is the thinnest thickness of a tank course. The allowable design stress was 159 MPa, the specific gravity of the liquid stored in the tank was 1.0, and the corrosion allowance was zero for all six tanks.

Top wind girders were included in the models to maintain the circular profile of the top edges of the tanks. The top wind girders were designed in compliance with API 650 [4], with a wind speed of 145 km/h. Note that the transformed shell height of Tank C was slightly larger than the maximum allowable unstiffened height specified in API 650. However, to make it consistent with the other models, an intermediate wind girder was not included in the model. The dimensions of the wind girders are listed in Table 2-2. Wind girder details can be found in API 650. Note that for Tanks B, C, and D, the top wind girders were angle profiles with the long legs placed horizontally.

The section modulus of the top wind girder provided for Tank A was slightly larger than the minimum requirement in API 650. However, if a smaller section which satisfied the demand was adopted, it resulted in the top wind girder buckling rather than the shell when conducting the LBA. The objective of the present paper is to study the buckling of the shell, and thus a larger wind girder section was selected.

The material specification of the tanks was ASTM A36 steel [58]. The Young's modulus, E, was 200 GPa, the Poisson's ratio, v, was 0.3, and the mass density, ρ, was 7900 kg/m³. For the material constitutive relationship, true stress-strain curve specified in ASME BPVC Section VIII, Division 2 [59] was employed for the cases that considers the material nonlinearity. The yield stress was 250 MPa, and the ultimate tensile stress was 400 MPa. The relationship between the stress and the true strain is plotted in Figure 3-1. Next, the wind profiles adopted in this study are discussed.

3.2.2   Wind Profiles

Four different wind profiles were utilized in this paper, including wind profiles specified in API 650 [4]/ASCE-7-16 [34], Eurocode (EN 1993-4-1) [55], and AS/NZS (Australian/New Zealand standard, AS/NZS 1170.2:2011) [33]. A wind profile proposed by Uematsu et al. [56] was also employed in this section. Among the wind profiles adopted, the profile specified in API 650/ASCE-7 was the most distinct. This profile dictates that the wind pressure should be uniformly distributed on the projected surface of the tank shell with a drag coefficient (C_f) of 0.63. This profile is illustrated in Figure 3-2. As a consequence, the actual wind pressure on the tank shell was the product of P and C_f or P and C_p (C_p will be defined in the next paragraph.) Here, P was defined as the pressure level that a gust of wind reaches without any obstacle. In other words, it was the product of the gust factor and the velocity pressure.

On the other hand, the wind pressure distributions of the other three wind profiles were given as a function related to circumferential position. In Eurocode [55], the wind profile is expressed as in Eqn. (17).

$$
\begin{aligned}
C_{pe}(\theta) = &-0.54 + 0.16(D/H) + [0.28 + 0.04(D/H)]cos(\theta) \\
&+[1.04 - 0.20(D/H)]cos(2\theta) + [0.36 - 0.05(D/H)]\,cos(3\theta) \\
&-[0.14 - 0.05(D/H)]\,cos(4\theta)
\end{aligned}
\tag{17}
$$

Here, C_{pe} is the normalized circumferential pressure distribution on the external shell, and θ is the circumferential angular position in degrees (a positive coefficient indicated that the wind is blowing toward the surface). Note that for tanks with an H/D ratio less than 0.5, an H/D ratio of 0.5 should be used in the Eqn. (17). As specified in the Eurocode, an additional internal inward pressure (C_{pi}) should be taken into account for an open-top tank. Regardless of the tank size, C_{pi} has a constant value of -0.6, indicating a constant vacuum. The normalized circumferential pressure distribution on the shell (C_p) was then defined as the difference between C_{pe} and C_{pi}, and the wind pressure on the tank shell subjected to a gust of wind was the product of P and C_p. This implies that if a gust of wind blows at a pressure level (P) of 1.0 Pa, without any obstacles, it generates a pressure of 1.6 Pa on the windward side (when $\theta = 0$) for an open-top tank.

The AS/NZS wind profile can be expressed as shown in Eqns. (18) ~ (21).

$$C_{pe} = k_b C_{pe,1} \tag{18}$$

$$\begin{aligned} C_{pe,1}(\theta) = &-0.5 + 0.4\cos(\theta) + 0.8\cos(2\theta) \\ &+0.3\cos(3\theta) - 0.1\cos(4\theta) - 0.05\cos(5\theta) \end{aligned} \tag{19}$$

$$\begin{aligned} k_b = \;&1.0 && \text{for } C_{pe,1}(\theta) \geq -0.15 \\ &1.0 - 0.55\big(C_{pe,1}(\theta) + 0.15\big)\log_{10}\big(H/D\big) && \text{for } C_{pe,1}(\theta) < -0.15 \end{aligned} \tag{20}$$

$$C_{pi} = -0.9 - 0.35\log_{10}\big(H/D\big) \tag{21}$$

This wind profile is only valid for tanks with aspect ratios (H/D) in the range of 0.25 to 4.0. It should be noted that Tanks E and F were not within this range. In addition, the API 650/ASCE-7 wind profile is specified in AS/NZS as an overturning check.

The wind profile proposed by Uematsu et al. [56] can be expressed as shown in Eqns. (22) ~ (30).

$$C_{pe}(\theta) = 0.72 - A\sin^c(1.06\theta) \qquad\qquad \text{for } 0 \leq \theta \leq 85° \tag{22}$$

$$C_{pe}(\theta) = B\cos\big(2.25(\theta - 85)\big) - 0.2 \qquad\qquad \text{for } 85° < \theta \leq 125° \tag{23}$$

$$C_{pe}(\theta) = -0.2 \qquad\qquad \text{for } 125° < \theta \leq 180° \tag{24}$$

$$C_{pi} = -0.35 - 0.5\,H/D \tag{25}$$

$$A = 0.72 - C_{pm} \tag{26}$$

$$C_{pm} = -0.7 - 0.5\,{}^{H}\!/_{D} \tag{27}$$

$$c = \frac{ln({}^{C_{ps}}\!/_{A})}{ln(sin(1.06\theta_0))} \tag{28}$$

$$\theta_0 = 43 - 8\,{}^{H}\!/_{D} \tag{29}$$

$$B = C_{pm} + 0.2 \tag{30}$$

This wind profile is only valid for tanks with aspect ratios between 0.25 and 1.0, which excludes Tanks A, B, E, and F. In this study, even though the author were aware that the AS/NZS and the Uematsu (referring to [33] and [56], respectively) wind profiles were not applicable to Tank E, analyses using these two profiles were still conducted on Tank E since this is a common tank size in the U.S for oil and gas industry. Figure 3-3 shows the wind profiles applied to Tank D (H/D=0.5).

In terms of implementing these models in ABAQUS, the load distribution function in ABAQUS only allows for exponents that are integers. Eqn. (28), however, generates c values that are not integers for Eqn. (22). Thus, in order to implement the model into ABAQUS, $C_{pe}(\theta)$ for $0 \le \theta \le 85°$ was fitted using a Fourier series, and can be expressed as in Eqn. (31).

$$C_p(\theta) = a_0 + a_1\cos(\theta) + a_2\cos(2\theta) + a_3\cos(3\theta) \tag{31}$$

The corresponding coefficients (e.g. a_1, a_2, and a_3) were solved for and recorded in Table 3-4. Note that the wind pressure was assumed to be constant with respect to tank height, since the height of the tanks examined was relatively short, and the vertical profile is almost constant along the axial direction of the tank. Therefore, the wind pressure distribution was considered constant along the tanks' heights in this study.

Note that among the four wind profiles mentioned, the only profile that did not explicitly include an additional internal pressure was the API 650/ASCE-7 profile. According to McGrath [43], an internal vacuum of 200 Pa should be add to the design pressure when the design wind speed is 160 km/hr. While there will not be a vacuum build up in an open-top tank, this factor is still accounted

for. As a consequence, it can be considered a compensation of the internal pressure on an open-top tank induced by wind. This is equivalent to 12% of the design pressure and is much smaller than what is specified in other codes. Now that the design of the tanks and the wind profiles adopted in this study have been discussed; the implementation of the finite element model is discussed in the next section.

3.3   Finite Element Analysis Implementation

In this section, the methods used to analyze the tanks are discussed. First, the type of analyses adopted are discussed along with some background information on these analyses. Next, the types and amplitudes of the imperfections studied are illustrated. A mesh convergence study and a study on the input parameter for the postbuckling analyses were then conducted to ensure a high quality analysis. Finally, the FE models were constructed using the parameters selected.

3.3.1   Analysis Algorithm

In this study, a static LBA and a postbuckling analysis including geometric, and material nonlinearities were conducted. The LBA was conducted first to obtain a computational simple preliminary estimation of the buckling capacity. The buckling capacity (eigenvalue) is solved for based on a geometrically perfect and elastic condition. During the analysis, a gravity load (gravitational acceleration $g = 9.8$ m/s) was applied as a preload. Then the wind load was applied to solve for the buckling capacity using a LBA step. Note that the buckling capacity reported is P rather than the product of P and C_p, because P is directly related to the wind speed. However, for different wind profiles, the C_p value varies. The objective of this study is to relate the buckling behavior of tanks to the wind speed for design purpose, rather than studying the buckling pressure of the tank shells. In this regard, reporting the product of P and C_p is not a good metric. Next, geometric nonlinearity, material plasticity, and geometric imperfections were taken into account.

The postbuckling analysis was conducted using Riks algorithm. Riks analysis applies a small portion of the specified external load as an incremental load to the structure at each step using an arc-length algorithm. While classic Newton-Raphson method (general static analysis) was also investigated, it did not yield results with as much accuracy as the Riks analysis did [12]. Thus,

Riks analysis was employed as the main analysis type in this study. By gradually increasing the applied load, the nonlinear behavior of structures can be captured. Analyses conducted using Riks analysis included geometrically nonlinear elastic analysis (GNA), geometrically and materially nonlinear analysis (GMNA), geometrically nonlinear elastic analysis with imperfection (GNIA), and geometrically and materially nonlinear analysis with imperfection (GMNIA). The buckling capacities resulting from those analyses were determined using the relationship between the displacement and the load proportionality factor (the proportion of the applied external load, LPF). The peak in the displacement to LPF diagram for an analysis was considered to be the buckling capacity of the system. It is important to note that the displacement history chosen for the diagram was the total displacement history of the node where the onset of buckling occured (the node having the maximum displacement right after the LPF reaches its first peak). The result of these analyses provide adequate information for a practical tank design.

For the analyses including material nonlinearity (e.g. GMNA and GMNIA), the stress-strain relationship is specified in Figure 3-1. The imperfection profiles employed in this study will be further examined in next section.

3.3.2 Imperfection Geometry

It is well-known that thin cylindrical shells, such as tanks, are prone to various types of imperfections resulting from the construction process. Here, potential imperfection types including out-of-plumbness (OOP) imperfection, imperfections resulting from uneven support (settlement imperfections) and eigen-affine imperfections were explored.

A schematic of the OOP imperfection and the settlement imperfection are given in Figure 3-4. Both imperfection amplitudes examined followed the API 650 [4] limit. The former imperfections limit is specified in API 650 Paragraph 7.5.2 and the latter limit is specified in API 650 Paragraph 7.5.5. To investigate the influence of these two kinds of imperfections, a LBA was conducted. Tank E was examined for this purpose with a global mesh size of 25 cm. The Eurocode [55] wind load distribution was used with the wind blowing horizontally. The wind pressure on tanks with these two types of imperfections were not perpendicular to the shell due to the tilt. For the OOP imperfection, the shell of the tank was tilted by $H/200$, which in this case result in a 6.1 cm imperfection. On the other hand, for the settlement imperfection, it was assumed that there was no

concrete ringwall under the tank and the difference in elevation between $\theta = 0°$ and $\theta = 180°$ was 2.6 cm. The element type was S4R, and the lower edges of the tanks were fixed. The LBA results for the tanks with these two types of imperfections can be seen in Table 3-5. In this table, $+x$ stands for the tank tilting towards $+x$ direction or settling in $+x$ region but uplifted in $-x$ region, considering the center of the tank bottom to be located at the origin. Table 3-5 shows that both type of imperfections increase the buckling capacity. The OOP imperfection increased the buckling capacity by 25%, which is a significant increase. However, the settlement imperfection did not greatly impact the buckling capacity. The increase caused by the settlement imperfection was less than 0.1%. This indicates that the possibility that Tank E is not sensitive to these types of imperfections under wind loading.

In contrast, it is well known that eigen-affine imperfections have a large impact on the buckling capacity of a tank. Thus, only this type of imperfection was used during the reminder of the study. For analyses with this type of imperfection, the nodes on a geometrical perfect tank are distributed according to the first buckling mode shape obtained through a LBA before a postbuckling analysis is performed. Based on the results presented by Sun et al. [41], the first buckling mode should have the most severe impact on the buckling capacity, and thus the first buckling mode was introduced as the imperfection shape in the GNIA and the GMNIA. Four levels of imperfection amplitudes were employed, and t was used to express the imperfection amplitude. Amplitudes including $0.01t$, $0.1t$, $0.5t$, and $1.0t$ were adopted in this study. These imperfection amplitudes were widely used by researchers, and larger amplitudes did not yield significantly smaller buckling loads [41]. In terms of conducting the GNA, the GMNA, the GNIA, and the GMNIA, a gravity load was again applied as a preload, and the wind load was applied using a Riks step. The material nonlinearity and/or the geometric imperfection was applied during these analyses. To ensure acceptable results, mesh convergence and load increment for postbuckling analyses were conducted and are discussed in the next section.

3.3.3   Validation of Input Parameters for Postbuckling Analysis

The accuracy of a FEA heavily depends on the mesh size of the model. A mesh convergence study was therefore conducted to ensure the quality of the analyses. Here, a mesh size index $(\beta\sqrt{Rt})$, where R was the radius of a tank, was adopted to ensure consistent mesh sizes between different

models. Tank E was adopted in this section, and loaded with the Eurocode wind profile. An LBA and a GMNIA were conducted to observe mesh convergence. The maximum load increment for the GMNIA was 50 Pa, the minimum load increment was 1E-11 Pa, and the total number of steps during the analysis was 200. Mesh scaling factors (β) of 0.3, 0.5 and 1.0, which result in global mesh sizes of 15 cm, 25 cm and 50 cm, were adopted. The imperfection was an eigen-affine imperfection (first mode) and the amplitude was 0.5t. The LBA buckling capacities of the tanks with different mesh sizes were 867.4 Pa, 877.3 Pa, and 923.0 Pa, respectively. The GMNIA results are shown in Figure 3-5. The x-axis in Figure 3-5 displays the total displacement history of the node where the onset of buckling occurs, denoted as w, and normalized by t. The y-axis represents the history of the LPF normalized with by design wind pressure, which was 838.8 Pa. From Figure 3-5, it can be observed that there is only a 1% difference between the LBA buckling capacities when β has a value of 0.3 or 0.5, however, the LBA buckling capacity when β=1.0 is much higher. Based on the GMNIA results, all three analyses seem to produce similar values. A β value of 0.5 should be adequate for obtaining a reasonably accurate results. Therefore, the mesh scaling factor (β) will be taken as 0.5 for the remainder of this study.

When conducting a Riks analysis, the solution is also dependent on the size of the load increment. Here, load increment refers to the maximum and minimum load increments applied at each step during an analysis. In ABAQUS, even though ABAQUS allows users to set the upper and lower bound of the increment size, users are not able to control the size of the individual steps if the step size is not assigned as a specific value. Users must have a thorough understanding about how increment size affect results. To this end, the influence of increment size was investigated. In this section, Tanks C and E were used. The mesh scaling factor (β) was set as 0.5, which resulted in global mesh sizes of 8.7 cm and 25 cm for Tanks C and E, respectively. The Eurocode wind profile was adopted, and material nonlinearity was not taken into account. The imperfection amplitude was 0.5t (e.g. GNIA). The LBA buckling capacities (1813 Pa, and 877.3 Pa, respectively) were used as an index for sizing the step increment. The parameters used for the analyses are given in Table 3-6 and Table 3-7 for Tanks C and E, respectively. Control cases were determined based on the author's experience. The FEA results of the cases specified in Table 3-6 and Table 3-7 can be found in Figure 3-6. The x-axes in Figure 3-6 display the total displacement history of the node

where the onset of buckling occurred normalized with respect to t, and the y-axes represent the history of the LPF normalized with the design wind pressure.

Figure 3-6 is divided into two rows, where the first row studies the influence of the maximum load increment and the second row studies the influence of the minimum load increment. In Figure 3-6 (b), it was determined that if the maximum load increment exceeded 15% of the linear buckling load, it would be possible for the analysis to exclude the correct loading path. It can also be observed from Figure 3-6 (a) and Figure 3-6 (b) that when the maximum load increment is set less than 6% of the linear buckling capacity, the results converge. Setting the maximum load increment to less than 1% of the buckling capacity does not yield a significant difference in the GNIA load path, and greatly increases the run time (by about four times). It was therefore decided to set the maximum load increment less than 6% of the LBA buckling capacity but more than 1% of the LBA buckling capacity. On the other hand, there is no significant difference between the curves in Figure 3-6 (c) and Figure 3-6 (d) when examine the minimum load increment. The curves are almost on top of each other. Even when an extremely small minimum increment was employed, the analysis run time did not change. Therefore, the minimum load increment was arbitrarily set to 1E-11 Pa since a small minimum increment did not increase the run time and had a low potential to produce inaccurate results. Note that only analyses including geometric imperfections were studied in this section, while analyses without any geometric imperfections were excluded. This is due to the fact that without any imperfections, the algorithm may not be able to capture the buckling behavior numerically. Since the criteria for selecting the input parameters has been determined, construction of the FE models is presented in the following section.

3.3.4   Finite Element Models

Finite element models of all six tanks were constructed using ABAQUS. As mentioned previously, a mesh size index ($\beta\sqrt{Rt}$) was used to keep a consistent mesh size between the different models. A β value of 0.5, which provides a good balance between accuracy and time efficiency, was adopted. The mesh sizes obtained using the index β=0.5 were 4 cm, 6 cm, 9 cm, 14 cm, 25 cm, and 38 cm for Tanks A, B, C, D, E, and F, respectively. In other words, for Tank A, the mesh size of the elements was 4 cm $\times$ 4 cm in both the axial and circumferential direction in general. All the wind girders had at least four elements along their depth. S4R elements, which are reduced

integration, 4-node, quadrilateral shell element with large strain formulation, were used. The bottom edges of all six models were fixed and the top edges were free. Though it was suggested that a fully fixed bottom may overestimate the buckling capacity of a tank [60], the influence is of the effect relatively small since the buckling of the tank shells occurs at the upper portion of the tanks [41]. Figure 3-7 shows the finite element model of Tank F with overall view and close up view of top wind girder. Analyses were conducted using the parameters mentioned, and the results are presented in the following sections.

3.4   Results and Discussion

Using the parameters mentioned in the sections 2 and 3, FEA were conducted. First, LBA were performed to obtain the linear buckling capacities and the imperfection shape of the eigen-affine imperfections. Next, the load increments used for the postbuckling analyses were examined and the increment sizes for each tank were determined. By analyzing the results obtained, the effects of material nonlinearity, geometric imperfection and internal inward pressure can be discussed.

3.4.1   Linear Bifurcation Analysis

The results of the LBA indicate the upper bound of the buckling capacity for a tank which can be used as a preliminary design guide due to its high computational efficiency. The first eigenvalues of all six tanks for various wind profiles obtained from the LBA are compiled in Table 3-8, with the results normalized by the design wind load. Based on API 650, the design pressure of tank shell is $860(V/190)^2$ Pa (unit of V is km/hr in this equation), and is specified in API 650 5.2.1 (k). As there is a shape factor (C_D) of 0.6 being applied to the design pressure of the shell, the velocity pressure along with the gust factor shall be the design pressure divided by C_D, and thus, the velocity pressure times the gust factor will be $1440(V/190)^2$ Pa. The design wind speed is 145 km/hr, which is equivalent to 40.3 m/s. By substituting V=145 km/hr into the expression, the corresponding "design pressure" used in paper would be 838.8 Pa. It may be confusing that it does not correspond to the design pressure specified by API 650. However, to establish a baseline for a comparison purpose, this 838.8 Pa was referred to as design pressure since it is the pressure without any shape factor or pressure coefficient being applied. To apply the pressure profiles (EU, AS/NZS, profile

proposed by Uematsu) correctly, it shall be reasonable using a pressure without any drag coefficient being applied should be more reasonable.

For each case, the design pressure was 838.8 Pa based on a wind speed of 145 km/hr. The buckling mode shapes of Tanks A and E are presented in Figure 3-8. When the effect of tank geometry is examined, it is clear that Tanks A, B, and C have relatively higher buckling capacities. Take the buckling capacities obtained from the Eurocode wind profile as an example. The buckling capacity of Tank C is about twice the buckling capacities of Tanks D, E and F. The buckling capacities of Tanks A and B are even higher than the buckling capacity of Tank C. This relatively large difference is a result of the design shell thickness, tank height to diameter aspect ratio and thickness to radius ratio. The shell thickness of Tanks D, E, and F are controlled by the hydrostatic pressure, and are determined by either the one-foot method or the variable-point method. In contrast, the shell thicknesses of Tanks A, B, and C were controlled by the minimum thickness limit specified in API 650, rather than the hydrostatic pressure generated by the liquid stored in the tank. This results in a relatively thick shells, and thus raises the buckling capacity of the tanks. Similarly, relatively slender tanks having higher height to diameter aspect ratios (Tanks A, B, and C) have larger buckling capacity than relatively broader tanks having smaller height to diameter aspect ratios (Tanks D, E, and F).

When the buckling capacities obtained using different wind profiles are examined, the buckling capacities associated with wind profiles which consider the internal pressure are similar for any given tank, but the buckling capacities obtained when adopting the API 650/ASCE-7 wind profiles are very different. From Table 3-8, it can be seen that the ratio of the buckling capacity obtained from the LBA for to the design wind pressure for Tanks D and E can be close to, or even less than, 1.0 when the wind profiles take additional internal pressure into account. This result is reasonable for Tank E, since API 650 would require the presence of an intermediate wind girder. For Tank D, however, API 650 does not prescribe an intermediate wind girder. If a safety factor of two is assumed for the LBA buckling capacities, then the design of all the tanks with aspect ratios less than 1.0 (Tanks D, E, and F) needs to be revised if loaded with the Eurocode, the AS/NZS and the Uematsu wind profiles. However, if the API 650/ASCE-7 wind profile is utilized, all six tanks are safe, as their buckling capacities are at least twice the design pressure. Since the linear buckling

capacity of all six tanks have been obtained, the load increment can now be determined for the following postbuckling analyses.

3.4.2   Parameters for the Postbuckling Analysis

Based on the LBA buckling capacities obtained in the section 4.1, the load increment for each case can be determined. For convenience, except for the analysis of Tanks A and B, a standard set of parameters was selected. The maximum load increment was 50 Pa (which is between 1.0 and 6.0% of the LBA buckling capacity of all four cases), the minimum load increment was 1E-11 Pa, and total number of steps in each analysis was 200. For the analyses associated with Tanks A and B, the parameters used are compiled in Table 3-9 and Table 3-10, respectively. Postbuckling analyses including GNIA, and GMNIA which consider geometric imperfections were conducted based on these parameters.

However, when the GNA and GMNA which do not consider geometric imperfections were conducted, the established parameters given in Table 3-9 and Table 3-10 did not produce adequate results. Without any imperfections introduced into the analysis, instability may not be properly achieved, as mentioned previously. Evidence of this statement is shown in Figure 3-9. In Figure 3-9, the tank has reached its buckling capacity, but the node with significant displacement is on the leeward side of the tank. In addition, the buckling capacities obtained by the GNA and the GNMA using the standard parameters usually exceeded the buckling capacities obtained by the LBA, which is incorrect, as the buckling capacities obtained by the LBA should be an upper bound. This indicated that the Riks analysis may not capture the correct buckling behavior of geometrically perfect structures. Thus, a smaller load increment, with a maximum of 5 Pa, a minimum of 1E-11 Pa, and 600 steps was adopted for most of the GNA and GMNA cases. The only exception was Tank E, which was loaded with Uematsu wind profile, as the buckling capacity obtained using these updated parameters still exceeded the LBA buckling capacity. Thus, for this case, the maximum increment was set to 2.5 Pa with 800 steps. Now that the parameters of all analyses have been set, the result of the analyses can be obtained and are presented next.

3.4.3   Effects of Different Wind Profiles

To discuss the effect of different wind profiles, Tank D is examined in this section because all the wind profiles are valid, and Tank D is the only tank whose LBA buckling capacity is less than the design pressure for some of the wind profiles. Postbuckling analyses using Riks algorithm are conducted without material nonlinearity (GNA, GNIA). Note that postbuckling analyses were conducted for each possible combination, but for the simplicity of the discussion, the results of only one or two configuration will be presented in each section. For complete analysis results, refer to Appendix A. The analyses results are presented in Figure 3-10 and Figure 3-11. In both figures, the x-axes represent the total displacement history of the node where buckle occurs normalized with respect to t, and the y-axes display the pressure normalized with the design pressure, 838.8 Pa. For all figures in following sections pertaining to postbuckling analysis results, the axes of the figures will be the same as in Figure 3-10. In addition, some of the data points in later stage of the analysis are removed to avoid ambiguity. Different curves represent different imperfection amplitudes, and the curve with 0t represents a GNA, analysis without geometric imperfection. A solid horizontal line indicates the normalized LBA buckling capacity, and a dashed horizontal line represents the normalized design wind pressure.

In Figure 3-10, it can be observed that the buckling capacity of Tank D is lower than the design pressure (the dashed horizontal line) for most cases. The only profile that produces buckling capacities that are always larger than the design pressure, regardless of imperfection amplitude, is the API 650/ASCE-7 profile. As mentioned previously, this is the only profile which may not sufficiently address the effect of the internal inward pressure. Without taking the additional internal pressure into account, the buckling capacity is much higher than buckling capacities obtained using the other profiles.

The difference in buckling capacities obtained from a tank loaded with the Eurocode profile and the AS/NZS profile (as shown in Figure 3-11) results from the differing magnitude of the internal pressure term. The internal pressure coefficient C_{pi} specified in the Eurocode is 0.6 regardless of tank size; while the internal pressure specified in the AS/NZS varies depending on the aspect ratio of the tank resulting in an internal pressure of 0.79 for Tank D. However, it is interesting to note that the C_{pi} specified in the AS/NZS is 30% larger than the C_{pi} specified in the Eurocode, and the

$C_p(0)$ specified in the AS/NZS is 12% larger than the $C_p(0)$ specified in the Eurocode. Nevertheless, the buckling capacity obtained utilizing the Eurocode profile is only 6% larger than what is obtained when the AS/NZS profile is utilized. Note that the pressure on the tank shell is the product of P and C_p. Based on these observations, it appears that the buckling capacity does not only depend on the pressure level at the windward stagnation point ($C_p(0)$), but also on the pressure distribution on the windward region. Similarly, since the $C_p(0)$ specified in the Uematsu profile is smaller than the $C_p(0)$ specified in the AS/NZS and the Eurocode, the resulting buckling capacity is higher.

3.4.4 Effects of Tank Size

To discuss the effects of tank aspect ratio, the Eurocode wind profile is adopted since this profile is valid for all the adopted tank geometries and it considers the additional internal pressure. Postbuckling analyses using Riks algorithm are conducted without material nonlinearity (GNA, GNIA). The results of these analyses are presented in Figure 3-12. Similar to the discussion in section 3.4.1, The relatively more slender tank, Tanks A, B, and C have a higher buckling capacity compared to the design pressure because the thickness of these tanks is larger than the thickness required to resist the hydrostatic pressure produced by the product the tanks will store. The thickness to diameter ratios (*t*/*D*) can be found in Table 3-2. It can be observed that the *t*/*D* ratios of Tanks A, B, and C are higher than the *t*/*D* ratios of Tanks D, E, and F. While this information does provide insight to why there is a difference in buckling capacities, the *t*/*D* ratio alone does not explain the following observation. For example, the *t*/D ratio does not provide a good indication of buckling capacity when the *H*/*D* ratio is less than 1.0, as the thicknesses are sized according to the hydrostatic pressure. Tank D has a higher *t*/*D* ratio but a lower buckling capacity than Tank E.

There is a significant drop in the buckling capacity of Tank A when comparing the postbuckling analysis and the LBA. The drop in the buckling capacity is due to the geometric nonlinear behavior of Tank A. The deflected shape of Tank A right after the onset of the buckling, along with the first mode shape of Tank A, are presented in Figure 3-13. By comparing subfigures (a) and (b) in Figure 3-13, it is observed that the deformed shapes obtained from the two analyses are different. In

subfigure (a), there are waves on the windward side of the shell. On the other hand, in subfigure (b), there are no such waves. This indicates that LBA could not capture the actual behavior of the tank, and overestimates the buckling capacity. In addition for Tank A, the magnitude of imperfection amplitude does not change the GNIA results that much (Figure 3-12(a)). This also explains why tall tanks are not sensitive to eigen-affine imperfections. These observations are similar to what Greiner and Derler [50] reported.

The buckling capacities of Tanks D and E are lower than the design pressure without the application of a safety factor for the most of the cases. Note that API 650 prescribes an intermediate wind girder for Tank E but not Tank D. However, the buckling capacities of Tanks D and E do not differ substantially (Figure 3-12 (d) and (e)). The buckling capacity of Tank F is relatively high compare to Tanks D and E, but it would not be conservative enough when a relatively small imperfection ($0.1t$) is applied (Figure 3-12 (f)). The buckling capacity of Tanks D and E are close, but the criteria indicates that Tank E needs one more wind girder, but not Tank D. Among the six tanks examined, it can be observed that the buckling capacity of the tanks decreases as the aspect ratio decrease when the aspect ratio is high ($H/D > 1.0$), and the buckling capacity is not directly related to the aspect ratio for tanks with small aspect ratios ($H/D < 1.0$).

3.4.5 Effect of Material Plasticity

For the discussion on the material plasticity, Tanks A and E are examined and subjected to the Eurocode wind profile in order to examine a tall tank (Tank A) and a broad tank (Tank E). Postbuckling analyses using Riks algorithm were conducted with the material plasticity was applied (GMNA, GMNIA). For the material properties, refer to section 3.2.1. Tank A was chosen because it is the only tank in which the material plasticity significantly affects the buckling capacity. Tank E was chosen because it is a common tank size, and the behaviors of Tanks B, C, D, and F are similar to Tank E when material plasticity is the only factor considered. The result of the analyses can be found in Figure 3-14 and Figure 3-15. In both Figure 3-14 and Figure 3-15, the left subfigures exclude the material plasticity while the right subfigures consider material plasticity.

In Figure 3-14, it can be observed that the buckling capacity of Tank A obtained from the GNA/GNIA (e.g. without material plasticity considered) and the GMNA/GMNIA (e.g. with material plasticity considered) differ. There is a 20% drop in buckling capacity when material plasticity is introduced. To discuss the behavior of Tank A in more detail, the deflected shapes of Tank A under a critical scenario are presented in Figure 3-16. Subfigure (a) is the von Mises stress distribution at the mid-surface of the elements in Tank A without material plasticity applied immediately after buckling occurs (where the maximum total displacement is 17 cm), and subfigure (c) is the von Mises stress distribution at the mid-surface of the elements in Tank A with material plasticity applied at approximately the same maximum displacement level as in subfigure (a). It can be observed that the maximum stress levels differ by an order of magnitude between subfigures (a) and (c) in Figure 3-16. This is due to the yielding of the material. The distribution of the stresses is very different as well, and a close-up view of the top of the tank in subfigure (a) is provided in subfigure (b). It can be observed that the high stress is concentrated at the top wind girder in subfigure (b). The material plasticity plays an important role because of the stress concentration at the wind girder. As soon as the top wind girder yields, the wind girder no longer has the ability to maintain the top edge's circular profile. A well-functioning wind girder acts similarly to a pin in the radial and circumferential direction at the top edge of a tank, while a yielded wind girder at the top edge of a tank acts more similarly to a free edge. Since the top wind girder is designed for a much lower pressure level (about 1/8 of the buckling capacity), it is not surprising that the wind girder yields. It seems that for an effective evaluation of the stability of tall tanks, such as Tank A, material nonlinearity must be included.

On the other hand, material plasticity did not affect the behavior of Tank E. In Figure 3-15, the overall response to the wind loading (including the displacement-loading paths and the buckling capacities) did not differ when the only dependent variable was material plasticity. It can therefore be reasonably conclude that material nonlinearity does not impact the buckling capacity of broad tanks, since the buckling is controlled by the slenderness of the geometry rather than the material strength. This phenomenon was also observed in the responses of the other tanks (Tanks B, C, D, and F), though these results are not explicitly presented in this section.

3.4.6 Effects of Imperfection Geometry

In this section, the effects of different imperfection geometries are investigated. Eigen-affine imperfections produced by the first five buckling modes obtained from a LBA were considered and used in a GNIA. Tanks A and E were examined and subjected to the wind loads produced by the Eurocode wind profile. Postbuckling analyses using Riks algorithm were conducted and no material nonlinearity was applied. The results of these analyses are presented in Figure 3-17 and Figure 3-18.

Figure 3-17 shows the responses of Tank A with different imperfection geometries introduced into the model. In Figure 3-17, it can be observed that regardless of the imperfection amplitude, the displacement-loading paths, the deflection levels where the onset of buckling occurs, and the buckling capacities are similar. Flores and Godoy [51] stated that the buckling behaviors of tanks with higher aspect ratios are not affected by eigen-affine imperfections resulting from the first mode obtained by a LBA. It appears that tall tanks are not affected by eigen-affine imperfection resulting from higher modes of imperfection geometry as well.

On the other hand, for a short tank, the imperfection geometry had a larger impact on the buckling behavior. Figure 3-18 presents the responses of Tank E with different imperfection geometries introduced into the model. In Figure 3-18, it can be observed that when the imperfection amplitude is small ($0.1t$, subfigure (a)), there is a 10% difference in buckling capacity when imperfections of different buckling modes are introduced to the tank, compared to when the imperfection correspond to first mode obtained by a LBA. In addition, the higher the mode of the imperfection geometry, the higher the observed buckling capacity and stiffness with an imperfection amplitude of $0.1t$. When the imperfection is larger ($1.0t$, subfigure (b)), a similar behavior can be observed, but it appears that the tank with the imperfection geometry corresponding to the second mode is slightly stiffer than the tank with the imperfection geometry corresponding to the third mode. Nevertheless, there is no doubt that the first mode imperfection geometry is the critical case, since a broad tank with a first mode imperfection geometry has the lowest stiffness and buckling capacity. This is similar to what Sun et al. [41] reported. Thus, it can be stated that the imperfection geometry obtained from the first mode of a LBA affects the buckling capacity the most.

3.5   Conclusion

This paper provided a comparison of the behavior of six tanks under wind loading resulting from different wind profiles available in design guides. The information required to conduct an accurate postbuckling analysis was also provided. Using a Riks analysis, a GNA, a GMNA, a GNIA, and a GMNIA were conducted for the six selected tanks with aspect ratios (H/D) ranging from 0.11 to 4.0.

A mesh convergence study and a study on the load increment requirements for a postbuckling analysis were conducted. It was found that a mesh scaling factor (β) of 0.5 generates an adequately converged buckling capacity solution and is computationally efficient. For the load increment study, it was determined that the maximum load increment for a postbuckling analysis has a great impact on the convergence of an analysis. A set of criterion for describing the maximum load increment was proposed, in which the maximum load increment should be less than 6% of the first eigenvalue obtained from a LBA. To make the analysis computationally efficient, a maximum load increment no less than 1% of the first eigenvalue is also recommended. It was also concluded that the minimum load increment did not greatly affected the outcome of the analysis. Using the established parameters, a LBA and a postbuckling analysis were conducted.

The effect of wind loading under different wind distribution was discussed. The LBA buckling capacities for Tanks A, B and C are at least twice as high as the design pressure for any given profile, but the buckling capacities of Tanks D, E and F are barely higher than the design pressure if the pressure distribution considers additional internal pressure. The same conclusion can be drawn from the results of the postbuckling analyses. It was observed that if the wind load is applied using the Eurocode pressure profile, the AS/NZS pressure profile, or the Uematsu pressure profile, the buckling capacities of Tanks D, E, and F obtained by the postbuckling analyses would be lower than the design pressure. This indicates that the current API 650 wind design pressure which underestimates the internal inward pressure for open-top tanks may be inadequate. Further investigation including a survey of existing tanks' wind performance in high wind velocity should be performed.

The influence of tank size was then examined. By conducting a GNIA, it was determined that since taller tanks ($H/D > 1.0$) have higher t/D ratios, the buckling capacities obtained from both the LBA and the postbuckling analyses are high. However, for broad tanks ($H/D < 1.0$), the buckling capacities are lower than the design pressure in most of the scenarios when imperfections are included. For broad tanks, since the shell thickness are designed by the 1-foot method or the variable-design-point method, the t/D ratio is not a good index for estimating the relative buckling capacity. For tall tanks (Tank A), the buckling shape obtained from a LBA and a postbuckling analysis were very different when geometric nonlinearity is introduced. It was concluded that a LBA is not sufficient for evaluating buckling behavior, including the buckling capacity and buckling shape of tall tanks. This helps explain the observation that tall tanks are not sensitive to eigen-affine imperfections.

Material plasticity had a great impact on the buckling capacity of Tank A, but not any other tanks. The t/D ratio of Tank A is high compared to the other tanks, and thus when Tank A is subjected to a strong wind gust, the wind girder yields before the limit of the shell is reached. Thus, material plasticity plays an important role in the behavior of Tank A under wind loading. For other tanks, however, the effect of material plasticity was subtle. Tank E was presented as an example. With material plasticity applied, hardly any difference was observed in buckling behavior. Therefore, it is recommended that material plasticity be considered in the design of taller tanks.

Various imperfection geometries of eigen-affine imperfections were investigated. It was determined that the mode shape resulting from the first mode obtained from a LBA is the most critical imperfection geometry for broad tanks (Tank E). Generally speaking, the higher the mode shape of the imperfection geometry, the higher the stiffness of the system, and the higher the buckling capacity. However, for tall tanks (Tank A) the mode shape of the imperfection geometry did not influence the observed buckling behavior.

3.6 Tables

Table 3-1. Geometries of tanks examined in this study. Tank height, H is 12.2 m for all tanks.

Tank name	Tank diameter D, m	Aspect ratio H/D
A	3.05	4.0
B	6.10	2.0
C	12.2	1.0
D	24.4	0.50
E	61.0	0.25
F	116	0.11

Table 3-2. Shell course thicknesses for modeled tanks.

Tank name	Shell thickness of courses, mm					t/D
	1 (Bottom)	2	3	4	5 (Top)	
A	6.0	5.0	5.0	5.0	5.0	1.63e-3
B	6.0	5.0	5.0	5.0	5.0	8.20e-4
C	6.4	5.0	5.0	5.0	5.0	4.10e-4
D	9.0	7.1	6.0	6.0	6.0	2.46e-4
E	22	17	8.0	8.0	8.0	1.31e-4
F	38	36	21	14	10	8.62e-5

Table 3-3. Size of the top wind girders for the modeled tanks.

Tank name	Detail type	Size (mm)	Distance from top edge of shell (cm)	Section modulus (cm^3)
A	a	65x65x8	0	8.46
B	b	65×65×6	2.5	27.0
C	c	100×75×8	8.0	67.0
D	d	125×75×8	9.6	308
E	e	b = 800	13	1570
F	e	b = 1150	16	3290

Table 3-4. Coefficients for the Fourier series for the wind profile proposed by Uematsu for circumferential angular position in the range of 0° to 85°.

Tank name	a_0	a_1	a_2	a_3
C	0.533	0.056	0.875	0.105
D	0.682	0.376	1.014	0.001
E	0.613	-0.379	0.945	-0.006

Table 3-5. The buckling capacities of Tank E resulting from the LBA with OOP and settlement imperfections.

Geometry	Perfect tank	With OOP imperfection		With settlement imperfection	
Direction		+x	-x	+x	-x
Buckling capacity (Pa)	877.3	1099	1095	877.6	877.6

Table 3-6. The GNIA setup for the load increment study of Tank C.

Case	Control	1	2	3	4	5	6
Maximum load increment (Pa)	50	100	1.0	300	50	50	50
Ratio of maximum load increment to LBA capacity	2.8%	5.5%	0.055%	16.5%	2.8%	2.8%	2.8%
Minimum load increment (Pa)	1.00E-11	1.00E-11	1.00E-11	1.00E-11	1.00E-1	1.00E-6	1.00E-16
Total step number in one analysis	200	200	1000	200	200	200	200

Table 3-7. The GNIA setup for the load increment study of Tank E.

Case	Control	1	2	3	4	5
Maximum load increment (Pa)	50	150	5.0	50	50	50
Ratio of maximum load increment to LBA capacity	5.7%	17%	0.57%	5.7%	5.7%	5.7%
Minimum load increment (Pa)	1.00E-11	1.00E-11	1.00E-11	1.00E-1	1.00E-6	1.00E-16
Total step number in one analysis	200	200	600	200	200	200

Table 3-8. Buckling capacities of all six tanks obtained from the LBA for various wind profiles.

	API		Australian		Eurocode		Uematsu	
	P_{LBA} (Pa)	P_{LBA}/P_{design}	P_{LBA} (Pa)	P_{LBA}/P_{design}	P_{LBA} (Pa)	P_{LBA}/P_{design}	P_{LBA} (Pa)	P_{LBA}/P_{design}
Tank A	40061	47.8	13455	16.0	19942	23.8	Not applicable	
Tank B	13090	15.6	4551	5.43	5691	6.79	Not applicable	
Tank C	4359	5.20	1591	1.90	1828	2.18	1815	2.16
Tank D	2084	2.48	805.6	0.961	849.8	1.01	1014	1.21
Tank E	2184	2.60	916.6	1.09	877.3	1.05	1181	1.41
Tank F	2646	3.15	Not applicable		1059.1	1.26	Not applicable	

Table 3-9. Parameters used for the postbuckling analysis of Tank A.

Wind profile	P_{LBA} (Pa)	Maximum load increment (Pa)	Ratio of maximum load increment to P_{LBA} (%)	Minimum load increment (Pa)	Step number
API 650/ ASCE-7	40061	1200	3.00%	1.00E-11	200
AS/NZS	13455	400	2.97%	1.00E-11	200
Eurocode	19942	600	3.01%	1.00E-11	200

Table 3-10. Parameters used for the postbuckling analysis of Tank B.

Wind profile	P_{LBA} (Pa)	Maximum load increment (Pa)	Ratio of maximum load increment to P_{LBA} (%)	Minimum load increment (Pa)	Step number
API 650/ ASCE-7	13090	600	4.58%	1.00E-11	200
AS/NZS	4551	100	2.20%	1.00E-11	200
Eurocode	5691	200	3.51%	1.00E-11	200

3.7 Figures
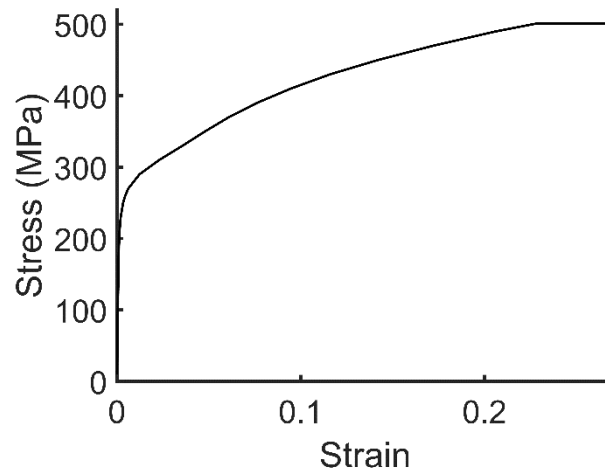
Figure 3-1. The true stress-strain diagram for ASTM A36 steel specified in ASME BPVC Sec. VIII, Div. 2 [59].

This figure is originally presented in Y.-C. Chiang and S. Guzey, "Influence of Internal Inward Pressure on Stability of Open-Top Aboveground Steel Tanks Subjected to Wind Loading," *Journal of Pressure Vessel Technology,* vol. 141, no. 3, p. 031204, 2019. Reproduction of the figure has been permitted by ASME. The author would like to acknowledge ASME for granting the permission.
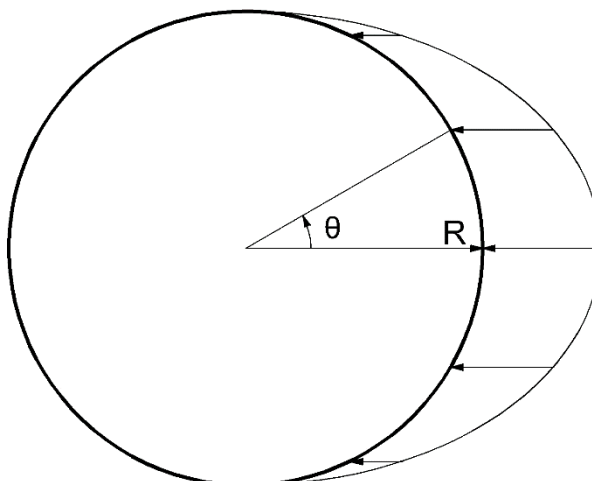
Figure 3-2. Schematic of the wind profile specified in ASCE-7. Wind blowing to the left.
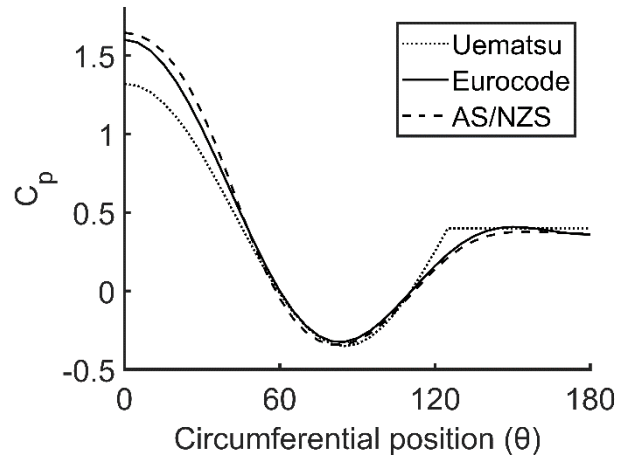
Figure 3-3. Wind profiles applied to Tank D (*H/D*=0.5).

(a)

⊢H/200⊣

(b)

26 mm
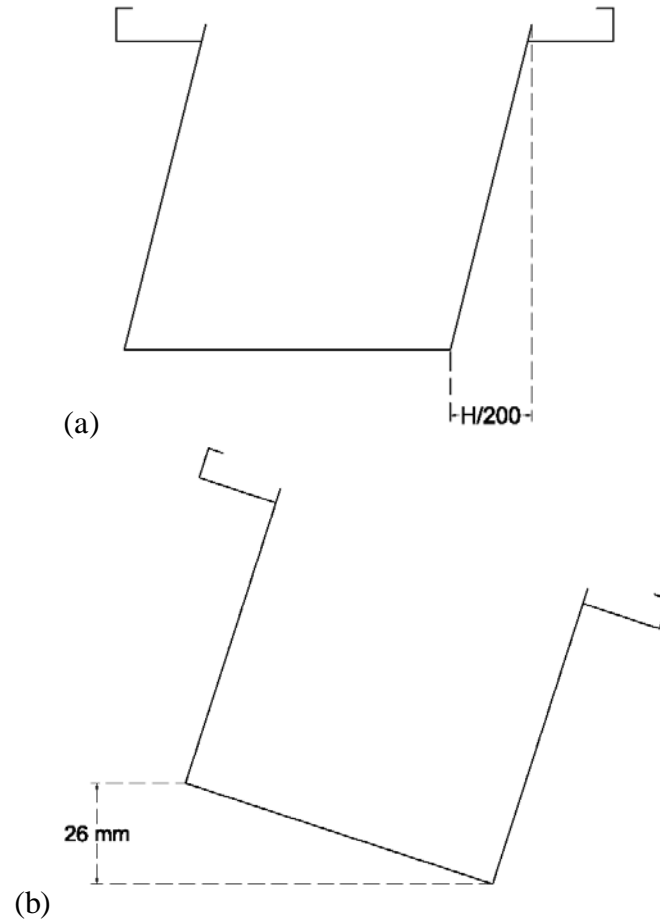
Figure 3-4. Schematic of (a) out-of-plumbness imperfection and (b) settlement imperfection. (Not to scale.)

This figure is originally presented in Y.-C. Chiang and S. Guzey, "Influence of Internal Inward Pressure on Stability of Open-Top Aboveground Steel Tanks Subjected to Wind Loading," *Journal of Pressure Vessel Technology,* vol. 141, no. 3, p. 031204, 2019. Reproduction of the figure has been permitted by ASME. The author would like to acknowledge ASME for granting the permission.
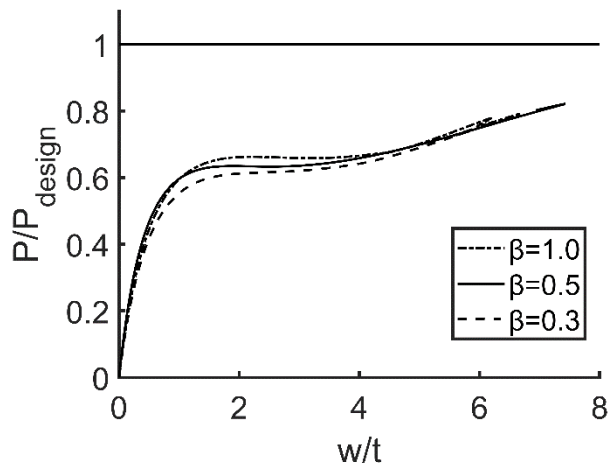
Figure 3-5. The GMNIA results from the mesh convergence study on Tank E.
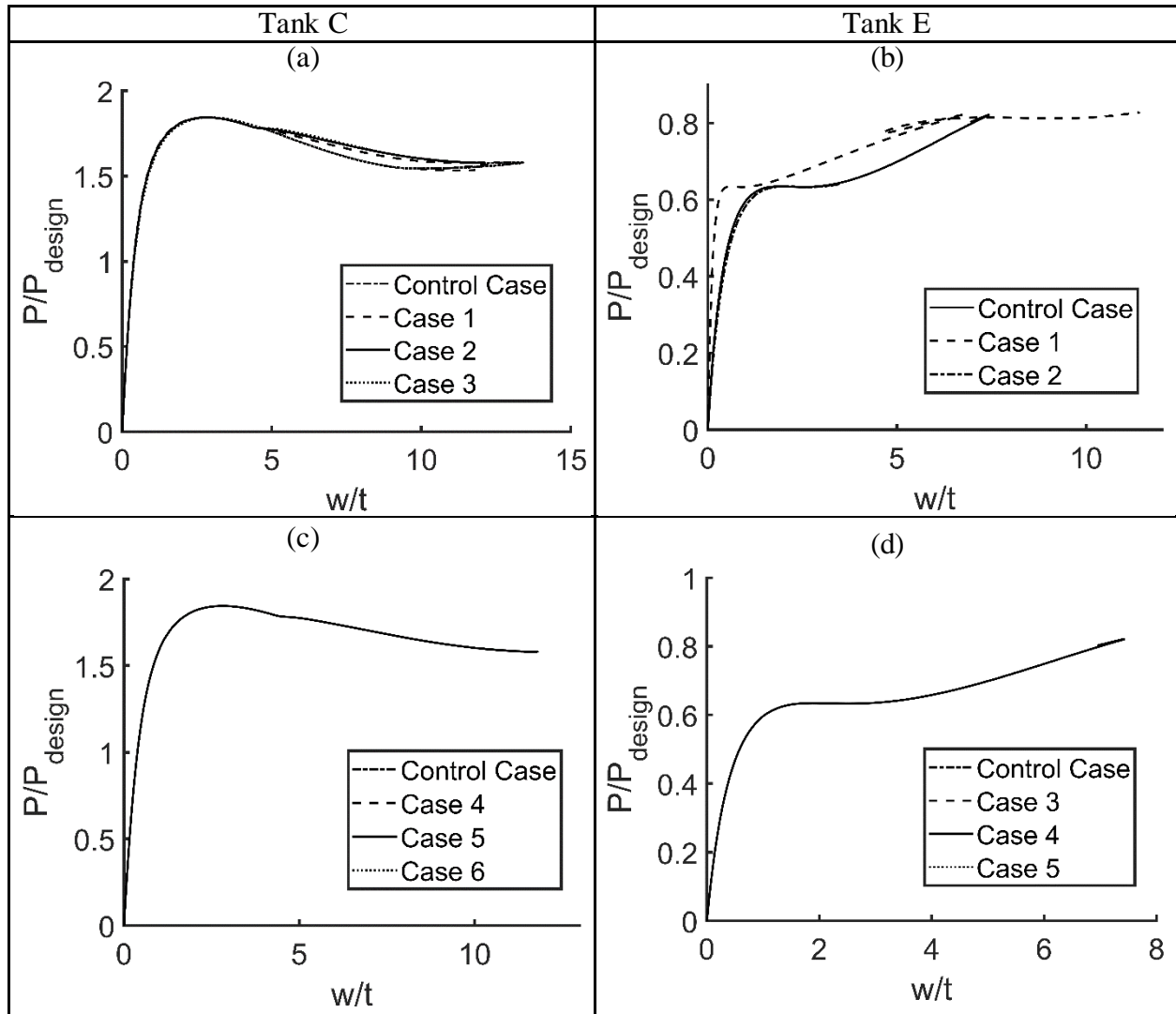
Figure 3-6. The GNIA results of the load increment convergence study on Tanks C and E.
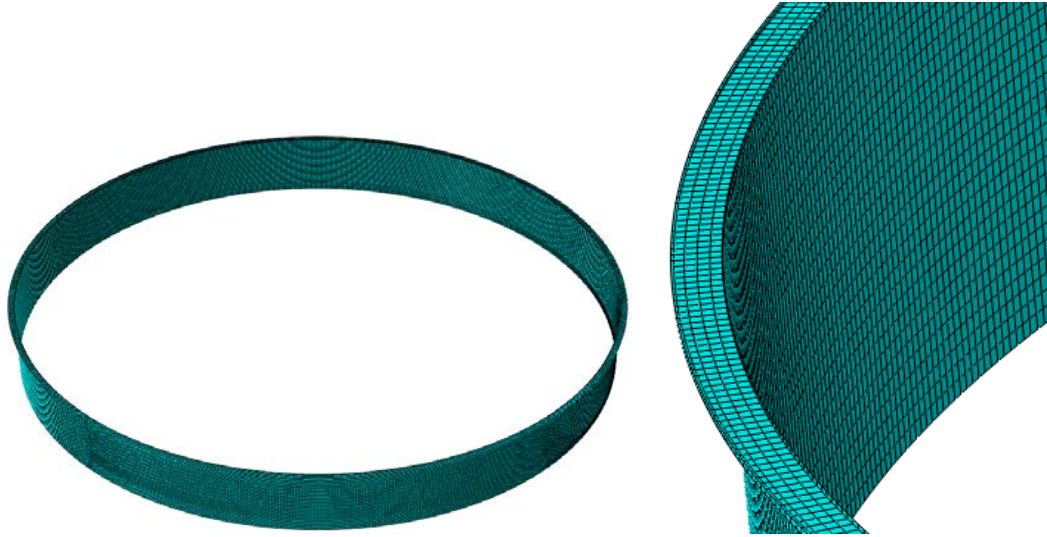
Figure 3-7. Model of Tank E with 35594 S4R elements. Overall view (left), and close-up view of the top wind girder (right).
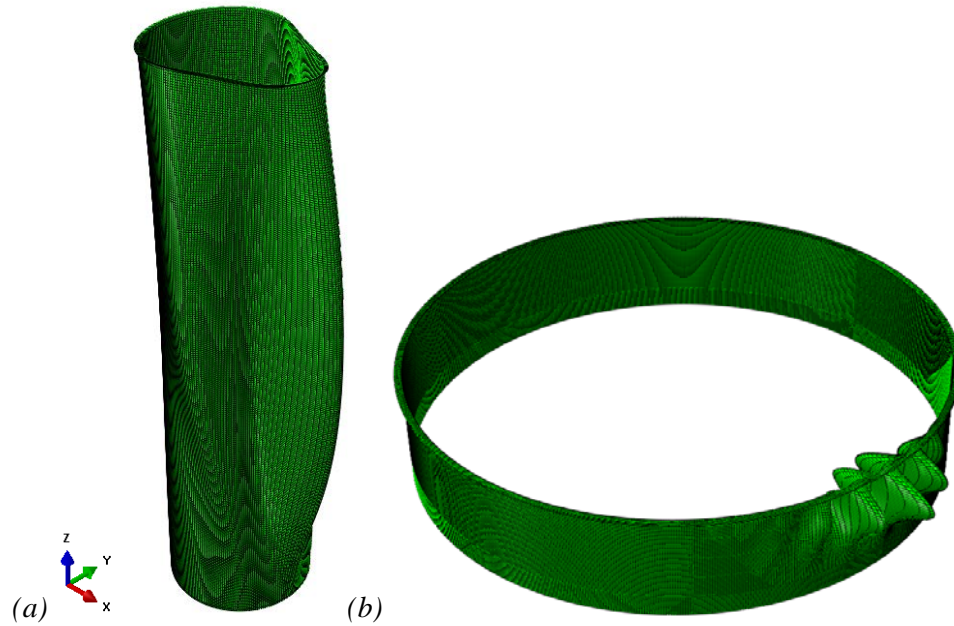
Figure 3-8. The LBA first mode shape of (a) Tank A and (b) Tank E subjected to wind loading in accordance with the Eurocode wind profile. Wind blowing from +x to –x direction.
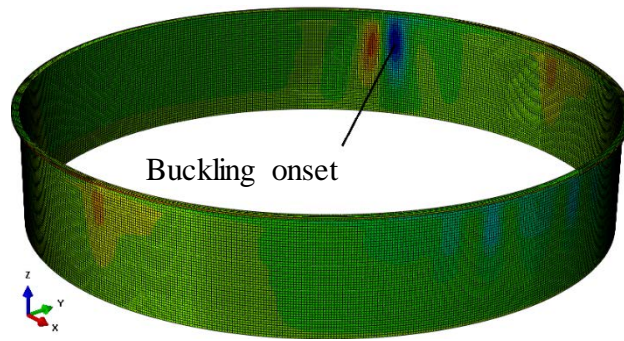
Figure 3-9. Radial deformation of the GMNA on Tank E subjected to the wind loading produced using the Uematsu profile. External wind pressure $P = 1273$ Pa. Wind blowing from $+x$ to $-x$.

This figure is originally presented in Y.-C. Chiang and S. Guzey, "Influence of Internal Inward Pressure on Stability of Open-Top Aboveground Steel Tanks Subjected to Wind Loading," *Journal of Pressure Vessel Technology,* vol. 141, no. 3, p. 031204, 2019. Reproduction of the figure has been permitted by ASME. The author would like to acknowledge ASME for granting the permission.
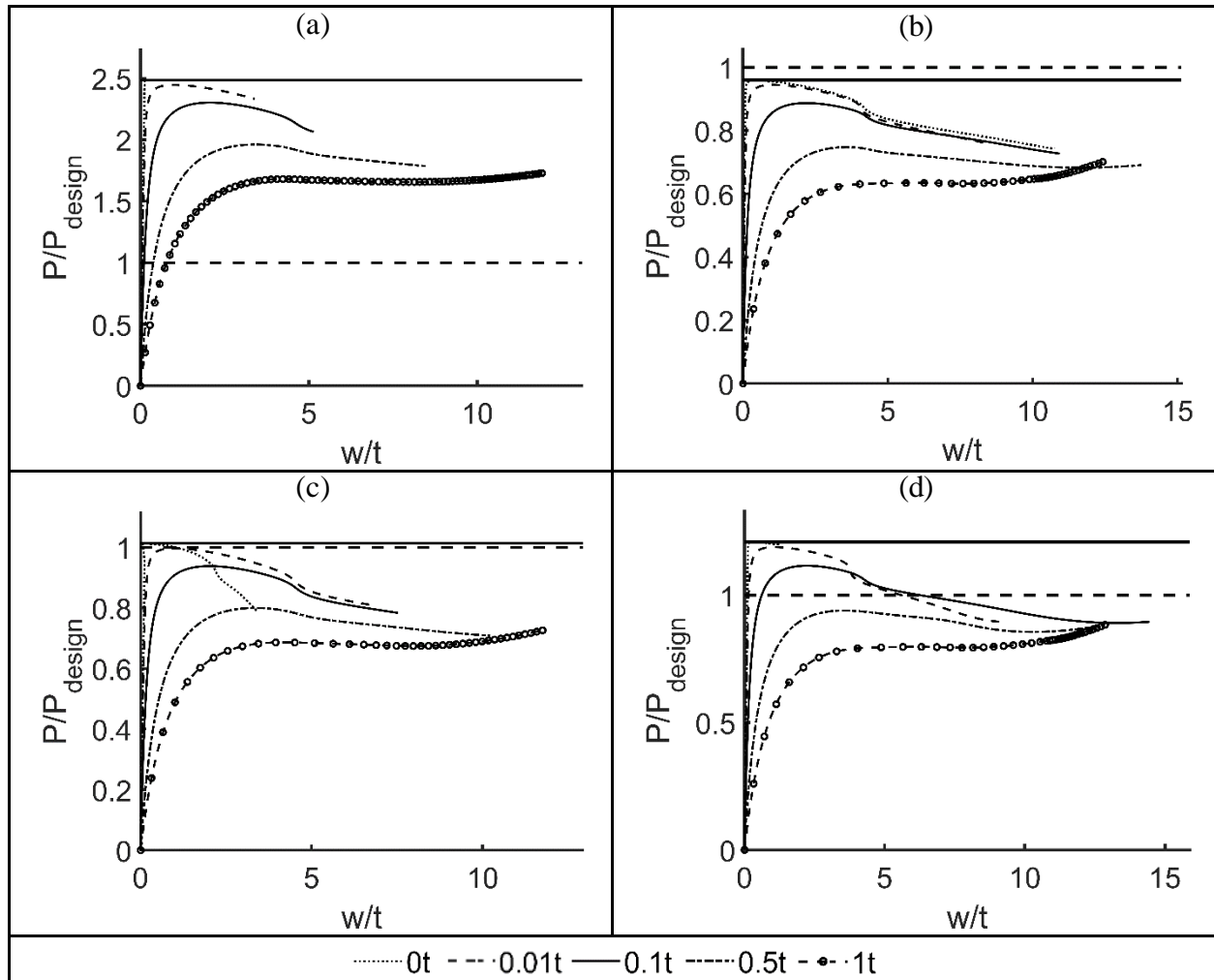
Figure 3-10. The GNIA results for Tank D subjected to wind loading resulting from the different wind profiles with different imperfection amplitudes. A Horizontal solid line represents the LBA buckling capacity, and a horizontal dotted line represents the design wind pressure. (a) API 650/ASCE-7 profile (b) AS/NZS profile (c) Eurocode profile (d) Uematsu profile.

This figure is originally presented in Y.-C. Chiang and S. Guzey, "Influence of Internal Inward Pressure on Stability of Open-Top Aboveground Steel Tanks Subjected to Wind Loading," *Journal of Pressure Vessel Technology,* vol. 141, no. 3, p. 031204, 2019. Reproduction of the figure has been permitted by ASME. The author would like to acknowledge ASME for granting the permission.
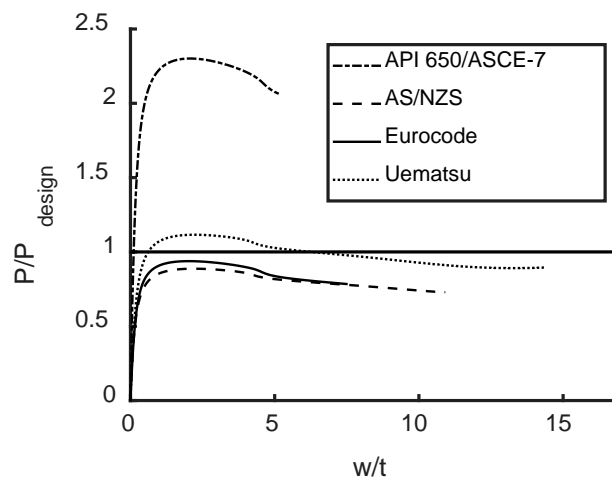
Figure 3-11. The GNIA results for Tank D subjected to the wind loading using different wind profiles with an imperfection amplitude of 0.1t. The horizontal solid line represents design wind pressure.
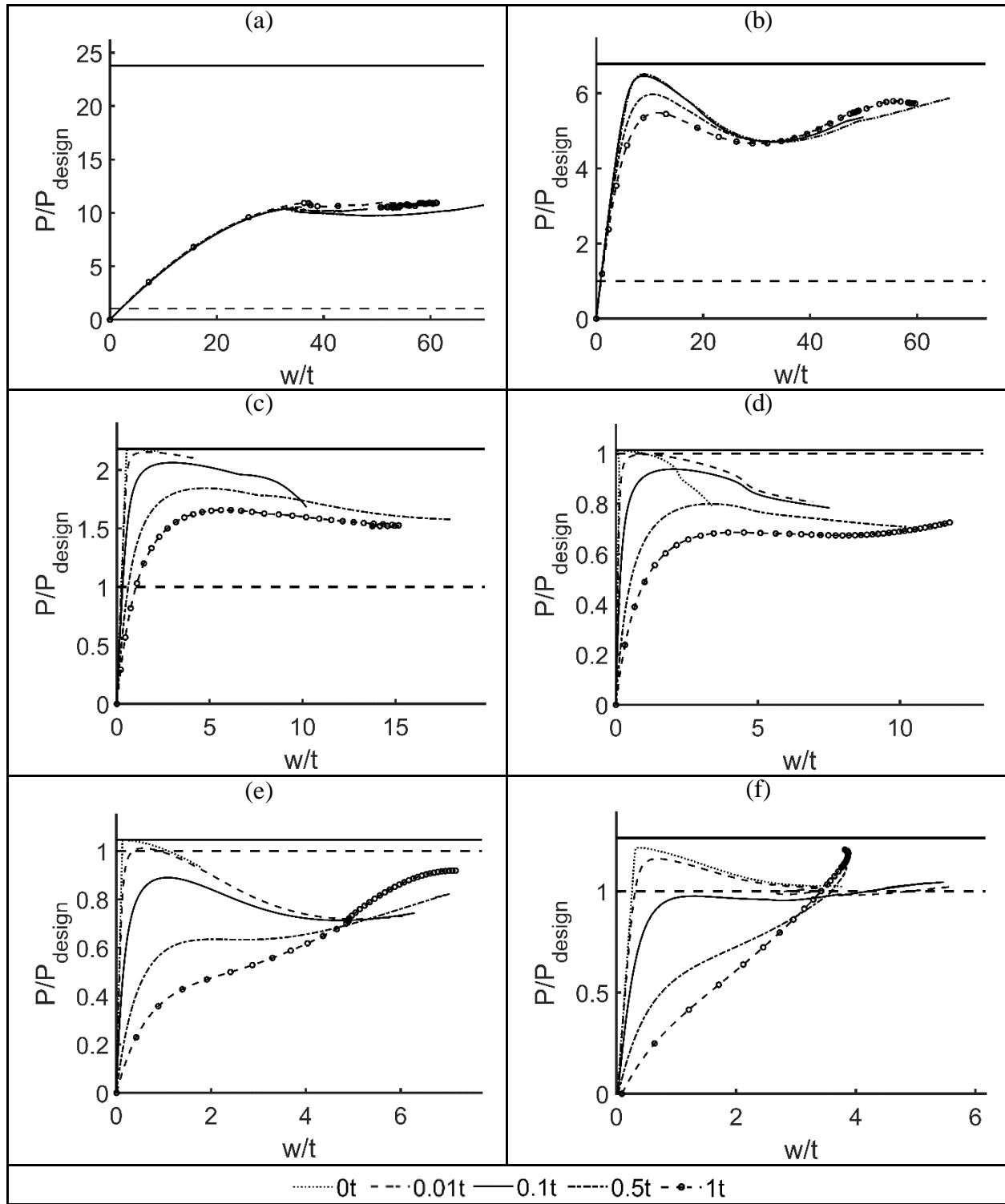
Figure 3-12. The GNIA results for the tanks subjected to wind loading utilizing the Eurocode wind profile with different imperfection amplitudes. A Horizontal solid line represents LBA buckling capacity, and a horizontal dotted line represents design wind pressure. (a) Tank A, (b) Tank B, (c) Tank C, (d) Tank D, (e) Tank E, (f) Tank F.

See copyright note in the next page.
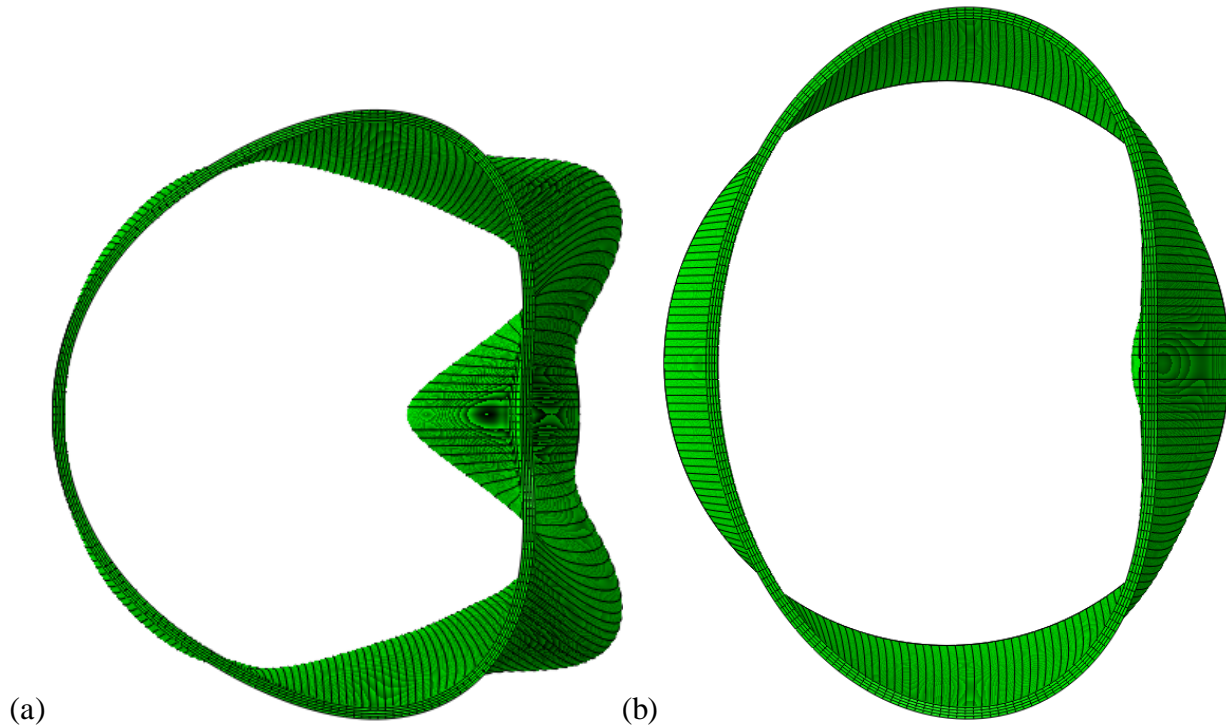
Figure 3-13. (a) The top view of the first mode shape of Tank A obtained from the LBA. (b) The deflected shape of Tank A with a 0.1t imperfection amplitude right after the onset of buckling obtained by the postbuckling analysis. (The deformation is scaled up three times.)

This figure is originally presented in Y.-C. Chiang and S. Guzey, "Influence of Internal Inward Pressure on Stability of Open-Top Aboveground Steel Tanks Subjected to Wind Loading," *Journal of Pressure Vessel Technology,* vol. 141, no. 3, p. 031204, 2019. Reproduction of the figure has been permitted by ASME. The author would like to acknowledge ASME for granting the permission.
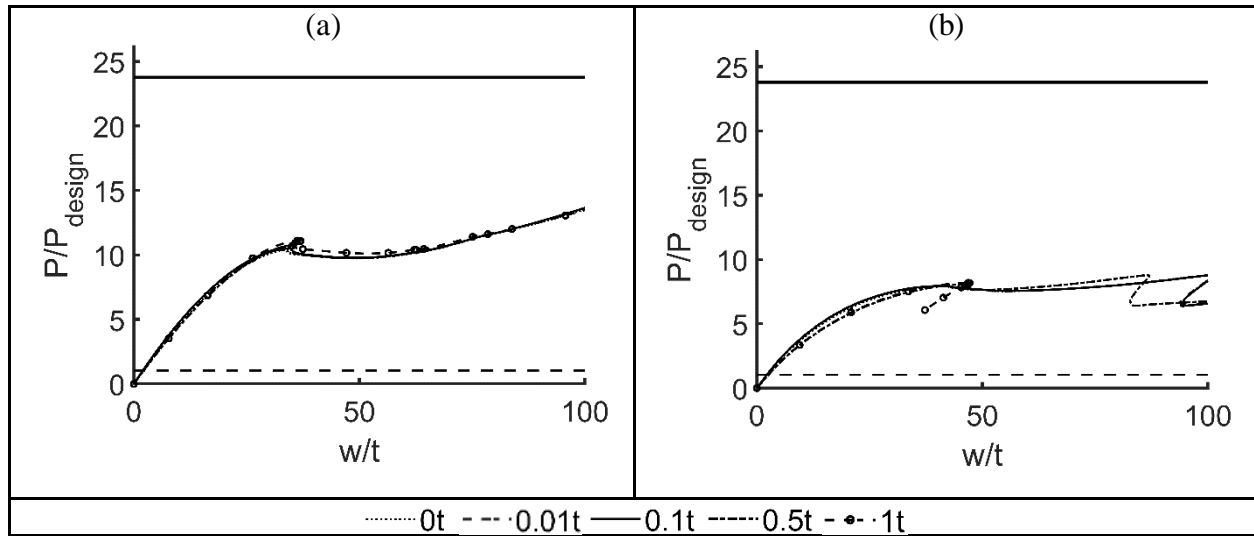
Figure 3-14. The postbuckling analysis with and without material plasticity for Tank A subjected to the wind loading produced by the Eurocode wind profile with different imperfection amplitudes. A horizontal solid line represents the LBA buckling capacity, and a horizontal dotted line represents the design wind pressure. (a) Without material plasticity. (b) With material plasticity.

This figure is originally presented in Y.-C. Chiang and S. Guzey, "Influence of Internal Inward Pressure on Stability of Open-Top Aboveground Steel Tanks Subjected to Wind Loading," *Journal of Pressure Vessel Technology,* vol. 141, no. 3, p. 031204, 2019. Reproduction of the figure has been permitted by ASME. The author would like to acknowledge ASME for granting the permission.
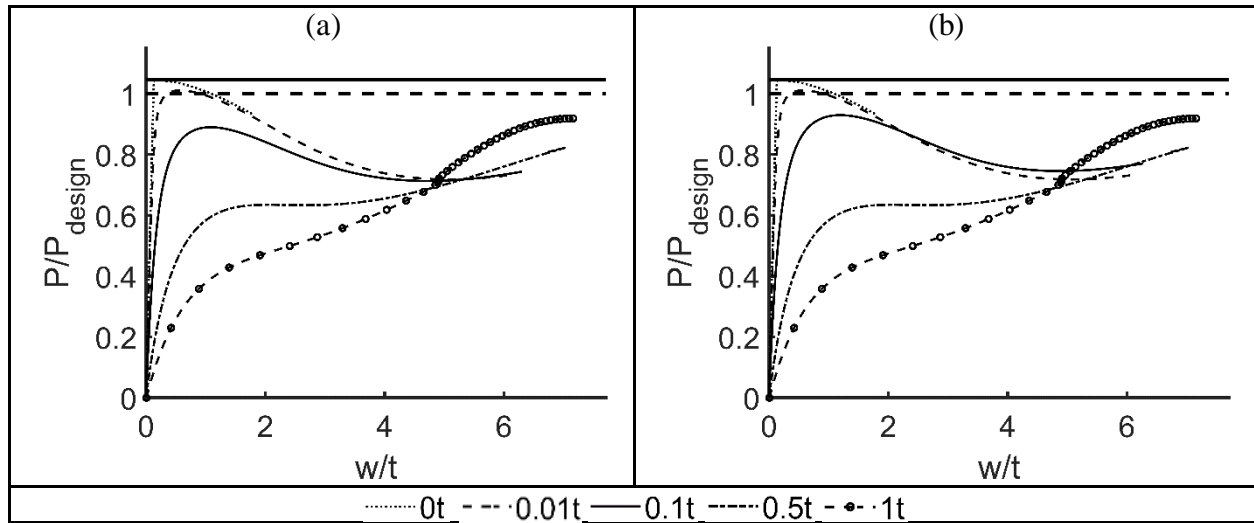
Figure 3-15. The postbuckling analysis with and without material plasticity for Tank E subjected to the wind loading produced by the Eurocode wind profile with different imperfection amplitudes. A horizontal solid line represents the LBA buckling capacity, and a horizontal dotted line represents the design wind pressure. (a) Without material plasticity. (b) With material plasticity.
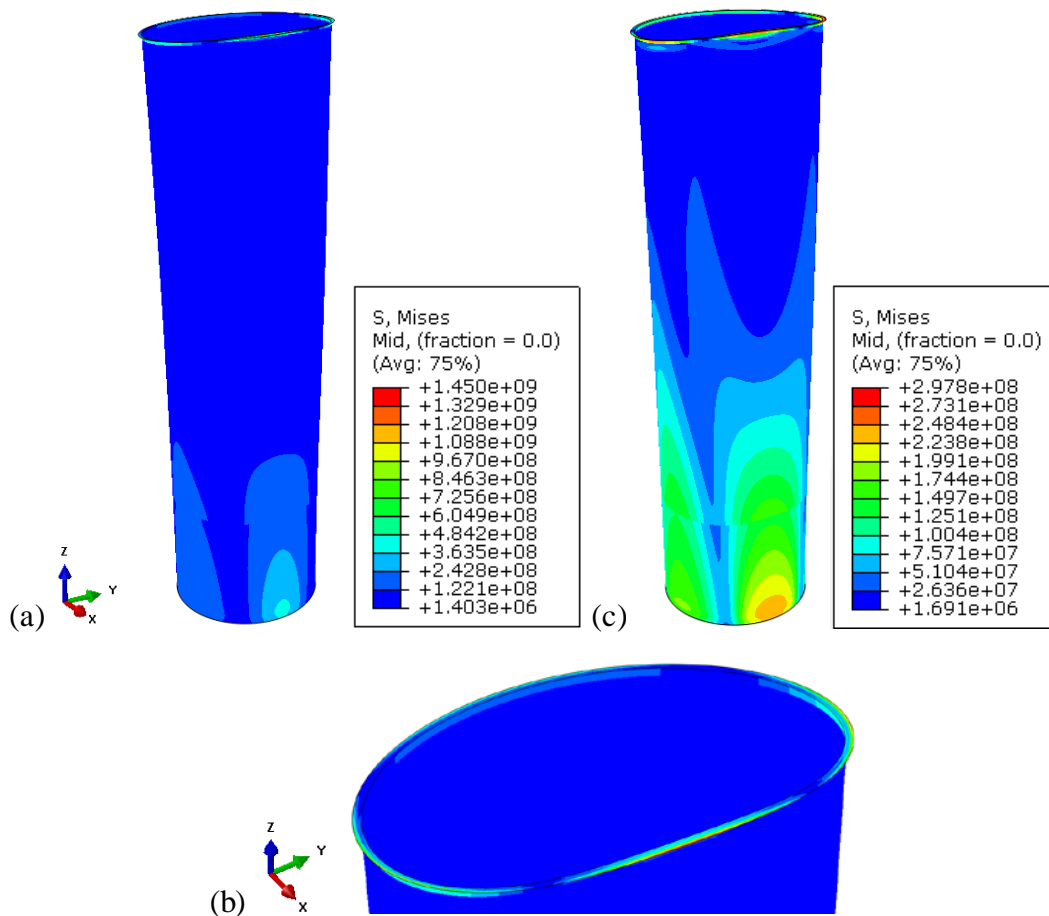
Figure 3-16. The deflected shape of Tank A subjected to the wind loading produced by the Eurocode wind profile. (a) The deflected shape of Tank A without material plasticity applied, at a maximum displacement of 17 cm. (b) A zoomed-in view of subfigure (a). (c) The deflected shape of Tank A with material plasticity applied at a maximum displacement of 17cm. The displacement in all three subfigure is scaled up three times.
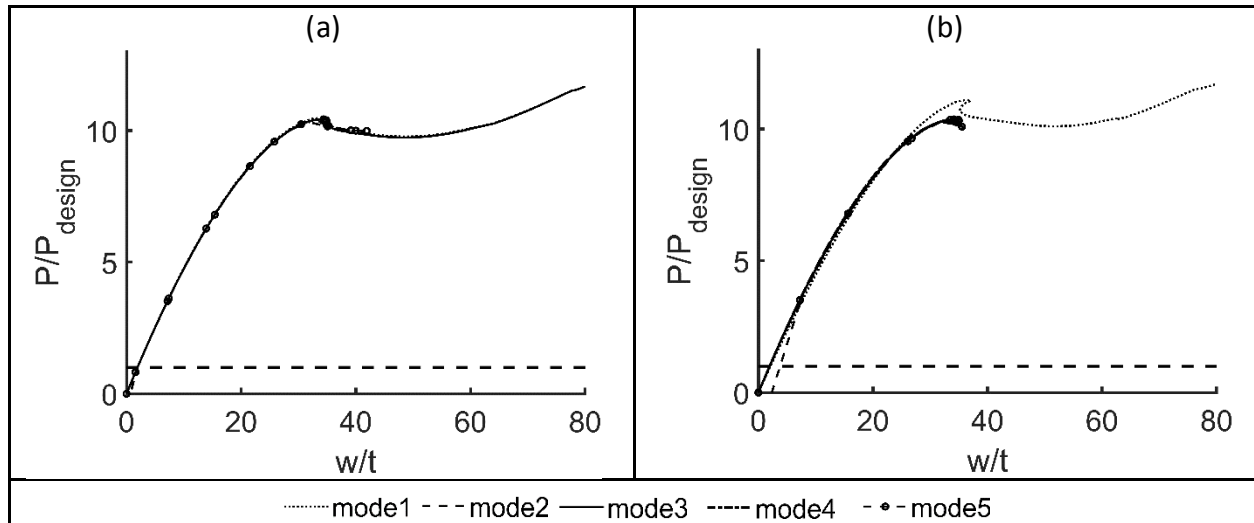
Figure 3-17. The postbuckling analysis of Tank A subjected to the wind loading produced by the Eurocode wind profile with different imperfection geometries. A horizontal dashed line represents design wind pressure. (a) Imperfection amplitude of 0.1*t*. (b) Imperfection amplitude of 1*t*.

This figure is originally presented in Y.-C. Chiang and S. Guzey, "Influence of Internal Inward Pressure on Stability of Open-Top Aboveground Steel Tanks Subjected to Wind Loading," *Journal of Pressure Vessel Technology,* vol. 141, no. 3, p. 031204, 2019. Reproduction of the figure has been permitted by ASME. The author would like to acknowledge ASME for granting the permission.
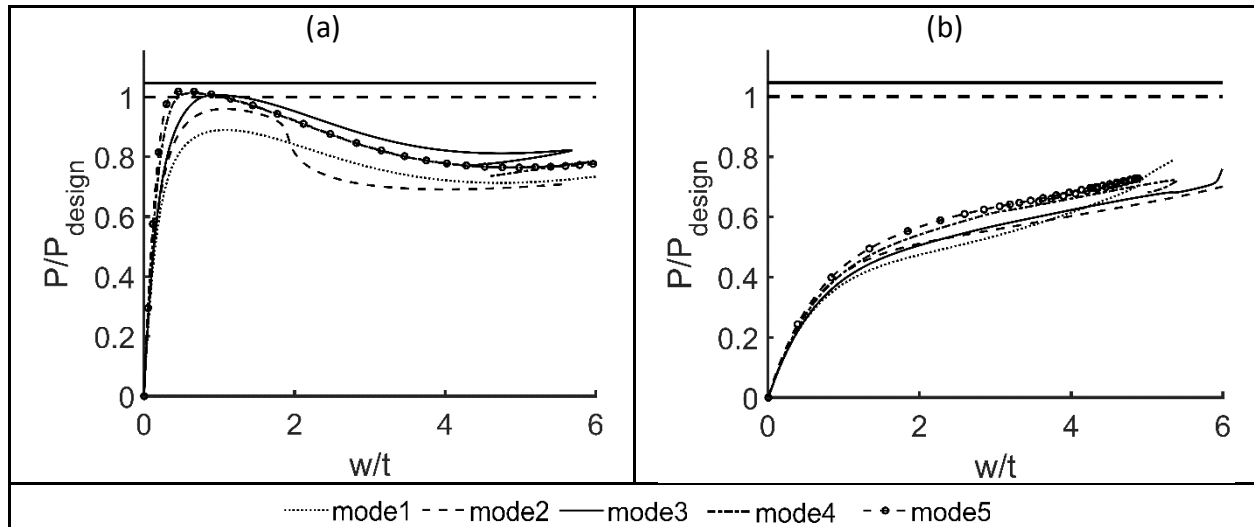
Figure 3-18. The postbuckling analysis of Tank E subjected to the wind loading produced by the Eurocode wind profile with different imperfection geometries. A horizontal dashed line represents design wind pressure. (a) Imperfection amplitude of 0.1*t*. (b) Imperfection amplitude of 1*t*.

This figure is originally presented in Y.-C. Chiang and S. Guzey, "Influence of Internal Inward Pressure on Stability of Open-Top Aboveground Steel Tanks Subjected to Wind Loading," *Journal of Pressure Vessel Technology,* vol. 141, no. 3, p. 031204, 2019. Reproduction of the figure has been permitted by ASME. The author would like to acknowledge ASME for granting the permission.

3.8   References

[1]   L. A. Godoy, "Buckling of vertical oil storage steel tanks: Review of static buckling studies," *Thin-Walled Structures,* vol. 103, pp. 1-21, 2016.

[2]   A. Zingoni, "Liquid-containment shells of revolution: a review of recent studies on strength, stability and dynamics," *Thin-Walled Structures,* vol. 87, pp. 102-114, 2015.

[3]   L. Zick and R. McGrath, "Design of Large Diameter Cylindrical Shells," *Proceedings— API Division of Refining, American Petroleum Institute, New York,* vol. 48, pp. 1114-1140, 1968.

[4]   API, *Welded Tanks for Oil Storage*. Washington, DC. API Standard No.650: American Petroleum Institue, 2013.

[5]   E. Azzuni and S. Guzey, "Comparison of the shell design methods for cylindrical liquid storage tanks," *Engineering Structures,* vol. 101, pp. 621-630, 2015.

[6]   E. Azzuni and S. Guzey, "Failure Modes of API 12F Tanks with a Rectangular Cleanout and Stepped Shell Design," *Journal of Pressure Vessel Technology*, vol. 140 no. 6 pp.061203-061203-18, 2018

[7]   A. Rondon and S. Guzey, "Determination of failure pressure modes of the API specification 12F shop-welded, flat-bottom tanks," *Journal of Pressure Vessel Technology,* vol. 139, no. 4, p. 041409, 2017.

[8]   E. M. Sosa and L. A. Godoy, "Nonlinear dynamics of above-ground thin-walled tanks under fluctuating pressures," *Journal of sound and vibration,* vol. 283, no. 1-2, pp. 201-215, 2005.

[9]   R. von Mises, *The critical external pressure of cylindrical tubes*. Navy Yard, Washington DC: US Experimental Model Basin, 1931.

[10]   L. Chen, J. M. Rotter, and C. Doerich, "Buckling of cylindrical shells with stepwise variable wall thickness under uniform external pressure," *Engineering Structures,* vol. 33, no. 12, pp. 3570-3578, 2011.

[11]   L. Chen, J. M. Rotter, and C. Doerich-Stavridis, "Practical calculations for uniform external pressure buckling in cylindrical shells with stepped walls," *Thin-Walled Structrures,* vol. 61, pp. 162-168, 2012.

[12]   S. Aghajari, K. Abedi, and H. Showkati, "Buckling and post-buckling behavior of thin-walled cylindrical steel shells with varying thickness subjected to uniform external pressure," *Thin-Walled Structures,* vol. 44, no. 8, pp. 904-909, 2006.

[13]   M. Rastgar and H. Showkati, "Buckling of cylindrical steel tanks with oblique body imperfection under uniform external pressure," *Journal of Pressure Vessel Technology,* vol. 139, no. 6, p. 061203, 2017.

[14]   Y. Ding, J. Liu, Z. Chen, F. Qiu, and Q. Lu, "Calculating Failure Pressure Under Different Failure Modes in the Roof-to-Shell of a Vaulted Tank," *Journal of Pressure Vessel Technology,* vol. 139, no. 4, p. 041201, 2017.

[15]   A. R. Shokrzadeh and M. R. Sohrabi, "Buckling of ground based steel tanks subjected to wind and vacuum pressures considering uniform internal and external corrosion," *Thin-Walled Structures,* vol. 108, pp. 333-350, 2016.

[16]   J. Spritzer and S. Guzey, "Nonlinear numerical evaluation of large open-top aboveground steel welded liquid storage tanks excited by seismic loads," *Thin-Walled Structures,* vol. 119, pp. 662-676, 2017.

[17]   M. Haroun and G. Housner, "Earthquake response of deformable liquid storage tanks," *Journal of Applied Mechanics,* vol. 48, no. 2, pp. 411-418, 1981.

[18]   M. A. Haroun and G. W. Housner, "Seismic design of liquid storage tanks," *Journal of the Technical Councils of ASCE,* vol. 107, no. 1, pp. 191-207, 1981.

[19]   P. K. Malhotra, "Seismic response of soil-supported unanchored liquid-storage tanks," *Journal of Structural Engineering,* vol. 123, no. 4, pp. 440-450, 1997.

[20]   L. S. Jacobsen, "Impulsive hydrodynamics of fluid inside a cylindrical tank and of fluid surrounding a cylindrical pier," *Bulletin of the Seismological Society of America,* vol. 39, no. 3, pp. 189-204, 1949.

[21]   M. E. Kalogerakou, C. A. Maniatakis, C. C. Spyrakos, and P. N. Psarropoulos, "Seismic response of liquid-containing tanks with emphasis on the hydrodynamic response and near-fault phenomena," *Engineering Structures,* vol. 153, pp. 383-403, 2017.

[22]   K. K. Mandal and D. Maity, "Nonlinear finite element analysis of elastic water storage tanks," *Engineering Structures,* vol. 99, pp. 666-676, 2015.

[23] M. Vathi, S. A. Karamanos, I. A. Kapogiannis, and K. V. Spiliopoulos, "Performance criteria for liquid storage tanks and piping systems subjected to seismic loading," *Journal of Pressure Vessel Technology,* vol. 139, no. 5, p. 051801, 2017.

[24] K. Bakalis, M. Fragiadakis, and D. Vamvatsikos, "Surrogate modeling for the seismic performance assessment of liquid storage tanks," *Journal of Structural Engineering,* vol. 143, no. 4, p. 04016199, 2016.

[25] S. K. Saha, K. Sepahvand, V. A. Matsagar, A. K. Jain, and S. Marburg, "Fragility analysis of base-isolated liquid storage tanks under random sinusoidal base excitation using generalized polynomial chaos expansion–based simulation," *Journal of Structural Engineering,* vol. 142, no. 10, p. 04016059, 2016.

[26] A. Kanyilmaz and C. A. Castiglioni, "Reducing the seismic vulnerability of existing elevated silos by means of base isolation devices," *Engineering Structures,* vol. 143, pp. 477-497, 2017.

[27] M. Sobhan, F. Rofooei, and N. K. Attari, "Buckling behavior of the anchored steel tanks under horizontal and vertical ground motions using static pushover and incremental dynamic analyses," *Thin-Walled Structures,* vol. 112, pp. 173-183, 2017.

[28] J.-G. Gong, Z.-Q. Zhou, and F.-Z. Xuan, "Buckling strength of cylindrical steel tanks under measured differential settlement: Harmonic components needed for consideration and its effect," *Thin-Walled Structures,* vol. 119, pp. 345-355, 2017.

[29] D. Pantousa, "Numerical study on thermal buckling of empty thin-walled steel tanks under multiple pool-fire scenarios," *Thin-Walled Structures,* vol. 131, pp. 577-594, 2018.

[30] I. Sabransky and W. Melbourne, "Design pressure distribution on circular silos with conical roofs," *Journal of Wind Engineering and Industrial Aerodynamics,* vol. 26, no. 1, pp. 65-84, 1987.

[31] P. Macdonald, K. Kwok, and J. Holmes, "Wind loads on circular storage bins, silos and tanks: I. Point pressure measurements on isolated structures," *Journal of Wind Engineering and Industrial Aerodynamics,* vol. 31, no. 2-3, pp. 165-187, 1988.

[32] X. Hua and C. Letchford, "A comparison of wind loads on circular bins, silos and tanks," in *Structures Congress 2014*, Boston, Massachusetts, 2014, pp. 1616-1629: ASCE.

[33] Joint Standards Australia/Standard New Zealand Standard, *AS/NZS 1170.2: 2011 Structural design actions-Part 2: Wind actions*. Sydney, NSW, Australia, 2011.

[34]   American Society of Civil Engineers, *ASCE-7-16: Minimum Design Loads for Building and other Structures*. Reston, VA.: ASCE-7-16, 2016.

[35]   G. Portela and L. A. Godoy, "Wind pressures and buckling of cylindrical steel tanks with a conical roof," *Journal of Constructional Steel Research,* vol. 61, no. 6, pp. 786-807, 2005.

[36]   G. Portela and L. A. Godoy, "Wind pressures and buckling of cylindrical steel tanks with a dome roof," *Journal of Constructional Steel Research,* vol. 61, no. 6, pp. 808-824, 2005.

[37]   J. Yasunaga and Y. Uematsu, "Dynamic Buckling of Cylindrical Storage Tanks under Fluctuating Wind Forces," (in Japanese), *Journal of Wind Engineering,* vol. 43, no. 2, 2018.

[38]   C. Iamandi, A. Georgescu, and C. Erbasu, "Experimental modelling of four steel tanks battery," in *Eleventh International Conference on Wind Engineering*, Lubbock, TX, 2003, pp. pp. 1243-1250.: Wind Science and Engineering Research Center at Texas Tech University.

[39]   AWWA, *Standard Specifications for Elevated Steel Water Tanks, Standpipes and Reservoirs*. Denver, CO: American Water Work Association, 1935, pp. 1606-1625.

[40]   E. Azzuni and S. Guzey, "Stability of open top cylindrical steel storage tanks: Design of top wind girder," *Journal of Pressure Vessel Technology,* vol. 139, no. 3, p. 031207, 2017.

[41]   T. Sun, E. Azzuni, and S. Guzey, "Stability of Open-Topped Storage Tanks With Top Stiffener and One Intermediate Stiffener Subject to Wind Loading," *Journal of Pressure Vessel Technology,* vol. 140, no. 1, p. 011204, 2018.

[42]   E. Azzuni and S. Guzey, "A perturbation approach on buckling and postbuckling of circular rings under nonuniform loads," *International Journal of Mechanical Sciences,* vol. 137, pp. 86-95, 2018.

[43]   R. V. McGrath, "Stability of API standard 650 tank shells," in *28th Midyear meeting of the American Petroleum Institute's division of refining*, Brooklyn, N.Y., 1963: American Petroleum Institute.

[44]   F. Bu and C. Qian, "A rational design approach of intermediate wind girders on large storage tanks," *Thin-Walled Structures,* vol. 92, pp. 76-81, 2015.

[45] F. Bu and C. Qian, "On the rational design of the top wind girder of large storage tanks," *Thin-Walled Structures,* vol. 99, pp. 91-96, 2016.

[46] J. H. Adams, "A study of wind girder requirements for large API 650 floating roof tanks.," in *API, Refining 40th Midyear Meeting,* Chicago, IL: American Petroleum Institute, 1975, pp. 16-75.

[47] Y. Uematsu, T. Yamaguchi, and J. Yasunaga, "Effects of wind girders on the buckling of open-topped storage tanks under quasi-static wind loading," *Thin-Walled Structures,* vol. 124, pp. 1-12, 2018.

[48] J. Yasunaga and Y. Uematus, "Buckling and Dynamic Behavior of Open-topped Oil-storage Tanks under Wind Loading," (in Japanese), *Journal of Wind Engineering,* vol. 38, no. 2, pp. 179-180, 2013.

[49] F. G. Flores and L. A. Godoy, "Forced vibrations of silos leading to buckling," *Journal of Sound and Vibration,* vol. 224, no. 3, pp. 431-454, 1999.

[50] R. Greiner and P. Derler, "Effect of imperfections on wind-loaded cylindrical shells," *Thin-Walled Structures,* vol. 23, no. 1-4, pp. 271-281, 1995.

[51] L. A. Godoy and F. G. Flores, "Imperfection sensitivity to elastic buckling of wind loaded open cylindrical tanks," *Structural Engineering and Mechanics,* vol. 13, no. 5, pp. 533-542, 2002.

[52] Y. Zhao and Y. Lin, "Buckling of cylindrical open-topped steel tanks under wind load," *Thin-Walled Structures,* vol. 79, pp. 83-94, 2014.

[53] Q. S. Cao, Y. Zhao, and R. Zhang, "Wind induced buckling of large circular steel silos with various slenderness," *Thin-Walled Structures,* vol. 130, pp. 101-113, 2018.

[54] A. R. Shokrzadeh and M. R. Sohrabi, "Strengthening effects of spiral stairway on the buckling behavior of metal tanks under wind and vacuum pressures," *Thin-Walled Structures,* vol. 106, pp. 437-447, 2016.

[55] European Committee for Standardisation, *Eurocode 3: Design of Steel Structures, Part 4.1: Silos*. Brussels, Belgium.: Standard No. EN 1993-4-1, 2007.

[56] Y. Uematsu, C. Koo, and J. Yasunaga, "Design wind force coefficients for open-topped oil storage tanks focusing on the wind-induced buckling," *Journal of Wind Engineering and Industrial Aerodynamics,* vol. 130, pp. 16-29, 2014.

[57]   ABAQUS, *ABAQUS Analysis User's Manual version 2018*. Providence, RI: Dassault Systèmes SIMULIA, 2018.

[58]   ASME Boiler and Pressure Vessel Code, *Section II. Materials*. New York, NY: American Society of Mechanical Engineers 2015.

[59]   ASME Boiler and Pressure Vessel Code, *Section VIII. Alternative Rules for Construction of Pressure Vessels, Division 2* New York, NY: American Society of Mechanical Engineers 2015.

[60]   C. Maraveas, G. A. Balokas, and K. D. Tsavdaridis, "Numerical evaluation on shell buckling of empty thin-walled steel tanks under wind load according to current American and European design codes," *Thin-Walled Structures,* vol. 95, pp. 152-160, 2015.

4. APPLICATION OF COMPUTATIONAL FLUID DYNAMICS ON CLOSE-TOP TANKS UNDER WIND LOADING

4.1 Introduction

Aboveground storage tanks have been used in wide variety of industries such as petroleum and chemical industries to store liquid. To make these tanks cost efficient, the shell thickness of such tanks are designed to be very slender [1, 2], and thus have been recognized to be prone to buckling [3, 4]. Buckling of a tank shell can be induced by different kinds of events, such as internal vacuums [5-8] and seismic events [9-11], and both of the events have been extensively studied. When the tanks are empty, wind gusts can induce buckling and cause drastic damage on tanks, and, thus, such buckling behavior has garnered much research [8, 12-17].

Before studying the buckling behavior of a tank subjected to wind loading, however, it is essential to understand how wind gusts interact with tanks. Researchers have extensively conducted boundary layer wind tunnel tests (BLWT) to investigate the wind pressure distribution on tanks subjected to wind gusts. Research conducted by Sabransky and Melbourne [18] and MacDonald et al. [19] are known to be the early experiments undertaken with high Reynolds numbers. According to Hua and Letchford [20], these two studies are the basis of AS/NZS 1170.2:2011 [21] and ASCE-7 [22]. Sabransky and Melbourne [18] studied silos with conical roofs and the height (H) to diameter (D) ratios of the silos ranged from 0.66 to 1.16. Additionally, valuable comparison between the result of the wind tunnel test and results from a full scale measurement [23] was presented. Later, MacDonald et al. [19] examined silos with aspect ratios (H/D) from 0.5 to 2 with different roof configurations. They proposed that the pressure distribution on the shell is independent of the Reynolds number if the Reynolds number at the height of the shell is greater than 1×10^5. Also, a relatively large internal inward pressure on an open-top silo was observed in the research [19]. Specifically, the magnitude of this internal pressure almost double the wind pressure on the windward stagnation point of open-top silos. This internal pressure, however, is not reflected in the current North American design documents including ASCE-7 [22] and API 650 [1]. Recently, a thorough study has been conducted to investigate the impact of such internal pressure on the stability of tanks [17]. Through finite element analysis, it was shown that the

buckling capacity of a tank may drop over 50%, indicating this is not a factor that is negligible during design.

In terms of BLWT in the literature, Uematsu and Koo [24] were interested in the pressure distribution on the flat roofs of tanks with aspect ratios from 0.5 to 3. Reynolds number independence study was conducted utilizing tanks with flat roofs. They concluded that the pressure coefficient is independent of Reynolds number as the Reynolds number exceeds 0.8×10^5. This observation matched the what MacDonald et al. [19] reported. The pressure distribution on flat roofs and the internal pressure on open-top tanks were studied. While the magnitude of the internal pressure coefficient observed by Uematsu and Koo [24] was smaller than what MacDonald et al. [19] recorded, the overall phenomenon was similar. Burgos et al. [25] aimed to study shielding effect of grouped conical roof tanks. Since the wind flow is obstructed if multiple structures are located closely, it was reported that the wind pressure distribution varied substantially due to the configuration of the tanks. Other researches employing BLWT includes studies by Zhao et al. [26], Matsui et al. [27], Portela and Godoy [28, 29].

Despite the rich literature employing BLWT, research based on computational fluid dynamics (CFD) as an alternative to obtain the wind pressure distribution on storage tank is almost not available. Indeed, as an experiment, BLWT shall be capable to reflect the actual interaction between wind gusts and structures. However, a wind tunnel facility is required for a BLWT test, and it may not be available at every research institute. In contrast, contemporary desktop computers are usually able to run steady CFD analysis without consuming excessive amount of time. Thus, CFD is likely a more cost efficient approach to obtain the wind pressure distribution of a tank. Research by Iamandi et al. [30] is the only study on wind distribution of tanks utilizing CFD to the author's best knowledge. Iamandi et al. [30] performed both CFD and BLWT, and concluded that the wind pressure distribution obtained from both method were aligned with each other. However, only very limited details about the CFD study was provided in the paper. Information including but not limited to tank geometry (height and pitch), computational domain size, grid size, and boundary conditions was not reported. Furthermore, there was a 25% difference between the measured pressure in BLWT and CFD, which should not be considered to be a small difference.

In contrast, CFD has been widely adopted in other research fields related to wind engineering. For instance, Blocken et al. [31] conducted a research on how the configuration of a peloton of cyclist affects the drag force on individual cyclist. The reduction of the drag (down to $5 - 10\%$) coefficient due to shielding effect on riders in the mid rear of the peloton observed indicated that the reduction of drag coefficient reported by previous studies ($50 - 70\%$) may not base on right assumptions. Kim et al.[32] focused on the wind pressure acting on multi-span green houses. A thorough insight of the effect of different turbulence models, domain size, first cell height, and grid size were provided. The results were compared to the pressure distribution obtained from BLWT to ensure the selected parameters properly reflects the reality.

Mochida et al. [33] conducted a cooperative project with Architectural Institute of Japan (AIJ), to provide guideline for practical CFD application to high-rise buildings. Simulations were performed by nine different affiliations, with same computational conditions, including grid arrangement and domain size. Different turbulence models were applied in this project, and difference between results obtained through different turbulence models were remarkable. For instance, the wind reattachment length predicted by different research groups had a difference up to 30% under identical set up. It was also noted that the standard k-ε model was not able to capture the reverse flow on the roof of the modeled buildings. Montoya et al. [34] present a fully numerical strategy as an alternative for the traditional iterative process in bridge deck design. Two cable-stayed bridge were investigated using a multidisciplinary method, which is an integration of CFD, surrogate modeling, quasi-steady aeroelastic formulation and multi-modeflutter analyses. The established numerical procedure reveals areoelastic effect on a bridge. To assess the viability of natural ventilation for preliminary building design, Cheng et al. [35] carried out CFD analyses with typical building geometries. A map of the natural ventilation potential across the North America was proposed. As an example, it was indicated that a four-story rectangular building located in Toronto would gain the most energy saving by using a southwest facing single sided natural ventilation.

CFD as a tool, however, needs to be applied with thorough understanding of the input parameters and the theories hidden by the commercial software. Franke et al. [36] provided a detailed instruction for application of CFD in wind engineering. It was suggested that standard k-ε model

should not be used in the simulation for wind engineering problems. Other parameters, such as domain size, boundary conditions, and grid resolution were also discussed. Moreover, the analysis convergence criteria, indicating that the final residual compared to the residual after the first iteration should drop at least five orders, was proposed. Similarly, Tominaga et al. [37] published another CFD guideline, representing the Working Group of AIJ. An extensive cross comparison of result obtained from BLWT and CFD was presented. Difference between these two guideline includes recommended domain size, representation of surroundings when applying CFD to urban areas, criteria of evaluating convergence, and boundary conditions. Recommendations by Franke et al. [36] and Tominaga et al. [37], if applicable, were adopted in this study and specific details will be discussed in the following sections.

Hargreaves and Wright [38] indicated that with wall function embedded in the commercial CFD codes, the inlet velocity and turbulence profile cannot be maintained in a fluid domain even without obstacle. This is a result of users only adopting a subset of the boundary condition proposed by Richards and Hoxey [39]. It was stated that complex modifications might be needed to make inlet profile sustain through the length of a fetch. To enforce the correct Reynolds stress, Cindori et al.[40] introduced an additional wind-source term to the momentum equation. Their result showed that the mean velocity, Reynold stresses and turbulent kinetic energy profile remain almost homogeneous along the computational domain, with a maximum discrepancy of 0.6%.

Recently, Thordal et al. [41] reviewed critical input parameters for conducting CFD and focused on evaluation of the design wind load of high-rise buildings. Thordal et al. [41] also pointed out that CFD guidelines associated with Reynolds-averaged Navier-Stokes (RANS) turbulence model are available, but guideline for large eddy simulation (LES) is still being needed, and this research gap is desired to be filled in the future. Aware of that the k-ε turbulence models not being able to accurately predict the reattachment length when a gust of wind passing through a building, Shirzadi et al. [42] tried to adapt the empirical parameters that are widely adopted by the commercial CFD codes to fit the experimental results. Specifically, semi-empirical coefficients, including C_μ, $C_{\epsilon1}$, and $C_{\epsilon2}$, were adjusted. It was suggested that this set of optimized coefficient significantly improved the accuracy of the turbulence model in terms of predicting velocity, turbulence kinetic energy and temperature distribution around a building.

The present study aims to investigate how CFD analysis can be applied to obtain the wind pressure coefficient of tanks, as there is barely any study available currently though it has been a common type of analysis in other research fields. As no detailed study, this paper started with a review on the theory and background knowledge of CFD. Then, analyses using a commercial CFD code, Ansys FLUENT [43], were conducted. To apply CFD to tanks, an elaborated grid dependence study on a tank with an *H* to *D* ratio of 0.5 and a flat roof was carried out. Mesh strategies for determining a converged grid discretization, and the size of the computational domain were proposed. To ensure the validity of the selected model and input parameters, available literatures, including research by MacDonald et al. [19, 24] were used as reference solutions. Once the grid discretization strategies were determined, tanks with aspect ratios ranging from 0.4 to 2 were analyzed. These tanks include tanks with flat roof, conical roof, and dome roof, and published results [19, 28, 29] were again used as reference solutions. With the obtained results, the effect of aspect ratio and the roof configuration on the pressure distribution on tank shell were presented. The pressure distribution on the tank roofs were discussed.

4.2   CFD Analysis Implementation and Set-up for Parametric Study

To accurately conduct CFD for estimating the pressure distribution, discussion about the input parameters, including turbulence model, boundary conditions, and mesh strategies, were selected and presented in this section.

4.2.1   Adopted Turbulence Models

Due to the nature of high Reynolds number of flow of interest, the flow condition is considered to be turbulent flow. To properly capture the characteristic of the flow, turbulence of the flow needs to be modeled with care. Turbulence models adopted in this study are based on RANS approach since the RANS models are the generally employed models, and extensive guidelines as how to handle the input parameters are available.

In RANS models, the instantaneous Navier-Stoke equation is separated into two terms, mean and fluctuating terms as shown in Eqn. (32).

$$\varphi = \bar{\varphi} + \varphi' \tag{32}$$

Here, φ can be scalar quantities such as velocity in a certain direction, pressure, or energy. Accordingly, $\bar{\varphi}$ will be the time-averaged term of the scalar, and φ' will be the fluctuation term of the scalar at a certain instant. By dropping the latter term in Eqn. (32), and substitute the time-averaged velocity into continuity and momentum equations, the time averaged solution can be obtained. Continuity and momentum equation, which are the governing differential equations for an incompressible flow, can be written as Eqn. (33) and Eqn. (34), respectively.

$$\nabla \cdot (\rho \vec{u}) = 0 \tag{33}$$

$$\frac{\partial}{\partial t}(\rho u_i) + \frac{\partial}{\partial x_j}(\rho u_i u_j) = -\frac{\partial \rho}{\partial x_i} + \frac{\partial}{x_j}\left[\mu\left(\frac{\partial u_i}{\partial x_j} + \frac{\partial u_j}{\partial x_i} - \frac{2}{3}\delta_{ij}\frac{\partial u_j}{\partial x_i}\right)\right] + \frac{\partial}{\partial x_j}(-\rho\overline{u_i'u_j'}) \tag{34}$$

Here, t is time, x_i is the i direction for the coordinate system, u_i represents the velocity in i direction, ρ is the density of air, μ is the dynamic viscosity, δ_{ij} is Kronecker delta, and $-\rho\overline{u_i'u_j'}$ is the Reynolds stress tensor, which were modeled to properly accomplish the closure of these governing differential equations.

To model the turbulence, k-ε and k-ω are two major turbulence models. These two models are the simplest models for which two extra transport equations are introduced to solve the turbulence of the flow. Since no advance property of the turbulence is required for these models to obtain a solution, they are referred to as "complete models" [44]. Thus, k-ε and k-ω models (including available modified models) were examined in this study. Detailed formulation of these two turbulence models can be found in FLUENT Theory Guide [45] and a report by Mulvany et al. [46]. The model constants are remained as their default values for all the turbulence models.

A time-averaged solution rather than a transient solution is reasonable since it is usual to consider a time-averaged pressure to be the design wind loading for structures [47]. The duration for which the pressure is averaged can range from 10 minutes to an hour for a full scale structure. Besides, most of the BLWT researches report the mean distribution profile. Therefore, a time-averaged solution should be able to replicate results that are reasonably close to the mean pressure distribution obtained through BLWT. For near-wall treatment, enhanced wall treatment, which is

a treatment that is insensitive of the dimensionless first cell height, as suggested [45] was applied to simulations adopting k-ε models.

4.2.2 Computational Conditions

As the turbulence model has been selected and discussed, parameters including boundary conditions, computational domain size, and iterative convergence were discussed in this section.

A tank along with the fluid domain is presented in Figure 4-1. The wind flows from $+x$ to $-x$ direction, and the center of the bottom plate of the tank is selected as the origin of the coordinate system. Consequently, the $+x$ region is the upstream region, and $-x$ region is the downstream region. The $+z$ and $-z$ direction is referred to as the lateral directions, and the y direction is referred to as height direction.

In terms of inlet boundary condition, the inlet profile proposed by Richards and Hoxey [39] was adopted. This inlet profile is widely adopted by researchers and is recommended by Franke et al. [36]. This set of boundary condition is composed of the following equations (Eqn. (35) to (38)).

$$u(y) = \frac{u^*}{\kappa} \ln \left(\frac{y + y_0}{y_0} \right) \tag{35}$$

$$k = \frac{(u^*)^2}{\sqrt{C_\mu}} \tag{36}$$

$$\varepsilon = \frac{(u^*)^2}{\kappa(y + y_0)} \tag{37}$$

$$\omega = \frac{\varepsilon}{C_\mu k} \tag{38}$$

Here, u is the streamwise velocity, u^* is the friction velocity, κ is von Karman's constant (approximately 0.41), C_μ is a model fitting parameter, y_0 is the surface roughness length, y is the height for which the velocity is considered, k is the turbulence kinetic energy, ε is turbulence dissipation rate, and ω is specific dissipation rate. To replicate wind tunnel test results, a y_0 of 0.002 m specified by MacDonald et al. [19], in their wind tunnel test was employed.

Reynolds number of the flow was selected such that the analysis results can be aligned with the available BLWT results. Reynolds number for a cylinder is defined as Eqn. (39)

$$Re = \frac{u_H D}{\nu} \tag{39}$$

where u_H is the velocity (m/s) at the shell height of a tank (height excluding the roof), and ν is the kinematic viscosity of air (1.8×10^{-5} m^2/s). To ensure a relatively high Reynolds number (exceeding 1×10^5), a u_H of 14 m/s was selected as all the tanks adopted in this study have a diameter of roughly 0.2 m, and this velocity corresponds to a Reynolds number of 1.5×10^5. With the determined velocity at the reference height, u^* can be calculated using Eqn. (35). The corresponding u^* is 0.92 m/s if a tank has a shell height of 0.1 m. The boundary conditions on the lateral and top surfaces of the domain were set to be symmetry boundary condition, such that no unnecessary velocity gradient would be generated at these surfaces. The outlet surface was a free surface.

The dimension of the computational domain in terms of the upstream length, lateral width, and the height follows the recommendation of by Franke et al.[36] and Tominaga et al. [37], in which both of them suggested these dimensions to be at least 5H. The suggested downstream length of the domain by Franke et al. [36] and Tominaga et al. [37], however, do not agree with each other. Thus, a parametric study was conducted to determine a suitable downstream length of the domain.

In terms of solution convergence, Franke et al. [36] suggested that the residual, normalized with the residual after first iteration, shall drop five order to ensure the convergence of the result. To eliminate the iterative error, have the normalized residual to be less than 10^{-12} is favorable. However, as Tominaga et al. [37] mentioned, the residual dependents on various parameters, and there is probably not a universal guideline. The author observed a larger normalized residual magnitude compare to recommendation made by Franke et al. [36]. To ensure the analysis is converged, the residual was monitored. Based on several trials, it was found that if there is no substantial change in the magnitude of the normalized residual in a thousand iterations, the residual is not likely to drop any further. Thus, this is considered to be the convergence criteria in the present study.

Double precision as suggested by Franke et al. [36] was adopted. A pressure-based solver is employed, with a pressure-velocity coupling algorithm, SIMPLE algorithm.

4.2.3 Mesh Strategy

The solution of a CFD analysis heavily depends on the grid discretization, and therefore the mesh strategies were hereby discussed. The construction of the grid was composed of several strategies and grid independence studies based on the proposed strategies were conducted in the following sections. First, as suggested by Tominaga et al. 2008 [37], the first ten cells adjcent to the wall (tank shell) were made to be prismatic cells, and the thickness of such cell was referred to as first cell height. The growth ratio, which dictates the relative cell edge length of two adjacent cells, of the first cell height was set to be 1.2. Second, to have a good mesh resolution on the tank shell and roof, the grid size on the tank shell and roof was also stuided. Third, the grid on the bottom surface of the fuild domain was set to be finer than other surfaces to capture the large velocity gradient at the lower portion of the height of a wind tunnel. The growth ratio of the second and third meshing strategies were 1.1 such that a good resolution in the near wall region can be ensured. These three parameters, namely first cell height, grid size on tank faces and grid size on the bottom surface were investigated in the following sections to obtain a grid independent solution.

4.2.4 Standard Test Cases for Parametric Study

To study the mentioned parameters, including grid independence, turbulence model, and downstream length of the domain, a standard test case was defined in this section. Since the objective of this study is to calibrate CFD with BLWT results, a tank tested by MacDonald et al. [19], with diameter of 0.2 m and height of 0.1 m and a flat roof, was adopted. The corresponding fluid domain size was 0.5 m ($5H$) in the lateral, top, and upstream directions. In this standard case, a downstream length of 1.5 m ($15H$) was conservatively selected, which followed the recommendation by Franke et al. [36]. For the boundary conditions, refer to section 4.2.2. In this standard set up, RNG k-ε model was selected. The result of realizable k-ε model and standard k-ω model diverged in some of the tests in a preliminary study conducted by the author, and thus was not adopted in this phase.

In terms of the meshing strategy, a first cell height of 0.1 mm, a mesh size on tank faces of 5 mm, and a mesh size on bottom surface of 5 mm were chosen. These grid sizes were based on the result reported by Kim et al. [32], because of the similarity of the studied model. Since [32] obeserved

results closely aligned with the results obtained by BLWT, these grid sizes as a first trial were selected. The maximum grid size of the entire model was 50 mm, to ensure at least 10 cells along the boundary edges. The seleceted parameters are complied in Table 4-1, and the corresponding grid discretization is presented in Figure 4-2.

4.3 Validation of the Input Parameters and Results of the Parametric Study

4.3.1 Notation Definition and Reference Solution

Before the results are presented, the notation adopted in this section was illustrated, and how the analyses results were compared to the reference solution was explained. For the design purpose, the result of BLWT or CFD are usually reported as pressure coefficient, C_p, rather than pressure. C_p can be expressed as Eqn (40).

$$C_p = \frac{p_p - p_\infty}{\frac{1}{2} \rho u_H{}^2} \tag{40}$$

Here, p_p is the pressure at any arbitrary point on a structure, p_∞ is the pressure at a location which is infinitely far from the structure, ρ is the density of the air (1.225 kg/m³), and u_H is the wind velocity at the reference height. In this case, the reference height is 0.1 m (tank shell height) from the bottom of the wind tunnel and the magnitude of u_H is 14 m/s. A positive pressure coefficient stands for a pressure, and a negative pressure coefficient stands for a suction. To better describe the pressure distribution, a cylindrical coordinate system used in the following sections is shown in Figure 4-3. The point with the largest positive pressure coefficient (at $\theta = 0°$) is referred to as stagnation point.

Without detailed wind tunnel test results, the pressure coefficient at the stagnation point ($C_p(0°)$) and the point with minimum pressure coefficient on the tank shell ($C_{p,suc}$), which were easy to read from the published results are chosen for comparing the CFD analysis result and the BLWT results. Results published by MacDonald et al. [19] was adopted as reference solutions. A pressure distribution curve at $y = 62$ mm reported by MacDonald et al. [19] indicated a $C_p(0°)$ of 0.98 and a $C_{p,suc}$ occured at $\theta = 80.6°$, with a magnitude of -1.00. Validation of the CFD analyses were based on these results. Note that the $C_p(0°)$ presented in the following sections were the highest

pressure coefficient along the line of $\theta = 0°$ (windward meridian), rather than the maximum pressure coefficient at $y = 62$ mm. A further discussion on the reasoning is include in section 4.3.2

4.3.2 Comparison of Result from Standard Test Case with Reference solution

Prior to the presentation of the parametric study, the results obtained from the standard test case must be compared with the reference solution (e.g. BLWT results) to ensure the validation of the input parameters (complied in Table 4-1). Apart from $C_p(0°)$ and $C_{p,suc}$, this section would also discuss the pressure distribution on the roof, and the results of the BLWT test carried out by Uematsu and Koo [24] was used as a reference solution. For design purpose, Uematsu and Koo [24] divided a roof of a tank into four regions, and the area-averaged pressure coefficients were reported. A schematic as how the regions were divided is presented in Figure 4-4.

The result of the standard test case along with the reference solution is presented in Table 4-2. It can be observed that the result obtained through the standard test case fairly aligned with the result presented by MacDonald et al. [19]. $C_p(0°)$ occurs at $y = 78$ mm, and the magnitude being 0.92, which represents 6% difference comparing to the reference solution, and this difference is considered acceptable. It seems that the location at where the pressure coefficient is the highest in the CFD simulation is slightly higher than the location at where MacDonald et al. [19] observed the highest pressure. However, it is typical to have the highest pressure coefficient being located in the region of 60% to 90% (60 mm to 90 mm in this case) of the tank height. As the maximum pressure coefficient obtained through CFD falls within this range, and it is not likely for the simulation to perfectly replicate the BLWT test, it was decided to report the highest pressure coefficient along the line of windward meridian.

The $C_{p,suc}$ was well-predicted by the CFD simulation, with the magnitude of -1.00, same as BLWT result. Location where the $C_{p,suc}$ is observed is also very close to the reference solution, 86° for the CFD analysis and 80.6° for the BLWT. The difference of the location where $C_{p,suc}$ is observed may be a result of the grids and the location of the pressure tap placed during the BLWT not being

at the same exact point. Thus, it should be safe to state that the location of $C_{p,suc}$ is being predicted quite accurately.

When the pressure on the roof is being discussed, the averaged pressure coefficient in all regions seem to be close to the reference solutions. The error ranges from 3% to 21%. A source of such discrepancy may be the different inlet wind profile. The inlet velocity profile adopted by Uematsu and Koo [24] followed the power law, and the present study employed an inlet profile based on the logarithm law. This shall not result in a drastic difference, but it still needs to be accounted for. The pressure coefficient in Reigion 3, which is the region with the largest area, was accurately predicted by the CFD simulation. Thus, it shall be safe to state that the CFD simulation is capable of capturing the pressure coefficient on flat roof on a tank.

For the discrepancy in Region 1 and 2, the discrepancy is likely due to some deficiency of k-ε model. As mentioned earlier, Mochida et al. [33] indicated that the reattachement length of the flow on the roof of the buildings they modeled was larger than the reattachment length observed in the BLWT in most of the cases. This is because the sharp corner in the model is a sort of singular point in CFD [48], and k-ε models is not to model the turbulence kinetic energy at the sharp corner properly. No matter how fine the grid is, this problem is not likely to be resolved [48]. Since there is a sharp corner present in the adopted model, along with the difference in the inlet profile, a discrepancy seems of 21% is actually surprisingly close to the reference solution.

Since it was confirmed that the proposed parameters yields results close to the reference solutions, the parametric study on whether the proposed parameters is able to generate converged results was present in the next section.

4.3.3   Result of Parametric Study

As the selected parameters are able to yield results that are acceptably close to the BLWT, this section focus on the convergence of the results based on parameters, including first cell height, domain size, tank shell grid size, and bottom surface grid size.

The first parameter studied in this section was the first cell height. To study the effect of the first cell height, four different first cell height, 0.01 mm, 0.1 mm, 1 mm, and 5 mm, were selected. The arrangements of the grid elements in the near wall region are presented in Figure 4-5, and the corresponding analyses results are complied in Table 4-3. With different first cell height, the result pressure coefficients do not differ from each other drastically. $C_p(0°)$ of all three analysis falls around 0.89~0.92, which correspond to a 3% of difference. The locations of $C_{p,suc}$ are close as well. Accounting for the fact that the nodes may not be located at identical locations from model to model, locations of $C_{p,suc}$ may be viewed as converged. The magnitude and the distribution of $C_{p,suc}$, however, is somewhat suspicious. The analysis with first cell height of 1 mm and 5 mm showed a relatively larger discrepency compared to analyses with first cell height of 0.1 mm and 0.01 mm. Besides, the pressure coefficient distribution obtained through analysis with first cell height of 1 mm is not symmetric. The pressure distribution of the pressure coefficient contours obtained with first cell height of 1 mm and 0.1 mm are presented in Figure 4-6. Note that the pressure coefficient of grids right at the shell height is excluded because of the divergence at this singularity points. Including the pressure coefficient at these points introduce a huge unnecessary pressure gradient, and make the figures unclear.

In Figure 4-6 (a), it can be observed that the pressure coefficient is not symmetric if the pressure coefficient in the region of 50° to 90° is compare with the pressure coefficient in the region of -50° to -90°. In the contrast, Figure 4-6 (b) presents a more symmetric distribution with respect to the windward meridian. Even 2000 more iterations were done in the analysis with first cell height of 1 mm, the problem of unsymmetric solution profile was not solved. It was, thus, determined that though a first cell height of 0.1 mm may yield a slight discrepancy in the obtained results comparing with results obtained through analysis with first cell height of 0.01 mm, since a first cell height of 0.1 mm generated a solution for which the pressure profile was symmetric, a first cell height of 0.1 mm was considered to be adequatly small. For further simulations, the first cell height, was therefore, fixed to 0.1 mm.

With the decided first cell height, the effect of downstream length was examined. Downstream length of 15H, 10H, and 5H were tested. The velocity magnitude vector diagrams at the mid-

surface (x-y plane) are presented in Figure 4-7, and subfigure (a), (b) and (c) are results for downstream length of 15H, 10H, and 5H, respectively. It can be observed that in Figure 4-7, the flow condition of all three analyses are similar. There is no any air flowing in from the outlet surface. $C_p(0°)$, $C_{p,suc}$, and location of $C_{p,suc}$ of three analyses barely differ from each other (see Table 4-4), which indicates that all three downstream length shall be enough to obtain a converged result in this particular case. However, to prevent from a diverged result in any further analysis with a different tank geometry, 10H as suggested by Tominaga et al. [37] was adopted for all the following analysis.

Next, the grid size on the tank face was studied, including 50 mm, 5 mm, and 2 mm. Section views of the arrangements of the grid elements are presented in Figure 4-8, and the analysis results are presented in Table 4-5. It can be observed that there is not any predominant difference between the results obtained by varying the grid size on the tank shell. For the practical design, however, the pressure at the windward stagnation point is an important design parameter, and obtaining a converged pressure coefficient at the stagnation point is considered essential. Therefore, though 50 mm may be considered to be an acceptable grid size, an even finer 5 mm was adopted in the following analyses. To make it compatible with other tank sizes, it is assumed that the grid size shall be less than $H/20$ on the tank shell, and $R/20$ on the tank roof, with R being the radius of the tank.

To investigate the effect of the grid size on the bottom surface, several different grid sizes on the bottom surface were examined, including 10 mm, 5 mm, and 3 mm. Section views of the arrangements of the grid elements are presented in Figure 4-9, and the analysis results are presented in Table 4-6. Hardly can any difference between the results generated by different bottom surface grid size be observed in Table 4-6. Nevertheless, if the pressure coefficient contour in Figure 4-10 is considered, a deficiency of bottom surface grid size of 10 mm can be observed. In Figure 4-10 (a), which is the pressure coefficient contour obtained through the analysis with bottom surface grid size of 10 mm, it is obvious that the contour is no as symmetric as Figure 4-10 (b), which is the pressure coefficient contour obtained through the analysis with bottom surface grid size of 5 mm. Though the pressure at the stagnation point is very close, it is decided that a bottom surface grid size of 5 mm to be employed in the further analyses.

As all the meshing strategies and the computational domain size has been determined, a study on the effect of turbulence model is presented hereby. Turbulence models including standard k-ε, realizable k-ε, standard k-ω, SST k-ω, and BSL k-ω were tested and the analyses result are presented in Table 4-7, and the pressure coefficient distribution is complied in Figure 4-11. In Table 4-7, except analyses with RNG k-ε and SST k-ω, all the other models predicted $C_p(0°)$ to be around 1.05~1.06, which is relatively high compare to the standard test case adopting RNG k-ε model. The location of $C_{p,suc}$, are close in all six analyses. The location predicted by different turbulence models ranged from 81.27° to 86.61°. The magnitude of $C_{p,suc}$ is also close, with obtained $C_{p,suc}$ ranging from -0.85 to -1.00. The analysis with standard k-ω has the largest difference in $C_{p,suc}$ (15%) comparing to the reference solution. However, in Figure 4-11, it can be observed that except analysis with the standard test (RNG k-ε) case and standard k-ω, all the other cases generates a pressure distribution contour that is not as symmetric with respect to the $\theta = 0°$ axis. As mentioned in section 4.2.4, an analysis employing standard k-ω model diverged badly in a preliminary study, it is not considered to be a suitable type of a model for further analysis. Therefore, RNG k-ε model is utilized in the rest of the study because of the favorable results it generated.

As a summary, the only difference in Table 4-1 after the parametric study is done would be the downstream length. The downstream length was determined to be 10H rather than 15H.

4.3.4   Further Validation on the Selected Parameters

As all the input parameters were decided only based on one tank (aspect ratio of 0.5), another tank was selected in this section to ensure the result obtained from the analysis with input parameters in conformance with the selected criteria will converge.

Another tank tested by MacDonald et al. [19] with diameter of 0.2 m and height of 0.4 m and a flat roof is studied in this section. According to the purposed criteria complied in 4.3.3, a set of standard input parameters for this test is complied in Table 4-8. To verify the convergence of the proposed criteria, the first cell height, downstream length, grid size on the tank shell, and the grid

size on the bottom surface of the domain were examined through four analyses. The tested parameters are presented in Table 4-9, and the corresponding grid discretization are complied in Figure 4-12. The corresponding analysis results are shown in Table 4-10. Note that since the result of this tank reported by MacDonald et al. [19] was the pressure distribution at $y = 312$ mm, both the magnitude and location of $C_{p,suc}$ were considered at this height.

By comparing the results in Table 4-10, it can be observed that the pressure coefficients and location of $C_{p,suc}$ obtained through the standard case is similar with those obtained through analyses with finer grid discretization or longer domain size. Interestingly, there is a 3% discrepancy between the $C_p(0°)$ obtained by the standard test case and the $C_p(0°)$ generated by all the other test cases. Though, since it is such a small difference, the standard input parameter set was considered to be able to generate a converged $C_p(0°)$. In terms of $C_{p,suc}$, there is a noticeable 6% difference between the $C_{p,suc}$ obtained through the standard test case and test case 3, for which the grid size on the tank shell was refined. This is possibly because a finer mesh on the tank shell improves the quality of the cells. In other words, the ratio of the longest dimension to the shortest dimension of a cell is lessened by refining the mesh. However, to keep the analysis time efficient, and because the difference was not considered to be gross, the established criteria was remained unchanged.

Since all the input parameters were decided, CFD analyses on tanks with various geometries and roofs configuration were conducted and presented in section 4.4.

4.4   CFD Analysis on Various Tanks

As the criteria for determining the input parameters for CFD analysis were established, this section aimed to apply the criteria to tanks with diverse geometries. In this section, pressure distributions on tank shells and tank roofs were presented and the effect of aspect ratio and roof configuration on the pressure distribution were discussed.

4.4.1 Computational Model Set-up for the Examined Tanks

In this section, tanks with aspect ratios ranging from 0.4 to 2 were studied. Roof configurations including flat, conical, and dome roofs were considered. Tanks studied by MacDonald et al. [19], Portela and Godoy [28, 29] were adopted and their BLWT results were used as reference solutions for a comparison purpose.

The tanks adopted in this section are complied in Table 4-11. For tanks with conical roofs, the tip 0.2 mm of the roofs were truncated to avoid from creating singularity points for the analyses. Additionally, this feature simulates the fact that for most of the tanks with conical roof, a top nozzle is usually installed at the center of the roof. A cross section (*x-y* plane) of Tank D is shown in Figure 4-13 to illustrate this feature.

The input parameters followed the established criteria described in section 4.3.3. Grid sizes and computational domain sizes were selected based on the geometries of the individual tanks. To determine the downstream length for tanks with conical or dome roofs, the total height of the tanks instead of the shell height were referenced.

CFD analysis results can be found in Table 4-12, and the discrepancies between the analysis results and the reference solutions are presented in Table 4-13. To further interpret the results, effect of aspect ratio and the effect of roof geometry were discussed in the sections 4.4.2 and 4.4.3, respectively. Note that to compare the CFD results with the reference solutions, $C_{p,suc}$ and its location were read from different heights in each individual case. This is because of the tank heights from tank to tank were different, and pressure tap shall be installed within the range of 60% to 90% of the shell height to ensure the largest pressure coefficient can be measured. Thus, according to different tank geometries, pressure taps were installed at different heights by researchers, and the CFD results were read accordingly. The height at which the $C_{p,suc}$ and its location were read are complied in Table 4-12.

4.4.2 Effect of Aspect Ratio on Pressure Distribution of Tank Shell

With the obtained results, this section mainly focus on how aspect ratio affects the discrepancies between the CFD simulation results and reference solutions, and the simulation results between tanks with different aspect ratios. For discussion purpose, Tanks A, B, and C were referred to as Group 1 (flat roof tanks) and Tanks D, E, and F were referred to as Group 2 (conical roof tanks).

In Table 4-13, difference between magnitude and location of $C_{p,suc}$ obtained through CFD and reference analysis did not seem to be drastic. For analyses with all the tanks in Groups 1 and 2, the locations of $C_{p,suc}$ predicted by CFD show a good agreement with the reference solution, with a maximum discrepancy of 4.6% as presented. The CFD results in Table 4-12 show that the higher the aspect ratio, the higher the suction (larger absolute value of $C_{p,suc}$) would be. By comparing the absolute value of $C_{p,suc}$ obtained through CFD, $C_{p,suc}$ of Tank C ($H/D = 2.0$) is roughly 50% higher than $C_{p,suc}$ of Tank A ($H/D = 0.5$). If Tanks D and F were considered, similar trend can be observed as well. Similar relationship between aspect ratio and $C_{p,suc}$ holds in the reference solution presented by MacDonald et al. [19]. In the reference solutions, the absolute value of $C_{p,suc}$ of Tank C is 70% higher than the absolute value of $C_{p,suc}$ of Tank A.

A relationship between discrepancies and aspect ratio was observed within both Groups 1 and 2. By comparing the $C_{p,suc}$ for individual tanks between the CFD results and the reference solution in Table 4-13, it can be observed that the higher the aspect ratios of the tanks, the higher the discrepancies are. For Tank A, there is a very good agreement between $C_{p,suc}$ obtained through CFD and the reference solution. However, as the aspect ratio increases, the discrepancy between $C_{p,suc}$ obtained through CFD and the reference solution increased as well. For Tanks B, the discrepancy is 7.1%, and for Tanks C, the discrepancy is 15%. For tanks in Group 2, similar trend of the discrepancy between CFD analysis and reference solution can be observed. This trend, for which the CFD analysis results for tanks with lower aspect ratio aligned with the reference results better, is likely a consequence that the input parameters were calibrated based on Tank A, whose aspect ratio is 0.5. Thus, for tanks with higher aspect ratio, the CFD results do not have a perfect agreement with the reference solution. Nevertheless, though the suction predicted by CFD analysis

seems to be smaller, as a suction does not cause buckling of tank shells, it hardly affects the design of shell.

In terms of $C_p(0°)$, for Tanks A and D, the $C_p(0°)$ are 6.1% and 1.1% below the reference solutions, which are fairly close to the reference solution, and can be considered satisfactory. On the other hand, for taller tanks (Tanks B, C, E, and F), the discrepancies between $C_p(0°)$ obtained through CFD analysis and reference solutions are 11%, 16%, 14%, and 23% for Tanks B, C, E, and F, respectively. The CFD analysis results shall be adequate, despite a relatively large discrepancy between CFD and reference solution from a structural design point of view; the $C_p(0°)$ solved by CFD are higher than reference solutions. In other words, if CFD is considered to be a tool to obtain wind pressure coefficient for design, it will result in a conservative shell design since $C_p(0°)$ predict by CFD are larger than the published BLWT results.

By further analyzing the CFD results in Table 4-12, it can be observed that CFD suggest that the higher the aspect ratio, the higher the $C_p(0°)$ for both Groups 1 and 2. However, this pattern is not observed in the results of the reference solutions. Moreover, for Group 2, the reference solution even suggested an opposite pattern, indicating the higher the aspect ratio, the lower the $C_p(0°)$. To further argue on this trend, the BLWT conducted by Sabransky and Melbourne [18] was considered. The results by Sabransky and Melbourne [18] showed that $C_p(0°)$ are 0.78, 0.80, and 0.81 for cylinders with aspect ratio of 0.7, 0.8, and 1.2, respectively, indicating a similar positive correlation between $C_p(0°)$ and aspect ratio in the CFD simulation results. Note that the models adopted by Sabransky and Melbourne [18] had a roof pitch of 27°. Though the discrepancies between the presented $C_p(0°)$ and the results by Sabransky and Melbourne [18] are still not negligible, the positive correlation between $C_p(0°)$ and aspect ratio matched. It seems that further research on the effect of aspect ratio by adopting BLWT on the wind pressure distribution of close-top tanks will be valuable.

4.4.3   Effect of Roof Configuration on Pressure Distribution of Tank Shell

As the effect of aspect ratio has been discussed, this section focus on the effect of roof configuration on pressure distribution on the tank shells. To discuss the effect of the roof

configuration, Tanks A, D, G, H, and I were classified as Group A, Tanks B and E were classified as Group B, and Tanks C and F were classified as Group C, based on the similarity of aspect ratios.

$C_p(0°)$ obtained through CFD show a favorable agreement with the reference solutions for all tanks in Group A. The maximum discrepancy of $C_p(0°)$ for tanks in Group A between the CFD analysis and the reference solution is 6.1%. For other tanks, the discrepancies are less than 3%, indicating CFD simulation being capable to predict $C_p(0°)$ of these tanks. $C_p(0°)$ of all tanks in Group A obtained through CFD in Table 4-12 are fairly close to each other, with a maximum discrepancy of 3.4% between Tanks A and G. This implies that the selected criteria for CFD analysis yields converged results regardless of the roof configuration.

To further discuss the discrepancy of $C_p(0°)$ between CFD result and reference solution, $C_p(0°)$ between the reference results were compared. It can be observed in the reference solution, $C_p(0°)$ for Tank A is noticeably larger than $C_p(0°)$ of Tanks D, G, H, and I. However, by comparing $C_p(0°)$ obtained through CFD or reference solution in Group A, it can also be stated that $C_p(0°)$ is almost independent of roof configuration. MacDonald et al. [19] also made the conclusion that for tanks with an identical aspect ratio and roofs, the pressure distributions are almost independent to the roof geometry. Based on this observation, $C_p(0°)$ of Tank A shall be similar to referenced $C_p(0°)$ of Tanks D, G, H, and I as well. Actually, $C_p(0°)$ of Tank A obtained through CFD has a maximum discrepancy of 3.4% comparing to the reference solution $C_p(0°)$ of Tanks D, G, H, and I. Thus, it should be safe to state that the obtained $C_p(0°)$ is satisfactory. Note that the fact that the pressure distribution profile on the tank shell is independent of the roof configuration is also reflected in the current design codes including EN1993-4-1 [49] and AS/NZS 1170.2:2011 [21]. The wind pressure distributions profile on tank shells are independent of roof configurations in these documents as long as the tank has a roof.

Within Group A, it can be observed that both the magnitude and the location of $C_{p,suc}$ for most of the tanks seem to be acceptable, with a less than 10% discrepancies comparing with the reference solution. The only tank whose $C_{p,suc}$ does not correspond to the reference solution perfectly is Tank I, and a 21% discrepancy between the CFD analysis and the reference is observed. Compare

to $C_{p,suc}$ of other tanks, such as Tanks A and C, $C_{p,suc}$ of Tank I obtained through CFD does not seem to be grossly off. Actually, though $C_{p,suc}$ of Tank H is closer to the reference solution, $C_{p,suc}$ of Tank H seem to be lower than other tanks with an aspect ratio of 0.5 (not including Tank G). It is interesting that Tank H aligned with the reference result better, but is relatively off from the CFD results of other tanks with an aspect ratio of 0.5. However, as mentioned earlier, suction does not induce buckling on tank shells, and, also, CFD analysis is able to predict the location of $C_{p,suc}$ fairly accurate, indicating the behavior of the wind flow is being captured, it should be safe to state that the proposed criteria are satisfactory. It is noticeable that $C_{p,suc}$ obtained through CFD for Tank G is lower than $C_{p,suc}$ of other tanks in Group A. This is due to the fact that Tank G has a lower aspect ratio ($H/D = 0.4$). As mentioned, the trend that the lower the aspect ratio, the lower the absolute value of $C_{p,suc}$ was observed by MacDonald et al. [19] and was confirmed in the present study.

Similar to what being observed within Group A, the CFD results within Groups B and C also show consistencies between tanks with different roof configuration. The discrepancies between the CFD analysis results and reference solutions within Groups B and C also show a close value with different roof configuration. For Group B, both Tanks B and E show a discrepancy in $C_p(0°)$ of 11%. Though, the discrepancy in $C_{p,suc}$ do not seem to be as consistent (7.1% and 14% for Tanks B and E, respectively), while the reference solutions themselves already have a noticeable difference. The $C_{p,suc}$ obtained through CFD again converged to similar pressure coefficients. For Group C, the analysis results of Tanks C and F converged to similar values as well. Besides, the discrepancy of both magnitude and location of $C_{p,suc}$ between simulation results of Group C and reference solutions are consistent. The discrepancy of $C_p(0°)$ between CFD results and reference solution for Tanks C and F is relatively off from each other, but both of them are roughly 20%.

Comparing the CFD results within Groups B or C, it can be observed the analysis results are almost on top of each other. This strengthen the statement that the wind pressure profile on tank shell for tanks with identical or similar aspect ratio shall be almost independent of the roof configuration as long as there is a roof.

4.4.4 Pressure Distributions of Analyzed Tanks

As the most significant features of the pressure coefficient on the tank shell were compared with the reference solutions, the pressure coefficient of the analyzed tanks obtained through CFD were presented. Since the distribution on the shell had a better convergence, the pressure distribution on the shell of all tanks were shown in this section. Pressure coefficient contours of tanks adopted from study by MacDonald et al. [19] (Tanks A through F) are complied in Figure 4-14, pressure coefficient contour of tank adopted from study by Portela and Godoy [28] (Tank G) is complied in Figure 4-15, and contours of tanks adopted from study by [29] (Tanks H and I) are complied in Figure 4-16. The y-axis of subfigures in Figure 4-14, Figure 4-15, and Figure 4-16 are height (y) at which the pressure coefficient were considered normalized with the respective shell height (H).

It can be observed that Figure 4-14 (a), (c), (d), and Figure 4-16 show a nice symmetric pressure distribution with respect to the windward meridian. Figure 4-14 (a), (c) are results obtained from the tanks employed in the parametric study, and thus it is not surprising for the result to be favorable. Figure 4-14 (d) and Figure 4-16 are obtained from tanks with aspect ratio of 0.5, which is identical to the Tank A, and thus the results are also favorable.

For Figure 4-14 (b) and (e), relatively unsymmetrical distributions in pressure coefficients are observed and this is somewhat interesting. Results of Tanks A and C do not show such an unsymmetrical distribution. As Tank B has an aspect ratio that is between Tanks A and C, it was expected that result for at least Tank B to be favorable because the parametric study was based on tanks with flat roofs. Similar non-symmetric pressure coefficient contour on Tank E is observed. Contour of Tanks D and F also show relative favorable results, while contour of Tank E can be improved. Result of Tank G does not seem to be unacceptable since the symmetric pattern can still be observed. From a design point of view, the buckling of tank under wind gusts are usually more associated with the pressure distribution in the positive pressure region. From Figure 4-14, Figure 4-15, and Figure 4-16, it seems that the pressure distributions in the positive pressure region are fairly symmetric, and thus CFD can be considered to be a powerful tool for practical design.

Since reference solution for the pressure coefficient on flat roofs are available, the pressure coefficient of Tanks A, B, and C are complied in Table 4-14, and the pressure coefficient are

complied in Figure 4-17. Accounting for the reasons (mentioned in section 4.3.2) that leads to discrepancy between the averaged pressure coefficient obtained through CFD and reference solutions, the discrepancies do not seem to be large. $C_{p,R1}$ is consistently overestimate by CFD, and the percent of the overestimation seems to have a positive correlation with the aspect ratio of the tank. The pressure in Region 1 is likely to control the design of connection between tank shell and roof. Since the pressure coefficient is overestimate by CFD, it will result in a conservative design. $C_{p,R2}$ and $C_{p,R4}$ seems to be consistently underestimated by CFD. Though the suction being underestimated in Region 2, the discrepancies in the region is small compare to other regions. The discrepancies in Region 4 is noticeable, but the pressure in this region is small compare to others, and it is not likely to govern the design of the connection between tank roof and tank shell. Moreover, the behavior of the wind flow seems to be captured successfully by CFD analyses. $C_{p,R3}$ are also nicely predicted by the CFD simulations. For Tanks A and C, $C_{p,R3}$ in this region almost match the reference solution. Though $C_{p,R3}$ of Tank B seems to be overestimated by 20%, considering all the possible difference between the CFD analysis and the wind tunnel test, this discrepancy shall be acceptable. This again indicated that CFD is indeed a powerful tool for practical wind design for tanks.

For a demonstration purpose, selected pressure coefficient on conical and dome roofs are presented in Figure 4-18. Tank E is chosen to be presented in Figure 4-18 because it is the only tank for which the pressure coefficient contour is presented by MacDonald et al. [19]. Tank H was chosen to show the pressure coefficient distribution on a dome roof. Since there is no original data available, no quantitative comparison can be done to compare the pressure coefficient on conical and dome roofs. Qualitatively, roof pressure distribution of Tanks E and H do not seem to be grossly off from the reference solutions. Note that Figure 4-18 (a) can be somewhat deceiving, since the pressure coefficient at the tip of the roof actually diverged. The maximum suction pressure coefficient at the tip is -3.59. Since the behavior is very local, and including the large suction value would make the figure difficult to read, the large suction at the apex region was hereby excluded. For comparison purpose, refer to study by MacDonald et al. [19] and Portela and Godoy [29] for pressure distribution contours obtained through BLWT.

4.5 Conclusion

This paper aims to investigate how CFD can be applied to obtain the wind pressure distribution on close-top tanks with flat, conical, and dome roofs. Tanks with aspect ratio ranging from 0.4 to 2 were adopted in this study. CFD analyses adopting a RANS model were conducted, and a through grid independence study on a tank with an aspect ratio of 0.5, and study on necessary input parameters were presented.

Since the solution provided by CFD is heavily dependent on the grid discretization, a grid independence study was conducted to ensure the obtained result is a converged solution. In this paper, mesh strategies including first cell height, grid discretization on tank shell, and grid discretization on bottom surface of computational domain were investigated. A tank with an aspect ratio of 0.5 and a flat roof was adopted for this study. Criteria for determining the grid discretization were proposed and the analysis results were calibrated with the available BLWT results. The proposed criteria includes a first cell height of 0.1 mm, a grid size on the tank shell of 5 mm (H/20), and a grid size on bottom surface of the computational domain of 5 mm (H/20). The effect of the downstream domain size and the effect of turbulence model were studied as well. It was concluded that, though a downstream domain size of $5H$ seems to be adequate to obtain a converged result, a downstream domain size of $10H$ as Tominaga et al. [37] suggested was adopted to keep further analyses from diverging. In terms of turbulence model, it was determined that RNG k-ε model yields a favorable result. It can be concluded that CFD may be a suitable tool to predict the pressure distribution on both the shell and the roof of a tank. To ensure that for a tank with different aspect ratio, the proposed criteria can guarantee a converged result, a tank with an aspect ratio of 2 and a flat roof was tested. It turned out that following the proposed criteria, the simulation result was able to converge.

With the criteria of deciding the input parameter being established, tanks with aspect ratios ranging from 0.4 to 2 were studied. Roof geometries including flat, conical, and dome roofs were employed. It was concluded that if the tank and the computational set up follows the proposed criteria, CFD produced converged pressure coefficient. Indeed, as discussed, there were some discrepancies between the pressure coefficient obtained through CFD results and published BLWT

results, but it seems that the pressure coefficient obtained through CFD analysis provides a pressure profile that is either accurate enough or is more conservative than the reference solutions.

By analyzing the CFD results, it is observed that for all the analysis, the location of $C_{p,suc}$ aligned with the reference result nicely. The magnitudes $C_{p,suc}$ obtained through CFD also fairly aligned with the reference solution, and the positive correlation of $C_{p,suc}$ observed in the CFD results correspond to what MacDonald et al. [19] found. The $C_p(0°)$ obtained from CFD were either close to the reference solution, or more conservative than the reference solution. Besides, magnitudes of $C_p(0°)$ obtained through CFD showed a positive correlation with the aspect ratio of the tank, while this was not observed by MacDonald et al. [19]. To further discuss on this trend, BLWT results reported by Sabransky and Melbourne [18] was considered, and similar positive correlation between aspect ratio and $C_p(0°)$ can be observed.

For tanks with similar aspect ratios but different roof configurations, the CFD results on the shell aligned with each other. The published BLWT results also suggested that the roof configurations do not pose a huge impact on the pressure distribution on the shell. This implies that though the analyses with conical roofs may be diverging badly at the tip of the roof even the tip was truncated, the pressure distribution on the shell was not heavily affected.

Finally, the pressure coefficient distributions on tank shells and roofs were presented. It was interesting that the pressure distribution obtained through CFD for Tanks B and E were not as favorable comparing to Tanks A, C, D, and F as the aspect ratios of Tanks B and E in between the aspect ratios of Tanks A and C and Tanks D and F. Nevertheless, the results for Tanks B and E was still acceptable. The averaged pressure coefficient on flat roof seem to be satisfactory for a design purpose. Though $C_{p,R1}$ seemed to be overestimated by CFD, considering a larger suction on the roof will result in a more conservative design of the connection between tank roof and shell. $C_{p,R2}$ and $C_{p,R3}$ predicted by CFD have small discrepancies compare to the reference solutions. Though $C_{p,R4}$ seems to be off from the reference solution, as it is not likely to control the design, it was considered to be satisfactory.

Due to the lack of raw BLWT data, a quantitative study on pressure coefficient of tanks with dome and conical roofs was not made to study the pressure distribution on the tank roof. Qualitatively, the pressure distribution on conical roof of Tank E and dome roof of Tank H did not seem to be grossly off from the published BLWT results even though the analysis seemed to diverge at the tip of a conical roof.

4.6   Tables

Table 4-1. Input parameters for the standard test case for the parametric study.

Turbulence model	RNG k-ε model
First cell height	0.1 mm
Tank face grid size	5 mm
Grid size on the bottom surface of the domain	5 mm
Maximum grid size	50 mm
Lateral, top, and upstream domain size	0.5 m
Downstream domain size	1.5 m
Number of iteration	3000

Table 4-2. Comparison of CFD results with reference solutions obtained from BLWT.

	CFD	MacDonald et al. [19]
$C_p(0°)$	0.92	0.98
$C_{p,suc}$	-1.00	-1.00
Location of $C_{p,suc}$ (degree)	86.0	84.0
	CFD	Uematsu and Koo [24]
$C_{p,R1}$	-1.09	-0.90
$C_{p,R2}$	-0.81	-0.95
$C_{p,R3}$	-0.33	-0.32
$C_{p,R4}$	-0.17	-0.27

Table 4-3. Pressure coefficients of the study on first cell height.

First cell height (mm)	$C_p(0°)$	$C_{p,suc}$	Location of $C_{p,suc}$ (degree)
0.01	0.91	-1.03	87.0
0.1	0.92	-1.00	86.0
1	0.92	-0.95	84.1
5	0.89	-0.96	86.6

Table 4-4. Pressure coefficients of the study on the computational domain size.

Downstream Length	$C_p(0°)$	$C_{p,suc}$	Location of $C_{p,suc}$ (degree)
15H	0.92	-1.00	86.0
10H	0.92	-1.00	84.9
5H	0.93	-1.00	85.3

Table 4-5. Pressure coefficients of the study on grid size on the tank face.

Tank face grid size (mm)	$C_p(0°)$	$C_{p,suc}$	Location of $C_{p,suc}$ (degree)
50	0.89	-0.97	86.4
5	0.92	-1.00	84.9
2	0.92	-0.97	84.1

Table 4-6. Pressure coefficients of the study on grid size on the bottom face.

Bottom face grid size (mm)	$C_p(0°)$	$C_{p,suc}$	Location of $C_{p,suc}$ (degree)
10	0.93	-1.00	86.4
5	0.92	-1.00	84.9
3	0.92	-0.99	85.9

Table 4-7. Pressure coefficient of analyses with different turbulence models.

	$C_p(0°)$	$C_{p,suc}$	Location of $C_{p,suc}$ (degree)
RNG k-ε	0.92	-1.00	84.9
Standard k-ε	1.05	-0.98	86.6
Realizable k-ε	1.05	-0.93	86.0
Standard k-ω	1.06	-0.85	81.3
SST k-ω	0.88	-0.96	83.2
BSL k-ω	1.05	-1.00	86.6

Table 4-8. Input parameters for the standard test case used in section 4.3.4.

Turbulence model	RNG k-ε model
First cell height	0.1 mm
Tank roof grid size	5 mm
Tank shell grid size	20 mm
Grid size on the bottom surface of the domain	20 mm
Maximum grid size	0.2 m
Lateral, top, and upstream domain size	2.0 m
Downstream domain size	4.0 m
Number of iteration	3000

Table 4-9. Parameters of test cases carried out in section 4.3.4.

	Test 1	Test 2	Test 3	Test 4
Tested parameter	First cell height	Downstream domain size	Shell surface	Bottom surface
Adopted parameter	0.05 mm	6.0 m	5 mm	2 mm

Table 4-10. CFD analysis result for tests listed in Table 4-8 and Table 4-9.

Case	$C_p(0°)$	$C_{p,suc}$	Location of $C_{p,suc}$ (degree)
Standard	1.03	-1.45	84.3
Test 1	1.06	-1.46	85.3
Test 2	1.06	-1.45	86.0
Test 3	1.06	-1.54	85.3
Test 4	1.06	-1.46	83.7

Table 4-11. Tank geometries and roof configurations studied in section 4.4.

Name	Height (mm)	Diameter (mm)	Aspect ratio (H/D)	Roof configuration	Roof height (mm)	Roof pitch (degree)	Geometry reference
A	100	200	0.5	Flat roof	N/A	N/A	[19]
B	200	200	1.0	Flat roof	N/A	N/A	[19]
C	400	200	2.0	Flat roof	N/A	N/A	[19]
D	100	200	0.5	Conical roof	46.6	25	[19]
E	200	200	1.0	Conical roof	46.6	25	[19]
F	400	200	2.0	Conical roof	46.6	25	[19]
G	116	269	0.4	Conical roof	25.4	11	[28]
H	116	238	0.5	Dome roof	36.7	N/A	[29]
I	116	238	0.5	Dome roof	54.9	N/A	[29]

Table 4-12. CFD analysis results for Tanks A to I along with the reference solutions.

Tank	Height where $C_{p,suc}$ was considered (mm)	CFD			Referenced BLWT results		
		$C_p(0°)$	$C_{p,suc}$	Location of $C_{p,suc}$ (degree)	$C_p(0°)$	$C_{p,suc}$	Location of $C_{p,suc}$ (degree)
A	62.0	0.92	-1.00	84.9	0.98	-1.00	84.0
B	162	0.98	-1.18	83.7	0.88	-1.27	85.0
C	312	1.03	-1.45	84.3	0.89	-1.70	87.3
D	62.0	0.91	-0.97	82.4	0.92	-1.00	80.6
E	162	0.98	-1.21	83.0	0.88	-1.40	87.0
F	312	1.06	-1.45	82.6	0.86	-1.70	85.0
G	88.9	0.89	-0.85	89.3	0.90	-0.85	83.1
H	88.9	0.88	-0.91	88.1	0.89	-0.83	85.3
I	88.9	0.93	-1.02	87.1	0.91	-0.84	82.7

Table 4-13. Differences between CFD analysis results and the reference solutions for Tanks A to I.

Tank	Percent difference		
	$C_p(0°)$	$C_{p,suc}$	Location of $C_{p,suc}$ (°)
A	6.1%	0.0%	1.1%
B	11%	-7.1%	1.5%
C	16%	-15%	3.4%
D	1.1%	-3.0%	2.2%
E	11%	-14%	4.6%
F	23%	-15%	2.8%
G	1.1%	0.0%	7.5%
H	1.1%	-9.6%	3.3%
I	2.2%	-21%	5.3%

Table 4-14. CFD analysis results and reference solutions on flat roofs of Tanks A, B, and C.

Tank A			
	CFD	Uematsu and Koo [24]	Difference
$C_{p,R1}$	-1.09	-0.90	21%
$C_{p,R2}$	-0.81	-0.95	15%
$C_{p,R3}$	-0.33	-0.32	3.1%
$C_{p,R4}$	-0.17	-0.27	37%
Tank B			
	CFD	Uematsu and Koo [24]	Difference
$C_{p,R1}$	-1.19	-0.87	37%
$C_{p,R2}$	-0.97	-1.01	4.0%
$C_{p,R3}$	-0.42	-0.35	20%
$C_{p,R4}$	-0.20	-0.28	29%
Tank C			
	CFD	Uematsu and Koo [24]	
$C_{p,R1}$	-1.24	-0.79	57%
$C_{p,R2}$	-1.05	-1.13	7.1%
$C_{p,R3}$	-0.48	-0.49	2.0%
$C_{p,R4}$	-0.23	-0.29	21%

4.7   Figures
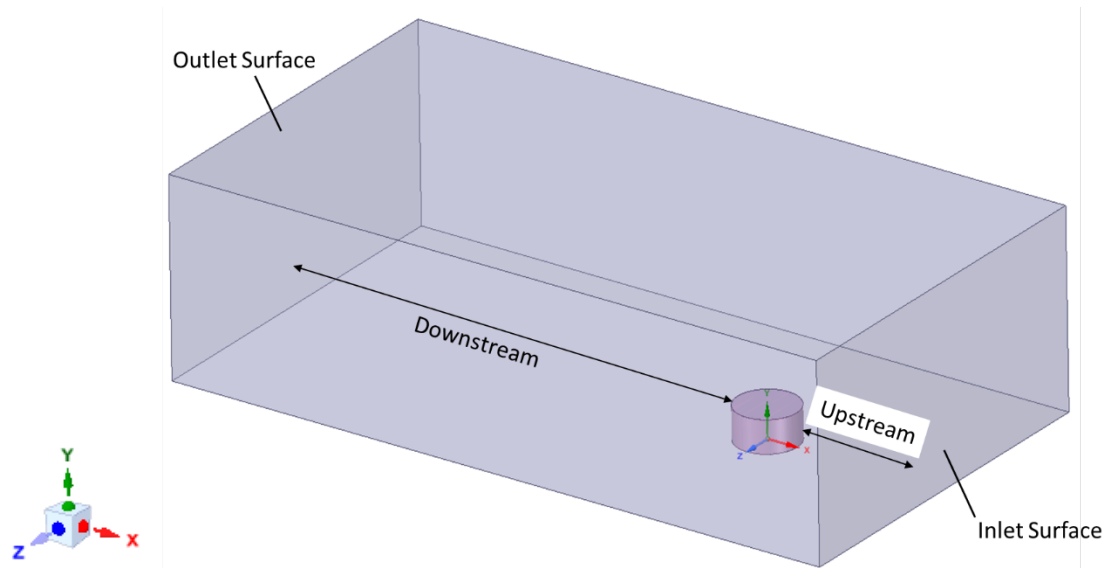
Figure 4-1. A fluid domain and a modeled tank.
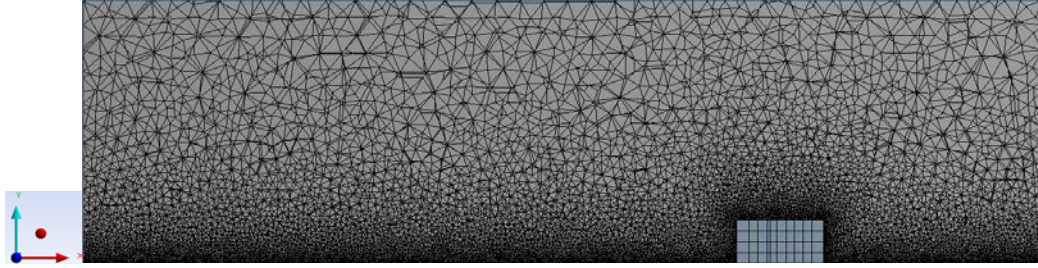
Figure 4-2. Section view (x-y plane) of grid discretization of the standard test case.
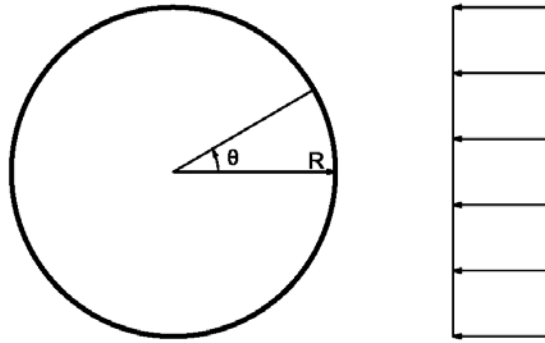
Figure 4-3. Definition of the cylindrical coordinate system. Wind blowing from the right hand side.
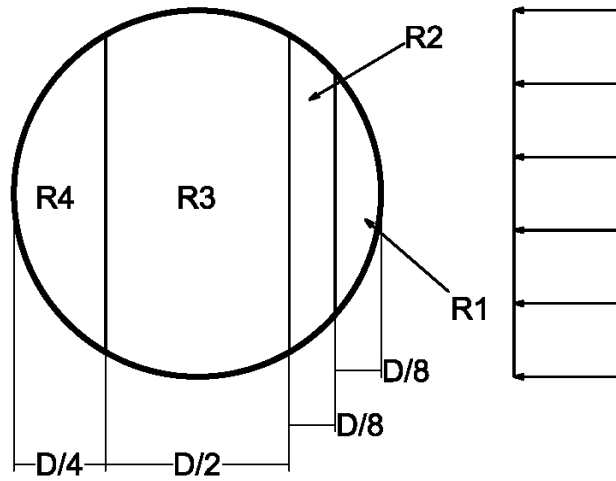
Figure 4-4. Definition of the roof regions. Wind blowing from the right hand side.
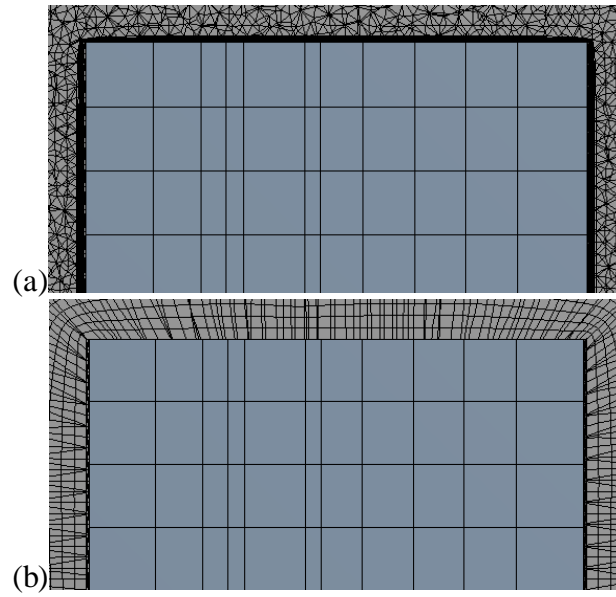
Figure 4-5. Section (*x-y* plane) view of the grid discretization at the near wall (tank) region. (a) Grid discretization with a first cell height of 0.1 mm. (b) Grid discretization with a first cell height of 5 mm.
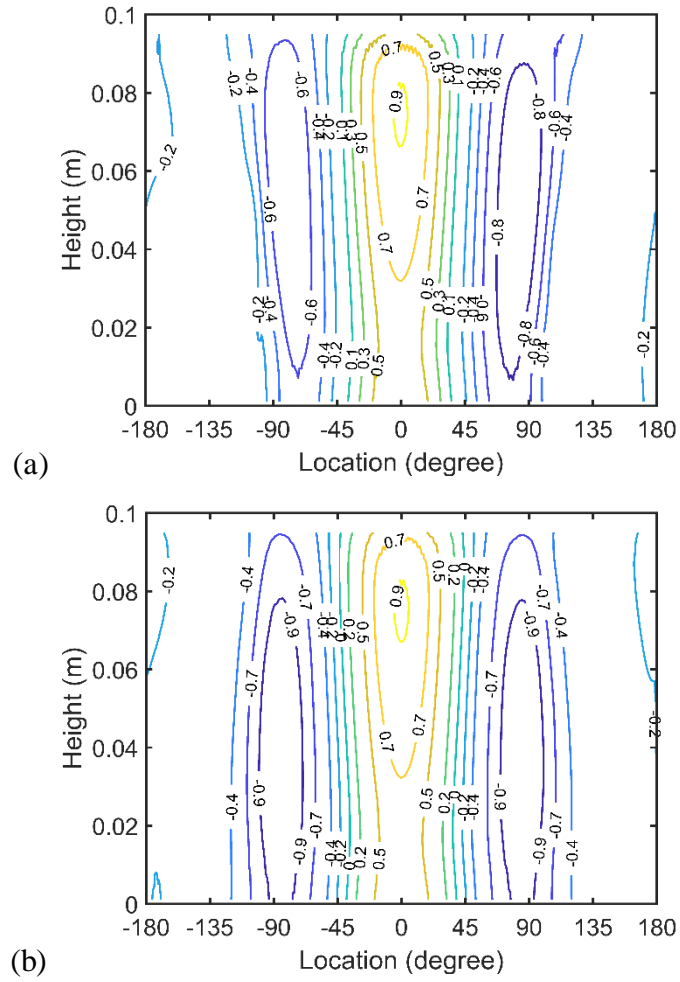
Figure 4-6. Pressure coefficient contour on the tank shell obtained from analysis with first cell height of (a) 1 mm (b) 0.1 mm.
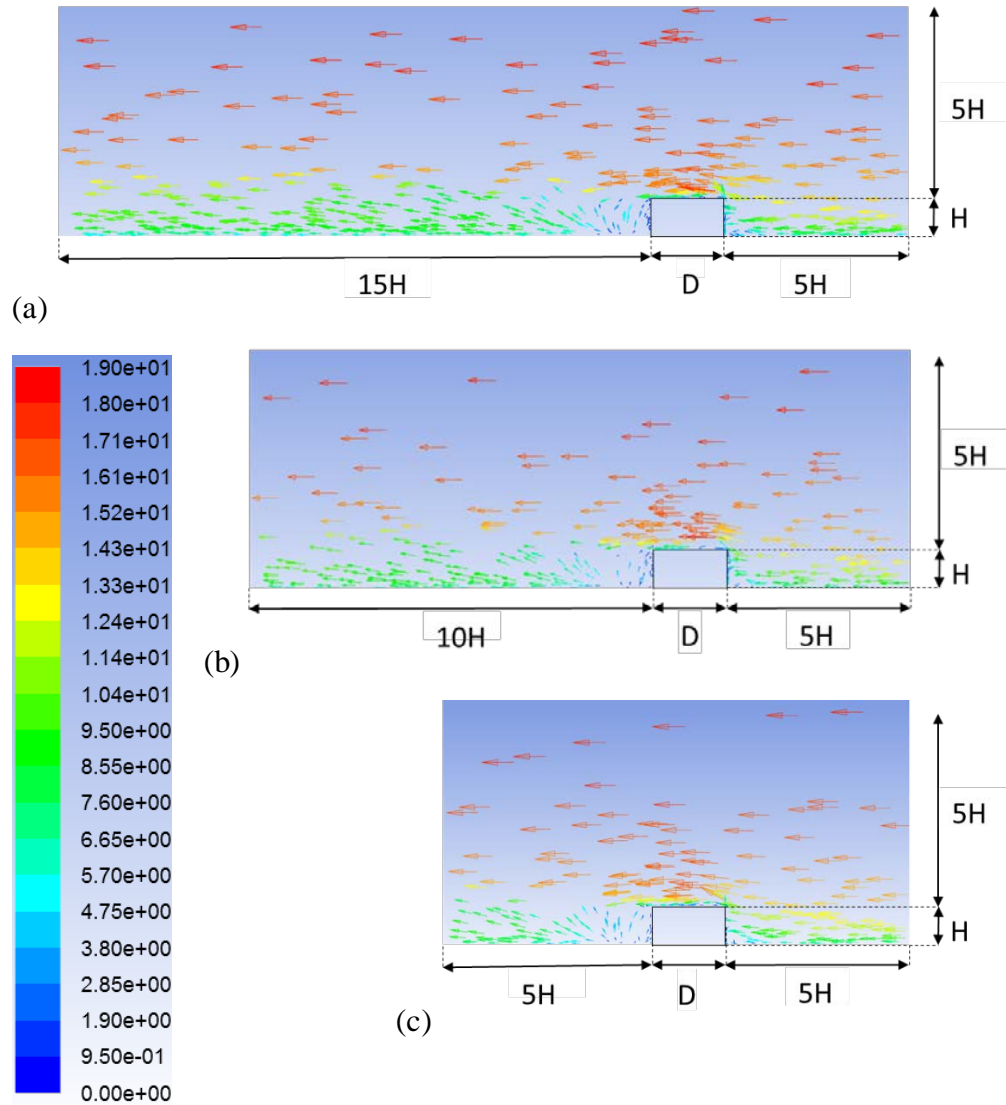
Figure 4-7. Wind velocity vectors at the *x-y* plane of the fluid domain. Wind blowing from the right hand side to left hand side. (a) Downstream length 15*H*. (b) Downstream length 10*H*. (a) Downstream length 5*H*.
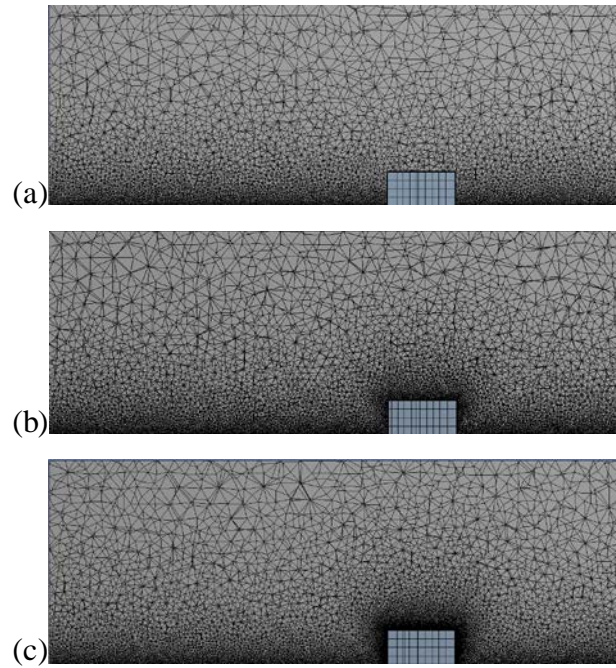
Figure 4-8. Section (*x-y* plane) view of the grid discretization of models with tank face grid size of (a) 50 mm (b) 5 mm (c) 2 mm.
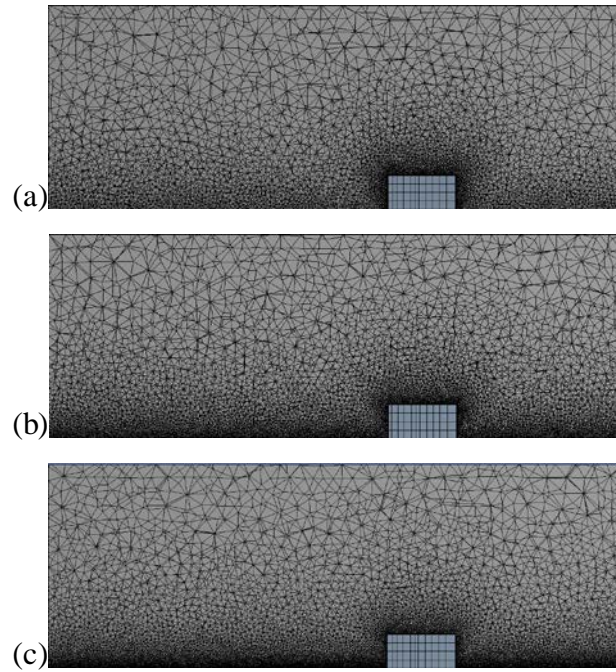
Figure 4-9. Section (*x-y* plane) view of the grid discretization of models with bottom surface grid size of (a) 10 mm (b) 5 mm (c) 3 mm.
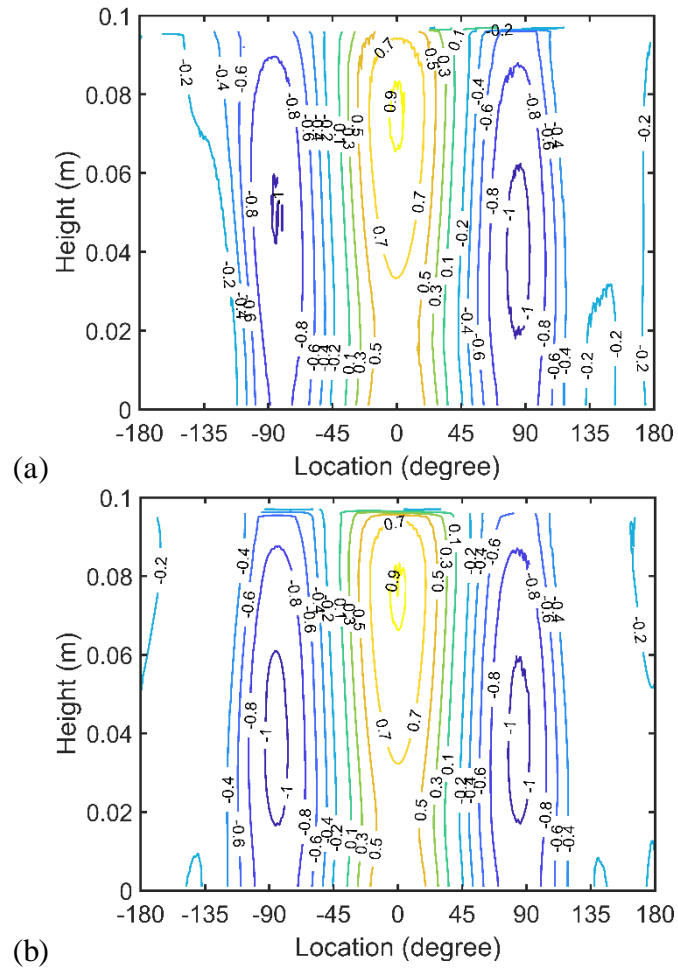
Figure 4-10. Pressure coefficient contour on the tank shell obtained from analysis with bottom surface grid size of (a) 10 mm (b) 5 mm.
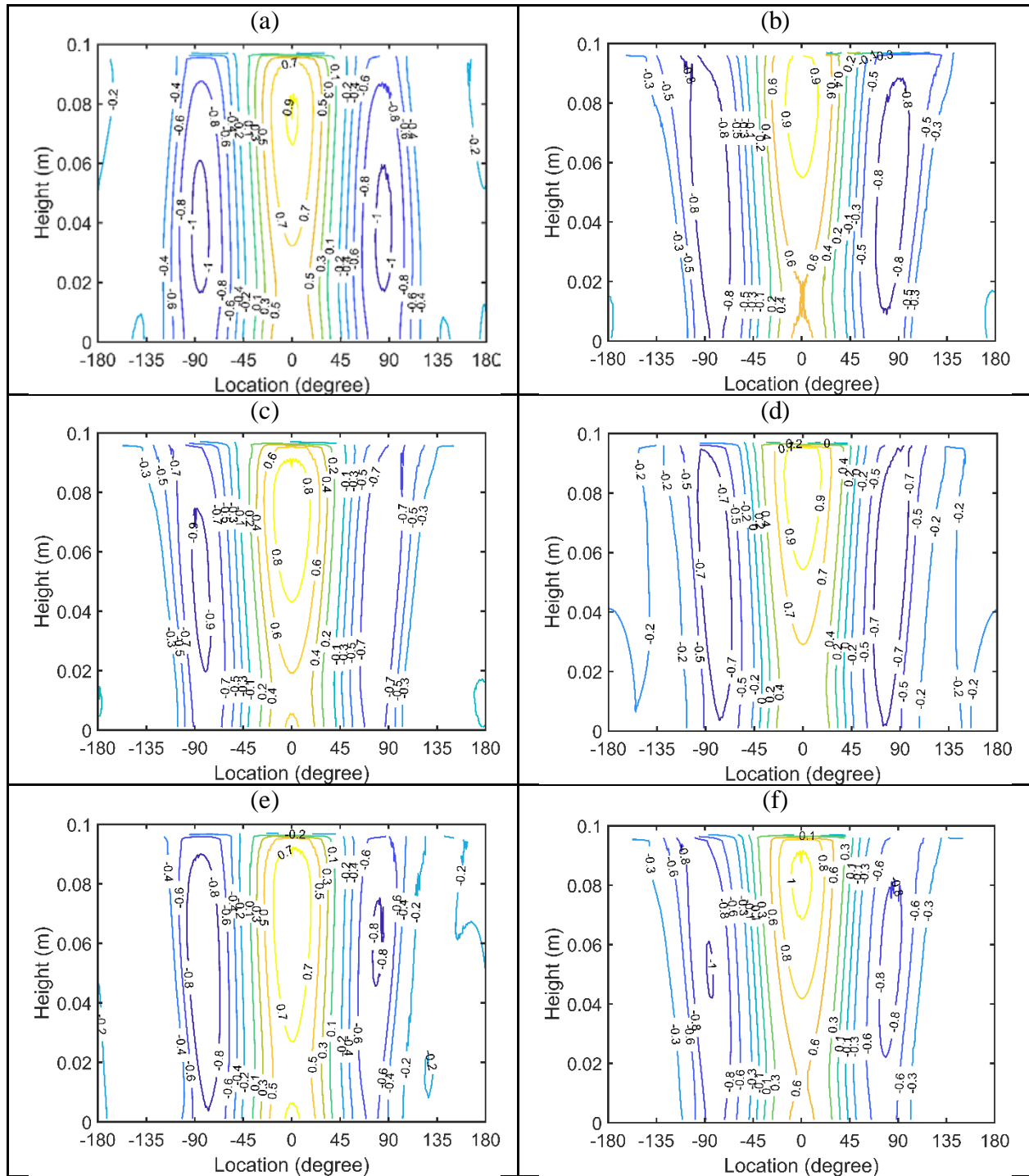
Figure 4-11. Pressure coefficient contours on the tank shell obtained from analyses with different turbulence models. (a) RNG $k\text{-}\varepsilon$ (b) standard $k\text{-}\varepsilon$ (c) realizable $k\text{-}\varepsilon$ (d) standard $k\text{-}\omega$ (e) SST $k\text{-}\omega$ (f) BSL $k\text{-}\omega$
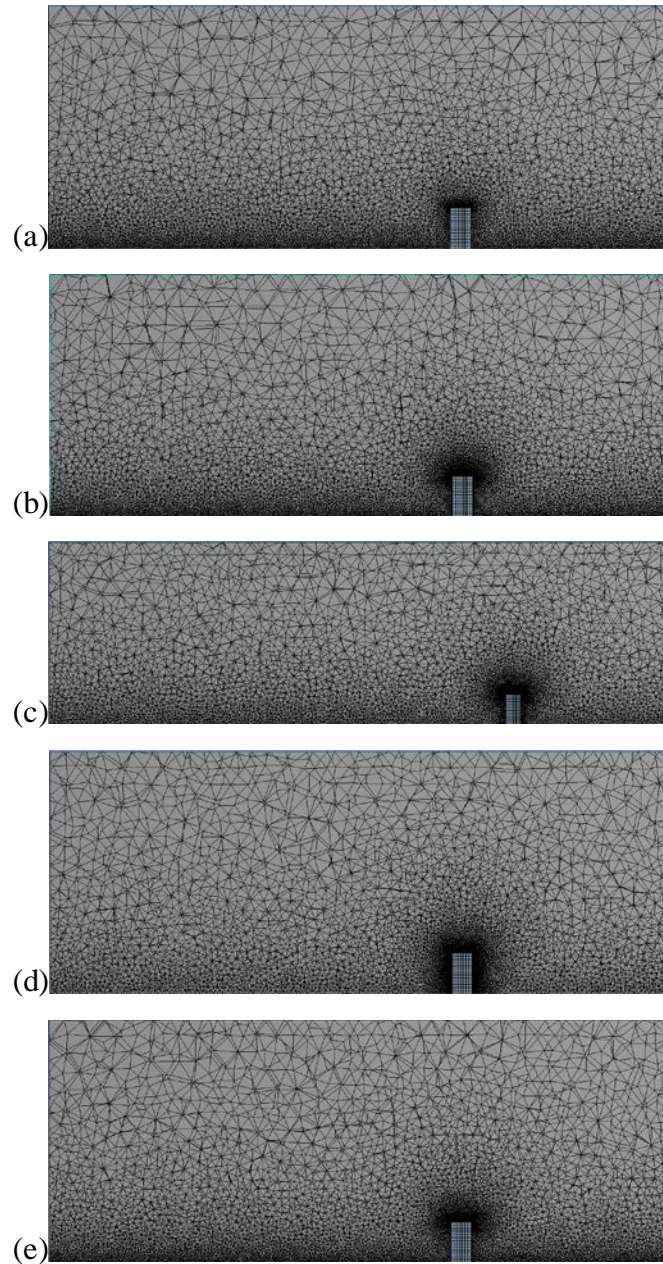
Figure 4-12. Section view (*x-y* plane) of grid discretization of the analysis conducted in section 4.3.4. (a) standard test case (b) analysis with first cell height of 0.05 mm (c) analysis with downstream length of 6 m (e) analysis with grid size on tank shell of 5 mm (d) analysis with grid size on the bottom surface of 2 mm.
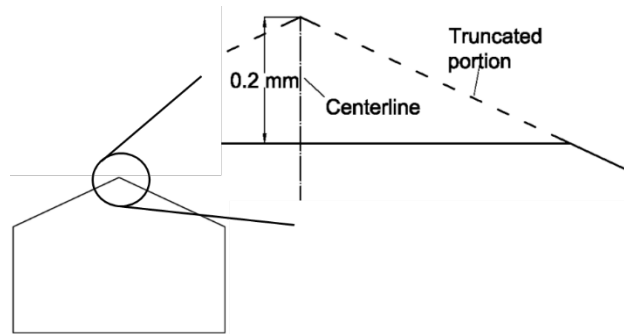
Figure 4-13. Section view (*x*-*y* plane) of truncated conical roof (Tank D).
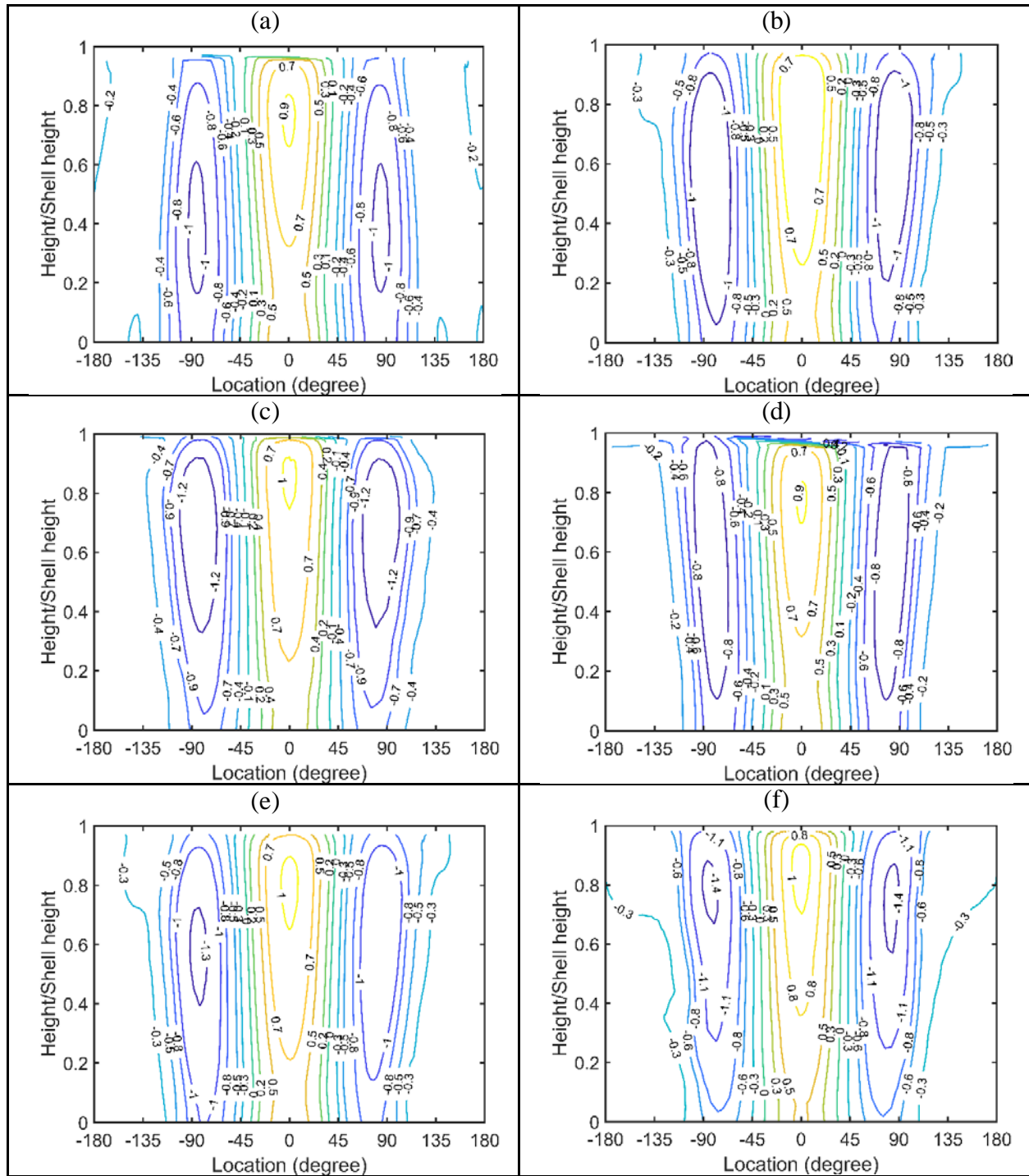
Figure 4-14. Pressure coefficient contours on the tank shells for (a) Tank A, (b) Tank B, (c) Tank C, (d) Tank D, (e) Tank E, and (f) Tank F. The vertical axis is the height at which the pressure coefficient is considered normalized with the shell height.
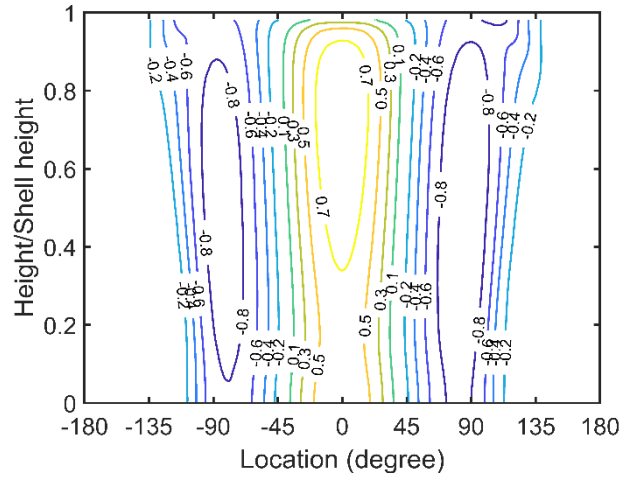
Figure 4-15. Pressure coefficient contours on the tank shells for Tank G. The vertical axis is the height at which the pressure coefficient is considered normalized with the shell height.
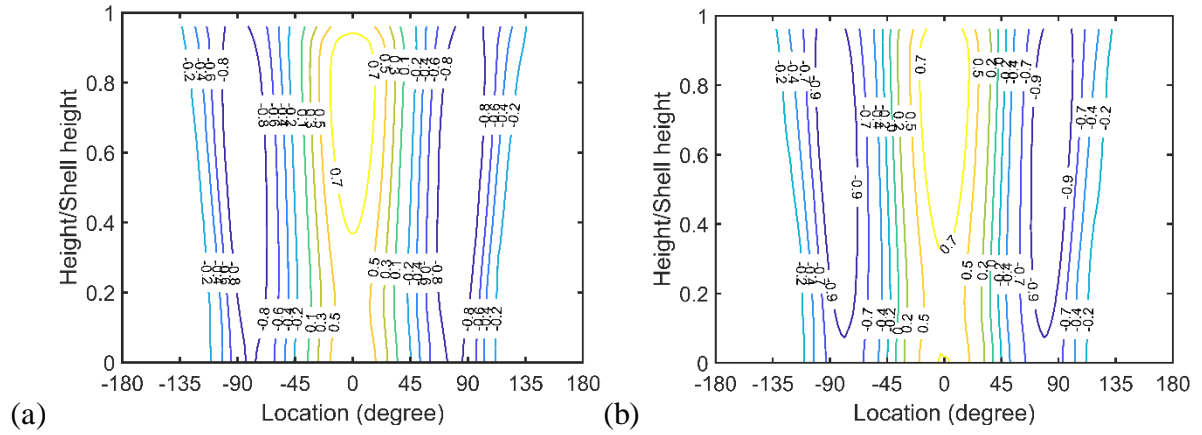
Figure 4-16. Pressure coefficient contours on the tank shells for (a) Tank H, and (b) Tank I. The vertical axis is the height at which the pressure coefficient is considered normalized with the shell height.
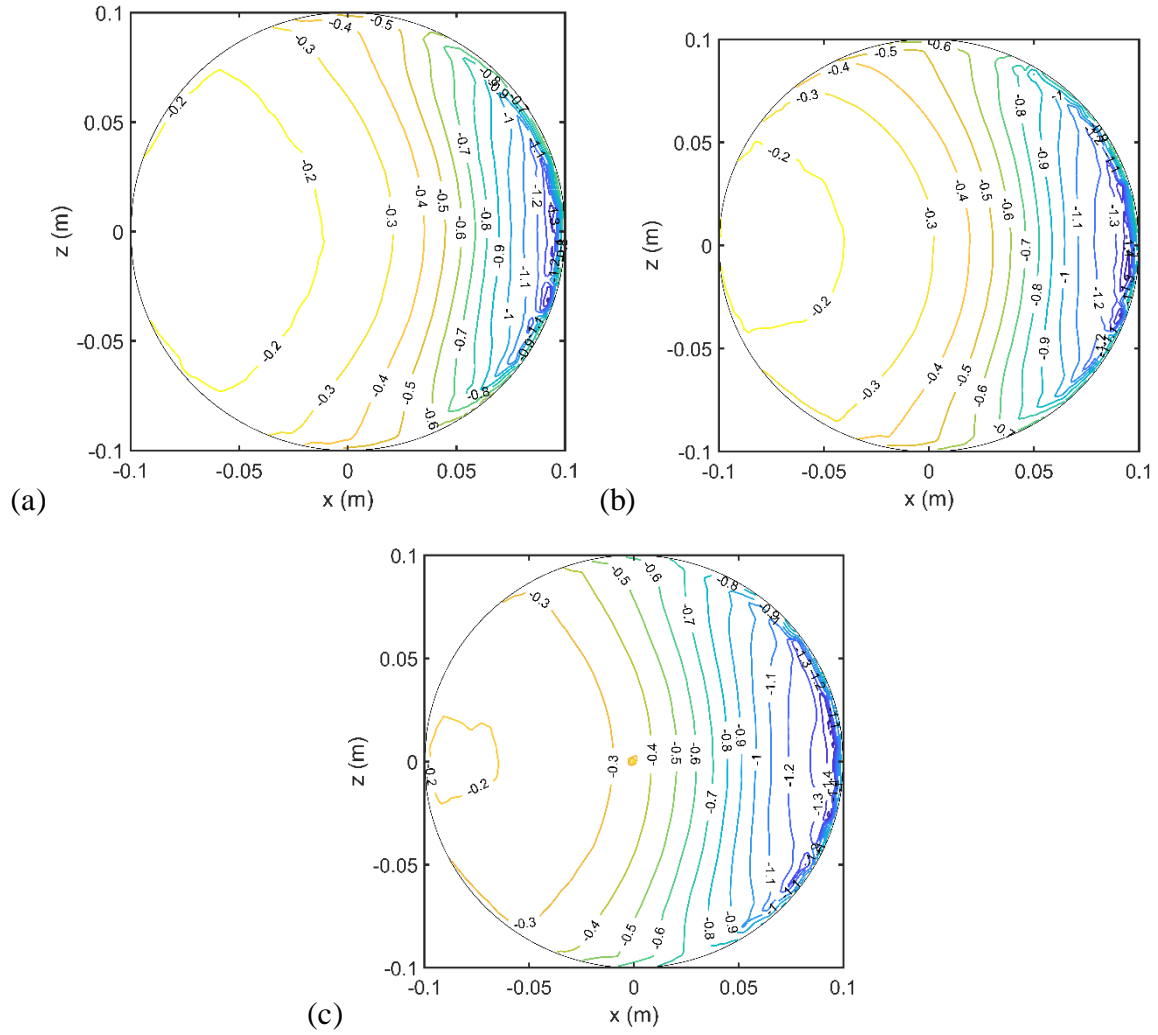
Figure 4-17. Pressure coefficient contours on the tank roof of (a) Tank A, (b) Tank B, and (c) Tank C.
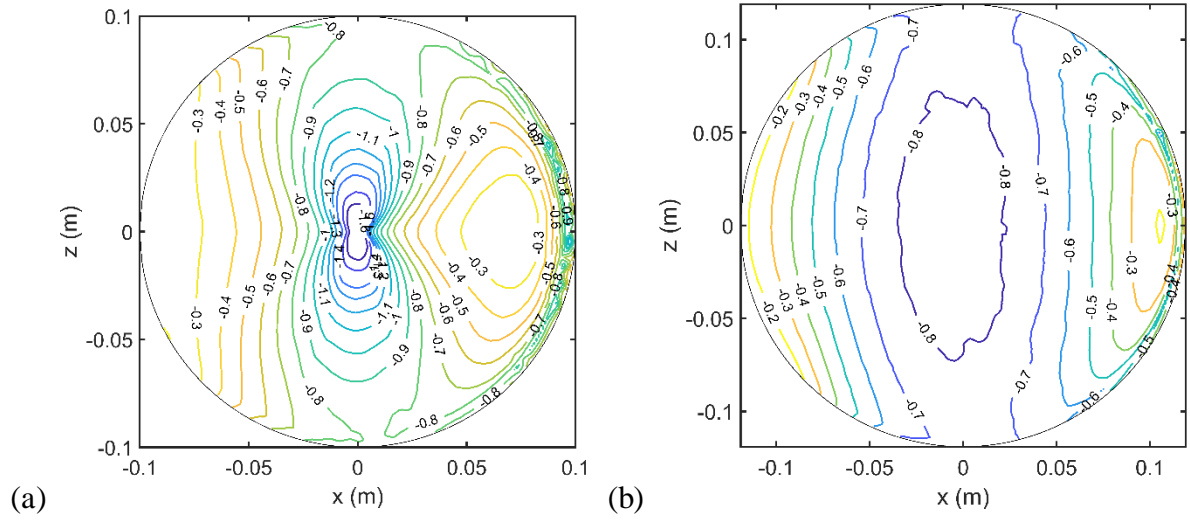
Figure 4-18. Pressure coefficient contours on the tank roof of (a) Tank E and (b) Tank H.

4.8   References

[1]   API, *Welded Tanks for Oil Storage*. Washington, DC. API Standard No.650: American Petroleum Institue, 2013.

[2]   E. Azzuni and S. Guzey, "Comparison of the shell design methods for cylindrical liquid storage tanks," *Engineering Structures,* vol. 101, pp. 621-630, 2015.

[3]   L. A. Godoy, "Buckling of vertical oil storage steel tanks: Review of static buckling studies," *Thin-Walled Structures,* vol. 103, Thin-Walled Structures, pp. 1-21, 2016.

[4]   A. Zingoni, "Liquid-containment shells of revolution: a review of recent studies on strength, stability and dynamics," *Thin-Walled Structures,* vol. 87, pp. 102-114, 2015.

[5]   L. Chen, J. M. Rotter, and C. Doerich-Stavridis, "Practical calculations for uniform external pressure buckling in cylindrical shells with stepped walls," *Thin-Walled Structrures,* vol. 61, pp. 162-168, 2012.

[6]   S. Aghajari, K. Abedi, and H. Showkati, "Buckling and post-buckling behavior of thin-walled cylindrical steel shells with varying thickness subjected to uniform external pressure," *Thin-Walled Structures,* vol. 44, no. 8, pp. 904-909, 2006.

[7]   A. R. Shokrzadeh and M. R. Sohrabi, "Buckling of ground based steel tanks subjected to wind and vacuum pressures considering uniform internal and external corrosion," *Thin-Walled Structures,* vol. 108, pp. 333-350, 2016.

[8]   A. R. Shokrzadeh and M. R. Sohrabi, "Strengthening effects of spiral stairway on the buckling behavior of metal tanks under wind and vacuum pressures," *Thin-Walled Structures,* vol. 106, pp. 437-447, 2016.

[9]   J. Spritzer and S. Guzey, "Nonlinear numerical evaluation of large open-top aboveground steel welded liquid storage tanks excited by seismic loads," *Thin-Walled Structures,* vol. 119, pp. 662-676, 2017.

[10]   M. Sobhan, F. Rofooei, and N. K. Attari, "Buckling behavior of the anchored steel tanks under horizontal and vertical ground motions using static pushover and incremental dynamic analyses," *Thin-Walled Structures,* vol. 112, pp. 173-183, 2017.

[11]   J.-G. Gong, Z.-Q. Zhou, and F.-Z. Xuan, "Buckling strength of cylindrical steel tanks under measured differential settlement: Harmonic components needed for consideration and its effect," *Thin-Walled Structures,* vol. 119, pp. 345-355, 2017.

[12]   Y. Zhao and Y. Lin, "Buckling of cylindrical open-topped steel tanks under wind load," *Thin-Walled Structures,* vol. 79, pp. 83-94, 2014.

[13]   E. Azzuni and S. Guzey, "Stability of open top cylindrical steel storage tanks: Design of top wind girder," *Journal of Pressure Vessel Technology,* vol. 139, no. 3, p. 031207, 2017.

[14]   T. Sun, E. Azzuni, and S. Guzey, "Stability of Open-Topped Storage Tanks With Top Stiffener and One Intermediate Stiffener Subject to Wind Loading," *Journal of Pressure Vessel Technology,* vol. 140, no. 1, p. 011204, 2018.

[15]   E. M. Sosa and L. A. Godoy, "Nonlinear dynamics of above-ground thin-walled tanks under fluctuating pressures," *Journal of sound and vibration,* vol. 283, no. 1-2, pp. 201-215, 2005.

[16]   F. Resinger and R. Greiner, "Buckling of wind loaded cylindrical shells—application to unstiffened and ring-stiffened tanks," in *Buckling of shells*. Berlin: Springer, 1982, pp. 305-331.

[17]   Y.-C. Chiang and S. Guzey, "Influence of Internal Inward Pressure on Stability of Open-Top Aboveground Steel Tanks Subjected to Wind Loading," *Journal of Pressure Vessel Technology,* vol. 141, no. 3, p. 031204, 2019.

[18]   I. Sabransky and W. Melbourne, "Design pressure distribution on circular silos with conical roofs," *Journal of Wind Engineering and Industrial Aerodynamics,* vol. 26, no. 1, pp. 65-84, 1987.

[19]   P. MacDonald, K. Kwok, and J. Holmes, "Wind loads on circular storage bins, silos and tanks: I. Point pressure measurements on isolated structures," *Journal of Wind Engineering and Industrial Aerodynamics,* vol. 31, no. 2-3, pp. 165-187, 1988.

[20]   X. Hua and C. Letchford, "A comparison of wind loads on circular bins, silos and tanks," in *Structures Congress 2014,* Boston, Massachusetts, 2014: ASCE, pp. 1616-1629.

[21]   Joint Standards Australia/Standard New Zealand Standard, *AS/NZS 1170.2: 2011 Structural design actions-Part 2: Wind actions*. Sydney, NSW, Australia, 2011.

[22]   American Society of Civil Engineers, *ASCE-7-16: Minimum Design Loads for Building and other Structures*. Reston, VA.: ASCE-7-16, 2016.

[23]   N. Cook and D. Redfearn, "Full-scale wind pressure measurements on cylindrical silos: a preliminary report," *Building Research Establishment, Note N 103/80,* 1980.

[24]   Y. Uematsu and C. Koo, "Wind-tunnel study of wind loads on circular cylindrical structures," *Journal of Wind Engineering,* pp. 17-25, 2008.

[25]   C. A. Burgos, R. C. Jaca, J. L. Lassig, and L. A. Godoy, "Wind buckling of tanks with conical roof considering shielding by another tank," *Thin-Walled Structures,* vol. 84, pp. 226-240, 2014.

[26]   Y. Zhao, Y. Lin, and Y.-b. Shen, "Wind loads on large cylindrical open-topped tanks in group," *Thin-Walled Structures,* vol. 78, pp. 108-120, 2014.

[27]   T. Matsui, Y. Uematsu, K. Kondo, T. Wakasa, and T. Nagaya, "Wind Effects on Dynamic Response of a Floating Roof in a Cylindrical Liquid Storage Tank," *Journal of Pressure Vessel Technology,* vol. 131, no. 3, p. 031307, 2009.

[28]   G. Portela and L. A. Godoy, "Wind pressures and buckling of cylindrical steel tanks with a conical roof," *Journal of Constructional Steel Research,* vol. 61, no. 6, pp. 786-807, 2005.

[29]   G. Portela and L. A. Godoy, "Wind pressures and buckling of cylindrical steel tanks with a dome roof," *Journal of Constructional Steel Research,* vol. 61, no. 6, pp. 808-824, 2005.

[30]   C. Iamandi, A. Georgescu, and C. Erbasu, "Experimental modelling of four steel tanks battery," in *Eleventh International Conference on Wind Engineering,* Lubbock, TX, 2003: Wind Science and Engineering Research Center at Texas Tech University, pp. pp. 1243-1250.

[31]   B. Blocken *et al.*, "Aerodynamic drag in cycling pelotons: new insights by CFD simulation and wind tunnel testing," *Journal of Wind Engineering and Industrial Aerodynamics,* vol. 179, pp. 319-337, 2018.

[32]   R.-w. Kim, I.-b. Lee, and K.-s. Kwon, "Evaluation of wind pressure acting on multi-span greenhouses using CFD technique, Part 1: Development of the CFD model," *Biosystems Engineering,* vol. 164, pp. 235-256, 2017.

[33]   A. Mochida, Y. Tominaga, S. Murakami, R. Yoshie, T. Ishihara, and R. Ooka, "Comparison of various k-ε models and DSM applied to flow around a high-rise building - report on AIJ cooperative project for CFD prediction of wind environment -," *Wind and Structures,* vol. 5, no. 2~4, pp. pp227-244, 2002.

[34] M. C. Montoya, F. Nieto, S. Hernández, I. Kusano, A. Álvarez, and J. Jurado, "CFD-based aeroelastic characterization of streamlined bridge deck cross-sections subject to shape modifications using surrogate models," *Journal of Wind Engineering and Industrial Aerodynamics,* vol. 177, pp. 405-428, 2018.

[35] J. Cheng, D. Qi, A. Katal, L. L. Wang, and T. Stathopoulos, "Evaluating wind-driven natural ventilation potential for early building design," *Journal of Wind Engineering and Industrial Aerodynamics,* vol. 182, pp. 160-169, 2018.

[36] J. Franke *et al.*, "Recommendations on the use of CFD in wind engineering," in *Proceedings of the International Conference on Urban Wind Engineering and Building Aerodynamics, COST Action C14, Impact of Wind and Storm on City Life and Built Environment,* Sint-Genesius-Rode, Belgium, 2004: von Karman Institute,.

[37] Y. Tominaga *et al.*, "AIJ guidelines for practical applications of CFD to pedestrian wind environment around buildings," *Journal of wind engineering and industrial aerodynamics,* vol. 96, no. 10-11, pp. 1749-1761, 2008.

[38] D. Hargreaves and N. G. Wright, "On the use of the k–ε model in commercial CFD software to model the neutral atmospheric boundary layer," *Journal of Wind Engineering and Industrial Aerodynamics,* vol. 95, no. 5, pp. 355-369, 2007.

[39] P. Richards and R. Hoxey, "Appropriate boundary conditions for computational wind engineering models using the k-ε turbulence model," *Journal of wind engineering and industrial aerodynamics,* vol. 46, pp. 145-153, 1993.

[40] M. Cindori, F. Juretić, H. Kozmar, and I. Džijan, "Steady RANS model of the homogeneous atmospheric boundary layer," *Journal of Wind Engineering and Industrial Aerodynamics,* vol. 173, pp. 289-301, 2018.

[41] M. S. Thordal, J. C. Bennetsen, and H. H. H. Koss, "Review for practical application of CFD for the determination of wind load on high-rise buildings," *Journal of Wind Engineering and Industrial Aerodynamics,* vol. 186, pp. 155-168, 2019.

[42] M. Shirzadi, P. A. Mirzaei, and M. Naghashzadegan, "Improvement of k-epsilon turbulence model for CFD simulation of atmospheric boundary layer around a high-rise building using stochastic optimization and Monte Carlo Sampling technique," *Journal of Wind Engineering and Industrial Aerodynamics,* vol. 171, pp. 366-379, 2017.

[43] FLUENT ANSYS, *19.0 User's Guide*. Canonsburg, PA: Ansys Inc., 2019.

[44]   D. C. Wilcox, *Turbulence modeling for CFD*. DCW industries La Canada, CA, 1998.

[45]   FLUENT ANSYS, *19.0 Theory Guide*. Canonsburg, PA: Ansys Inc. , 2019.

[46]   N. J. Mulvany, L. Chen, J. Y. Tu, and B. Anderson, "Steady State Evaluation of Two Equation RANS Turbulence Models for High Reynolds Number Hydrodynamic Flow Simulations," *Final Report, Defence Science and Technology Organisation, Departement of Defence, Australian Goverment,* 2004.

[47]   P. Irwin, R. Denoon, and D. Scott, *Wind Tunnel Testing of High-Rise Buildings: An Output of the CTBUH Wind Engineering Working Group*. Chicago, IL: Council on Tall Buildings and Urban Habitat (CTBUH), 2013.

[48]   S. Murakami, "Overview of turbulence models applied in CWE–1997," *Journal of Wind Engineering and Industrial Aerodynamics,* vol. 74, pp. 1-24, 1998.

[49]   European Committee for Standardization, *Eurocode 3: Design of Steel Structures, Part 4.1: Silos*. Brussels, Belgium.: Standard No. EN 1993-4-1, 2007.

5. CONCLUSION

Three independent studies were conducted to evaluate the current design guidelines presented in API 650 and ASCE-7. The design wind load for an open-top tank has no major change in the past few decades. The API 650/ASCE-7 wind distribution profile dictates that the wind pressure is applied on to the projected area of a tank, while this distribution is actually far from the results obtained through wind tunnel tests. Especially, the internal pressure on an open-top tank specified in ASCE-7 and API 650 is significantly smaller than what is observed in BLWT. Additionally, the design guideline in API 650 bases on static analyses, though wind loading should be considered to be a dynamic loading. Therefore, in order to evaluate the dynamic effect on buckling capacity of open-top tanks, explicit dynamic analyses and natural vibration frequency analysis were conducted and were complied in Chapter 2. To compare the design wind load in different design documents and asses the adequacy of ASCE-7 and API 650, different wind distribution profiles specified in various design documents were adopted for conducting static analyses in Chapter 3. To study how wind pressure distributes on tank under a gust of wind, computational fluid dynamics analyses were conducted in Chapter 4.

In Chapter 2, it was concluded that the examined open-top tanks does not experience a resonance in the selected setups. A frequency analysis was first conducted to identify the mode with the most effective mass for each individual tanks. Analysis parameters including mesh size and time step size were discussed to ensure the accuracy of the performed analyses. Wind loading with a wide range of fluctuation period was considered to represent fluctuation of wind gusts. It turns out that the dynamic buckling capacities of boarder tanks ($H/D < 1.0$), no matter the load fluctuation period, were similar to the buckling capacities obtained through a static analysis. For taller tanks ($H/D > 1.0$), the static buckling capacity was perceptibly larger than the dynamic buckling capacity, but it was still concluded that resonance was not observed throughout the study.

Chapter 3 delivered a comparison of the behavior of six tanks subjected to static wind loading specified in different design documents. The effect of imperfection geometry, the effect of aspect ratio, and the effect of material plasticity were discussed as well. A study on how the input parameters in a Riks analysis affects the accuracy of the analysis was also conducted. The results

show that among four selected distribution profiles, the ASCE-7/API 650 profile yields a largest buckling capacity for all examined tanks. This indicates that compare to other wind profiles, the ASCE-7/API 650 profile is the least conservative profile. Since wind profile specified in other design documents are more close to results obtained through BLWT, wind profile in API 650 and ASCE-7 may need a revision.

Chapter 4 studied the wind pressure distribution on nine close-top tanks with a wide spectrum of aspect ratios and roof configurations by conducting computational fluid dynamics (CFD) analyses. Tanks with aspect ratios ranging from 0.4 to 2 were studied, and roof configurations including flat, conical, and dome roofs were considered. To properly carry out the CFD analysis, a through parametric study on the input parameter based on published guidelines was conducted using a tank with an aspect ratio of 0.5 and a flat roof. Criteria as to determine the input parameters were proposed. With the established criteria, wind pressure distribution on the rest of eight tanks were reported and compared to published BLWT results. It was concluded that with the established criteria, the pressure distribution obtained is fairly close to the BLWT results.

These three studies intend to point out the improvement that could be made on the current design documents. It can be concluded that a static analysis shall be enough for a practical design purpose. The wind profile used by ASCE 7 and API 650 has not be substantially changed for several decades, and it may need a revision to ensure the stability tanks under wind loading.

APPENDIX A. COMPLETE POSTBUCKLING ANALYSIS RESULTS FOR CHAPTER 3

In this appendix, the complete postbuckling analysis results are presented for the completeness of the study. See Tables A-1 to A-6 for the complete results.
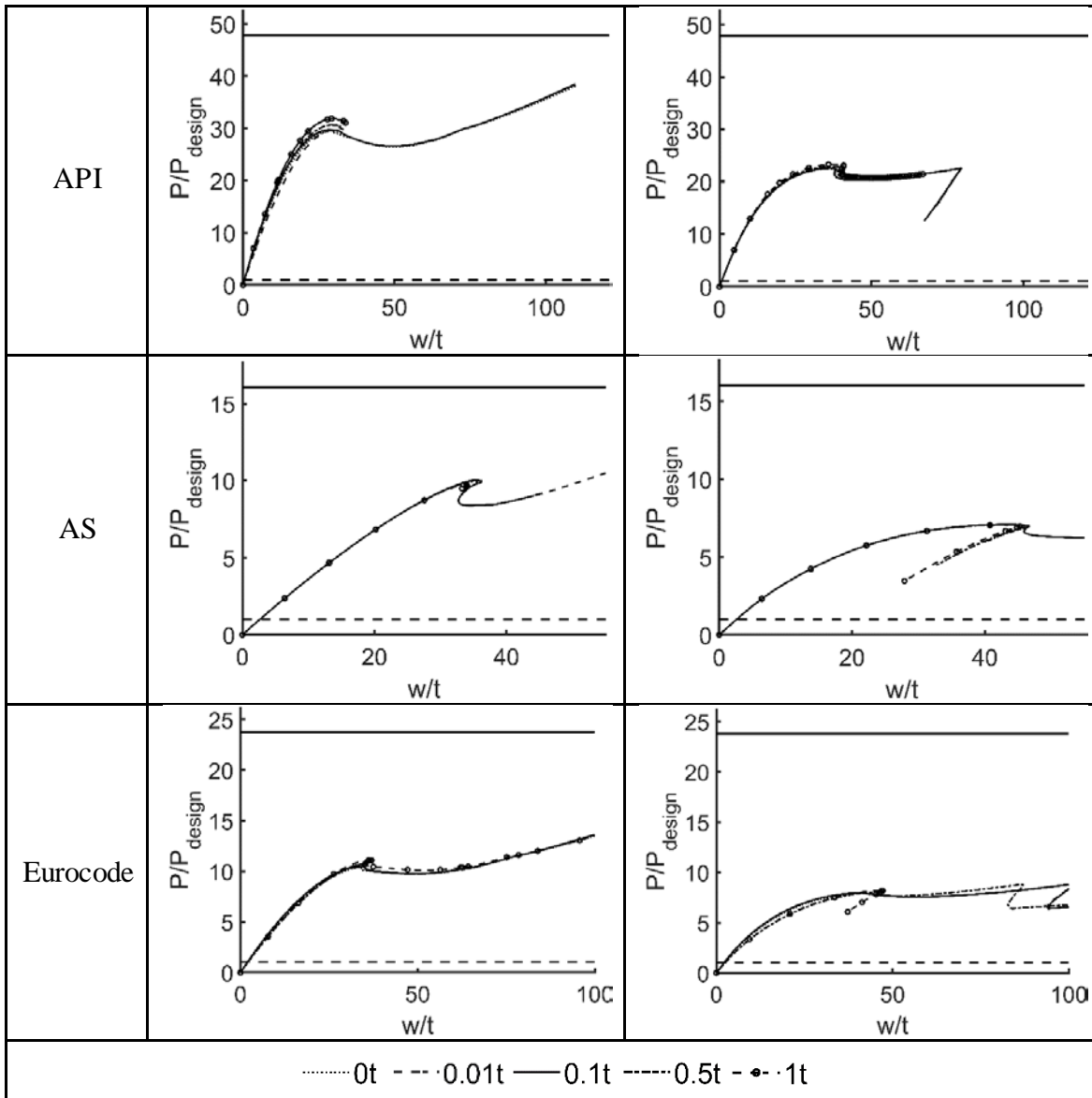
Figure A-1. The postbuckling analysis with and without material plasticity (left and right column, respectively) for Tank A subjected to the wind loading produced by the selected wind profiles with different imperfection amplitudes. A horizontal solid line represents the LBA buckling capacity, and a horizontal dotted line represents the design wind pressure.
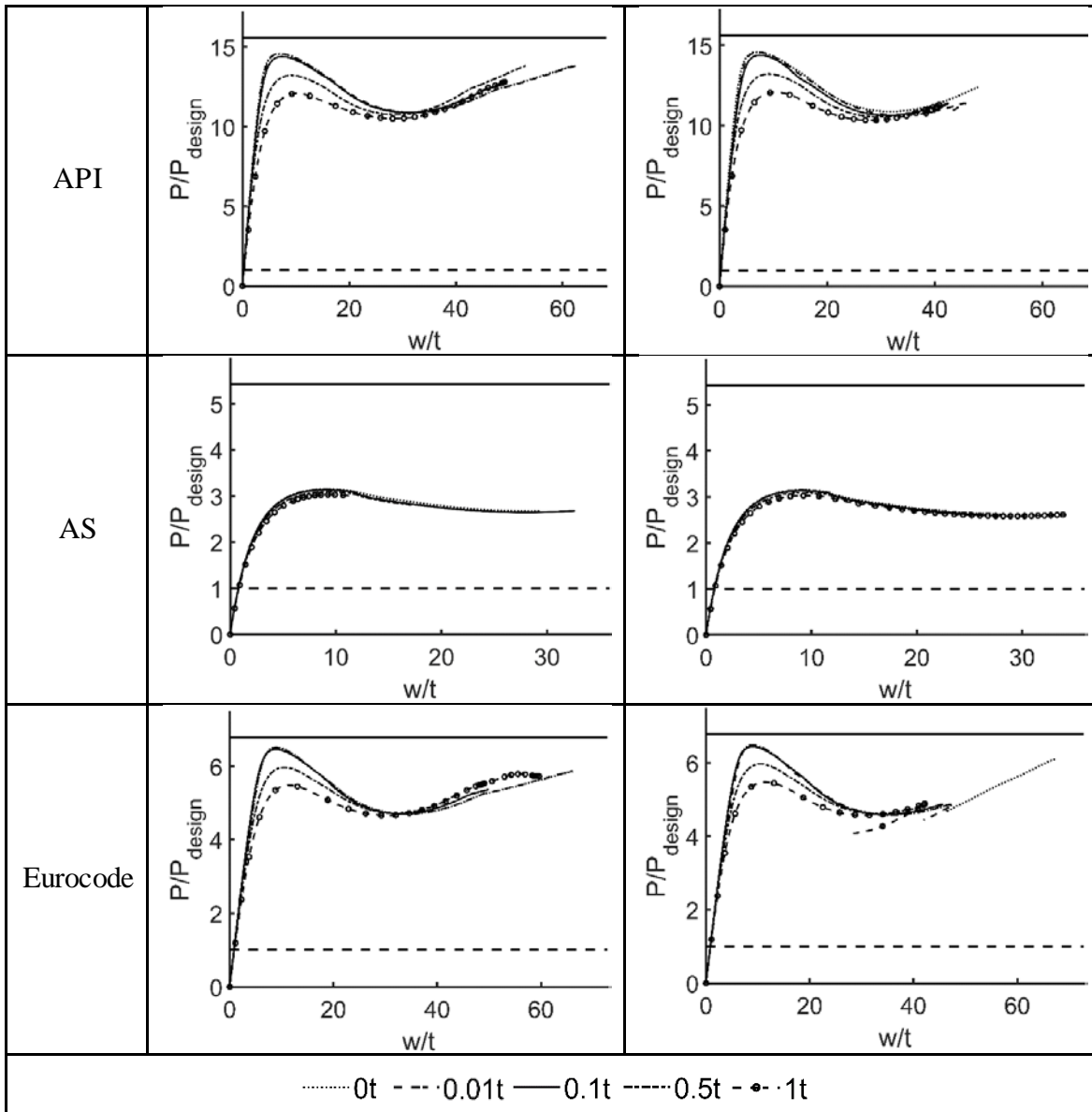
Figure A-2. The postbuckling analysis with and without material plasticity (left and right column, respectively) for Tank B subjected to the wind loading produced by the selected wind profiles with different imperfection amplitudes. A horizontal solid line represents the LBA buckling capacity, and a horizontal dotted line represents the design wind pressure.
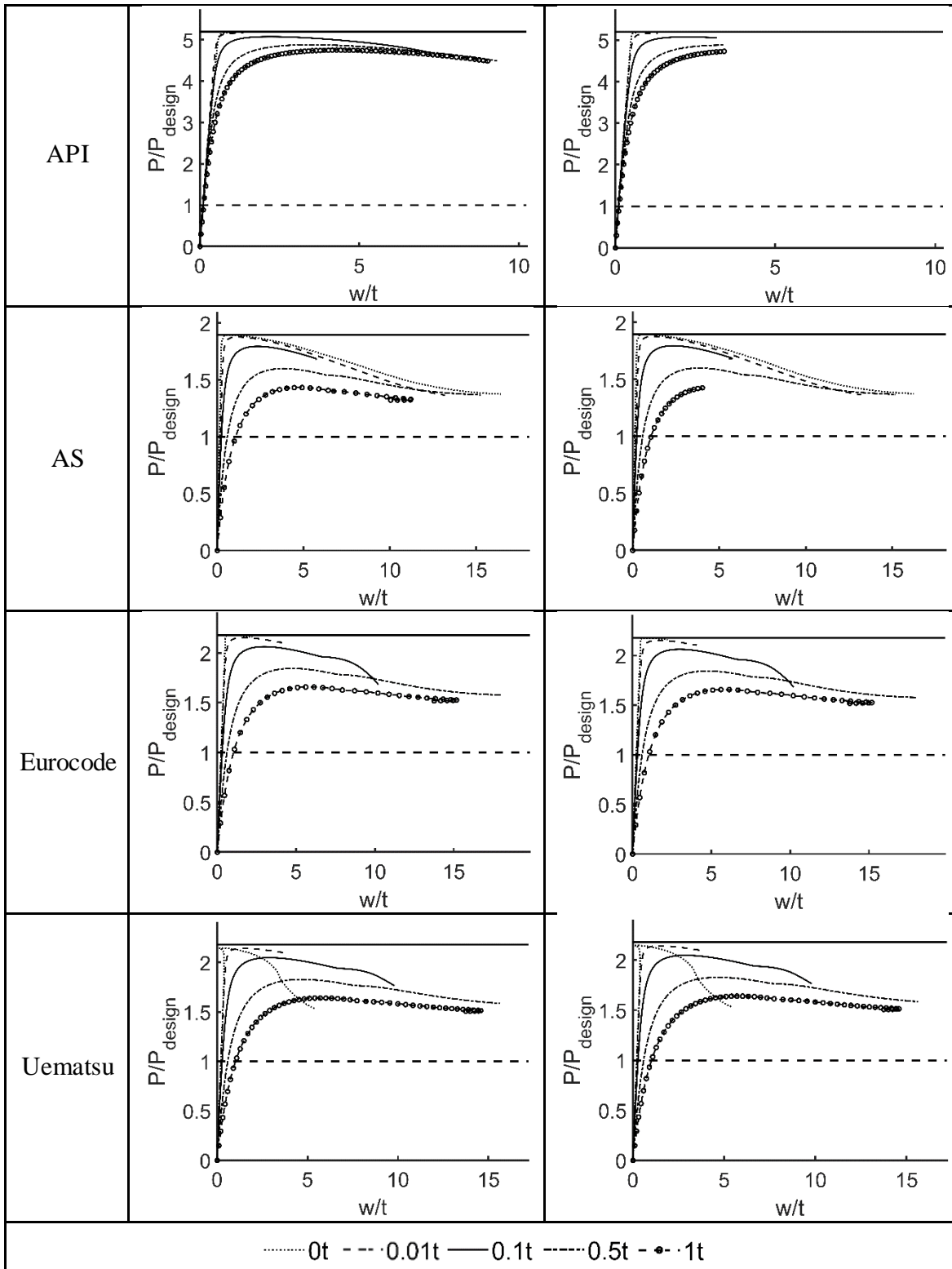
Figure A-3. The postbuckling analysis with and without material plasticity (left and right column, respectively) for Tank C subjected to the wind loading produced by the selected wind profiles with different imperfection amplitudes. A horizontal solid line represents the LBA buckling capacity, and a horizontal dotted line represents the design wind pressure.
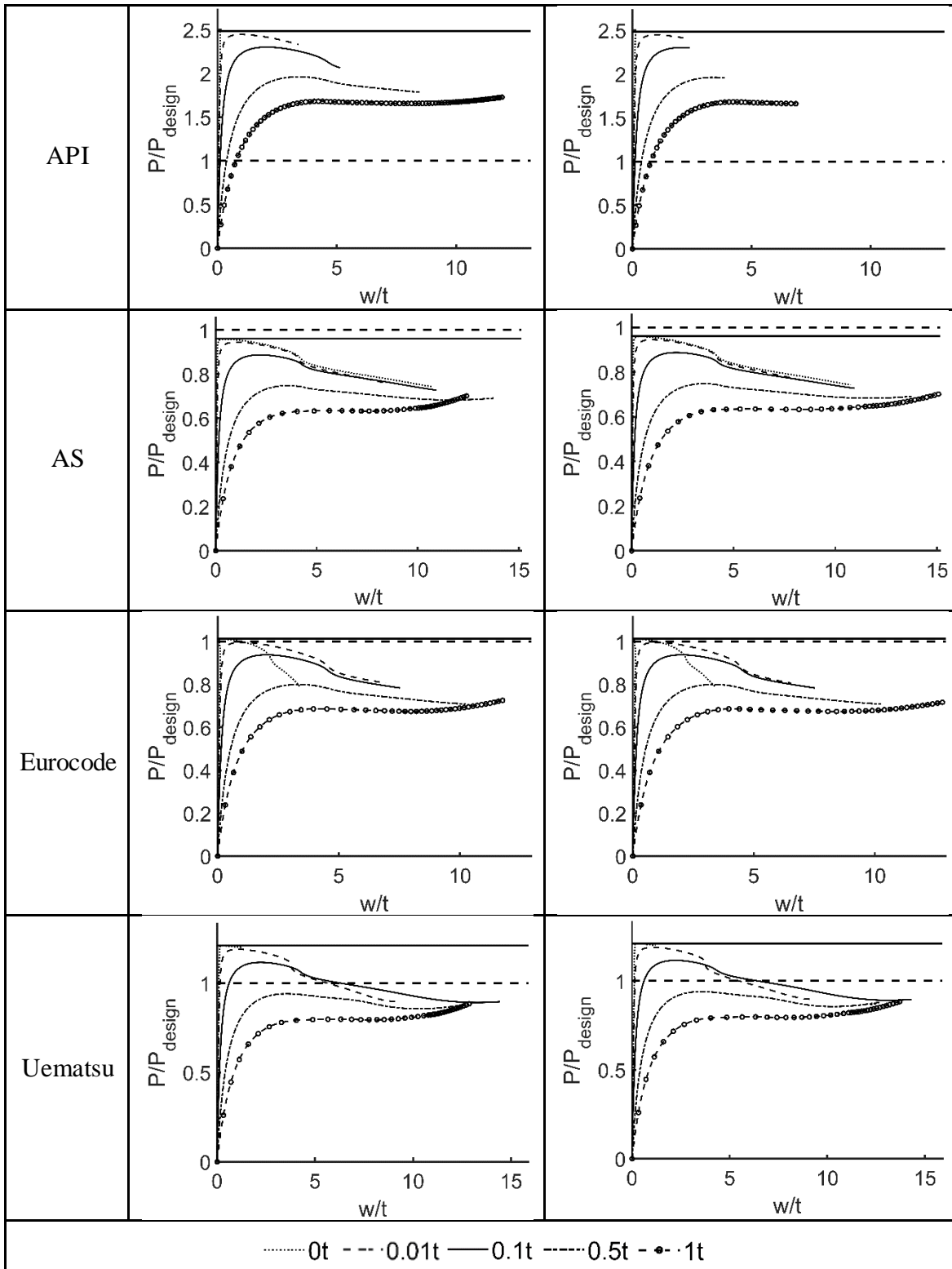
Figure A-4. The postbuckling analysis with and without material plasticity (left and right column, respectively) for Tank D subjected to the wind loading produced by the selected wind profiles with different imperfection amplitudes. A horizontal solid line represents the LBA buckling capacity, and a horizontal dotted line represents the design wind pressure.
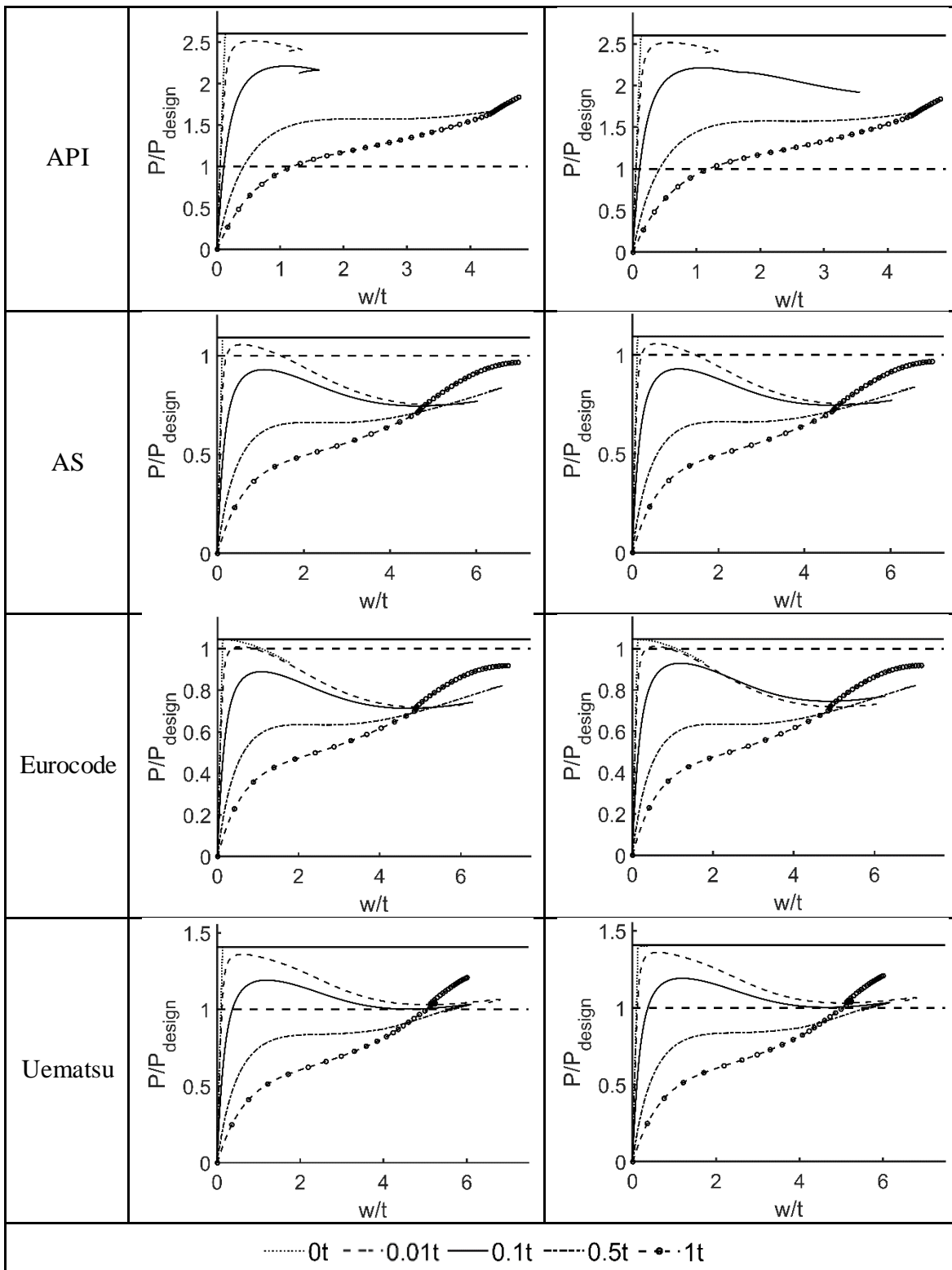
Figure A-5. The postbuckling analysis with and without material plasticity (left and right column, respectively) for Tank E subjected to the wind loading produced by the selected wind profiles with different imperfection amplitudes. A horizontal solid line represents the LBA buckling capacity, and a horizontal dotted line represents the design wind pressure.
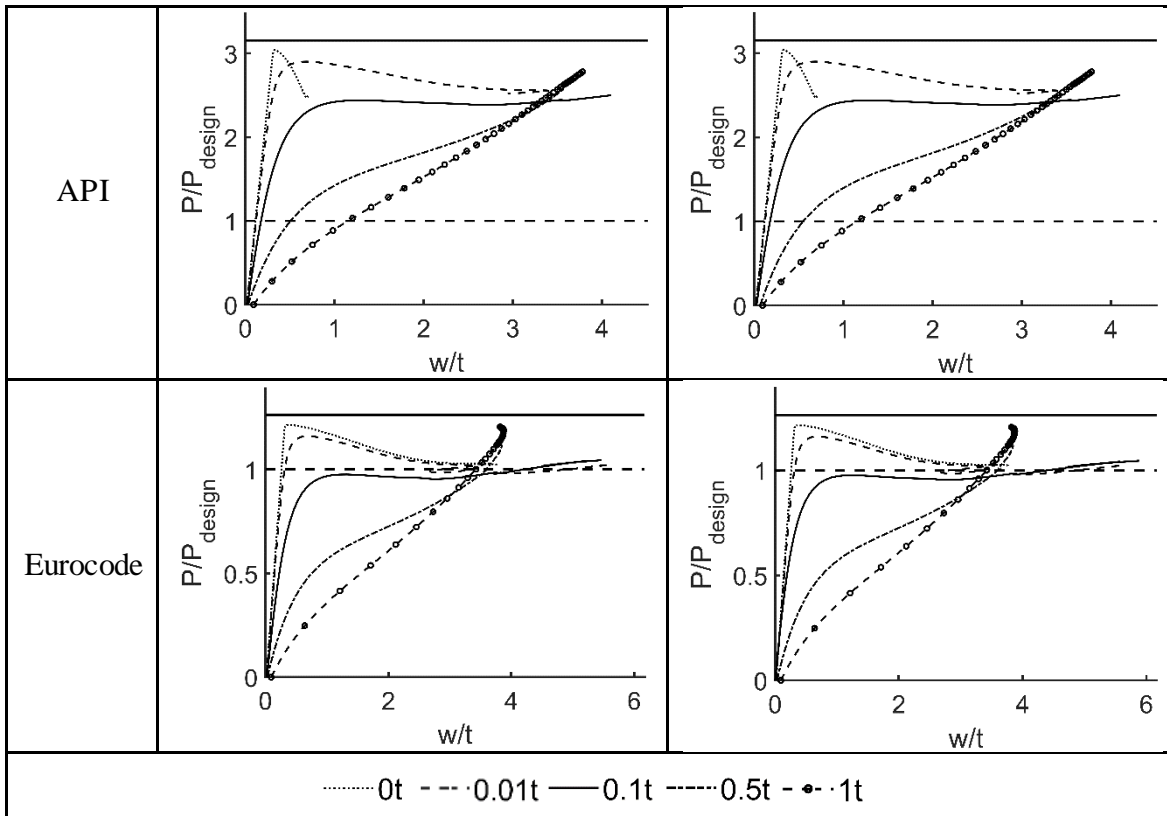
Figure A-6. The postbuckling analysis with and without material plasticity (left and right column, respectively) for Tank F subjected to the wind loading produced by the selected wind profiles with different imperfection amplitudes. A horizontal solid line represents the LBA buckling capacity, and a horizontal dotted line represents the design wind pressure.